Chem Soc Rev

REVIEW ARTICLE

View Article Online
View Journal | View Issue

Cite this: *Chem. Soc. Rev.*, 2015, **44**, 3143

Energetics of atomic scale structure changes in graphene

Stephen T. Skowron,[a] Irina V. Lebedeva,[b] Andrey M. Popov[c] and Elena Bichoutskaia*[a]

Received 18th December 2014

DOI: 10.1039/c4cs00499j

www.rsc.org/csr

The presence of defects in graphene has an essential influence on its physical and chemical properties. The formation, behaviour and healing of defects are determined by energetic characteristics of atomic scale structure changes. In this article, we review recent studies devoted to atomic scale reactions during thermally activated and irradiation-induced processes in graphene. The formation energies of vacancies, adatoms and topological defects are discussed. Defect formation, healing and migration are quantified in terms of activation energies (barriers) for thermally activated processes and by threshold energies for processes occurring under electron irradiation. The energetics of defects in the graphene interior and at the edge is analysed. The effects of applied strain and a close proximity of the edge on the energetics of atomic scale reactions are overviewed. Particular attention is given to problems where further studies are required.

1. Introduction

Since the discovery of one- and two-dimensional carbon nanostructures, nanotubes[1] and graphene[2] respectively, a variety of interesting fundamental properties and applications of these nanostructures have been found. Contrary to bulk matter, one- and two-dimensional nanostructures do not correspond to the ground state of an infinite 3D system. Thus, studies of the kinetics of atomic scale processes are especially important for understanding atomistic formation mechanisms of these nanostructures. Such kinetics are determined by the energetics of bond realignment, emission and insertion of carbon atoms.

Transformation of carbon nanostructures under heating[3–6] or electron irradiation[3,4,7–14] leads to a production of entirely new species (see also ref. 15 for a recent review on modelling

[a] *School of Chemistry, University of Nottingham, University Park, Nottingham NG7 2RD, UK. E-mail: elena.bichoutskaia@notiingham.ac.uk*
[b] *Nano-Bio Spectroscopy Group and ETSF Scientific Development Centre, Departamento de Fisica de Materiales, Universidad del Pais Vasco UPV/EHU, San Sebastian E-20018, Spain*
[c] *Institute for Spectroscopy of Russian Academy of Sciences, Troitsk, Moscow 142190, Russia*

Stephen T. Skowron

Steve Skowron was awarded his MSci degree in Chemistry from the University of Nottingham in 2012. During his masters project he worked with Dr Nick Besley in developing inexpensive methods for computing NEXAFS spectra using time-dependent DFT. Remaining at Nottingham, he started his PhD in the computational nanoscience group in the same year, under the supervision of Dr Elena Bichoutskaia. His current research focuses on the effects of electron irradiation in TEM, using accurate ab initio calculations coupled with experimental images to investigate structure transformations of graphene and nanotube-encapsulated molecules.

Irina V. Lebedeva

Irina Lebedeva is a Marie Curie postdoctoral fellow at Nano-Bio Spectroscopy Group of the University of the Basque Country, Spain. She received her Bachelor (2006) and Master (2008) degrees from Moscow Institute of Physics and Technology and PhD degree (2011) in Chemical Physics from National Research Centre "Kurchatov Institute", Russia. Irina is an author of more than 35 publications on atomistic and multi-scale modeling of growth and transformation of carbon nanostructures, their mechanical, tribological and transport properties and application in nano-electromechanical systems.

transformation processes under electron irradiation). Among the most striking examples of such processes are the formation of graphene nanoribbons from different organic molecules inside carbon nanotubes under heating[3,4] and electron irradiation,[3,4] the formation of flat nanotubes from bilayer graphene nanoribbons,[7] fullerenes from initially flat graphene flakes[8] and carbon chains from graphene[13,14] under electron irradiation. Others include the transformation of polyhedral graphitic nanoparticles into quasi-spherical onions under heating[5] and electron irradiation,[9,10] the formation of double-walled nanotubes from single-walled nanotubes filled with fullerenes under heating[6] and electron irradiation,[11] and the formation of a trilobate structure from three La@C_{82} endofullerenes inside a carbon nanotube under electron irradiation.[12] Mesoscopic processes such as the shrinking of nanotube diameter under electron irradiation,[16] migration and merging of large holes in the outer wall of nanotubes at high temperature,[17] superelongation of carbon nanotubes at high temperature,[18,19] and the migration and annihilation of graphene grain boundaries under electron irradiation[20] have also been observed. These large transformations in nanostructures take place *via* bond realignments complemented by atom emission, and are determined by energetic characteristics of the corresponding atomic scale reactions.

The presence of defects in graphene structure[21–61] leads to new electronic,[33–44] magnetic,[21,24,35,45–55] thermal[56–61] and mechanical[22–32] properties. In addition to defect formation, self-healing of defects has been observed in carbon nanostructures, including vacancies and holes in nanotubes[62,63] and graphene[64–66] structure. The processes of defect formation, healing and changes of defect type due to bond realignment and atom emission reactions are determined by the activation energies (barriers) of thermally activated processes and the threshold energies of irradiation-induced processes.

The energetics of all atomic-scale reactions change upon approaching graphene edges,[52,56,67–71] and this is especially important for graphene nanoribbons. Edge reconstructions with the formation of topological defects are frequently observed under electron irradiation[13,72–75,270] and significantly deteriorate elastic[76] and fracture[77] properties of graphene nanoribbons. Creation of defects at the edges of graphene nanoribbons can also be used to tune electron[78–85] and thermal[86] transport. Atoms are less stable and much more reactive at the edge compared to the graphene interior, and so reactions at edges play a crucial role in transformations of carbon nanostructures. Notable examples include the transformation of a graphene flake to a fullerene,[8,70,71,87] the formation of nanotube caps,[88] sewing up graphene layers into a nanotube,[89,90] reconstruction of holes in graphene[91] and carbon nanotubes,[92–94] and graphene growth[95] and evaporation[96] at high temperatures.

There are currently several reviews devoted to the properties of carbon nanostructures with irradiation defects[97,98] and properties of graphene with defects.[99,100] A very recent review[101] covers the general study of graphene with TEM, while the various structures of interest in graphene under TEM are detailed in ref. 72. However, the energetics of rate determining bond reorganisations in graphene has not yet gained considerable attention within a single review. In the present review we provide an overview of the energetic characteristics of various thermally activated and irradiation-induced reactions in the graphene interior and at graphene edges. In addition to static characteristics, such as formation energies of defects relative to perfect structures, we consider activation energies and threshold energies under irradiation for various bond reorganisations and atom emission reactions. The relationship between atomic scale energetic characteristics and experimentally observable macroscopic processes is discussed.

As most energetic characteristics related to atomic scale structure changes in graphene cannot be determined from experiment, the majority of the data presented in the review is obtained by chemical calculations. However, the activation energies for thermally activated processes and the threshold energies for processes occurring under electron irradiation are

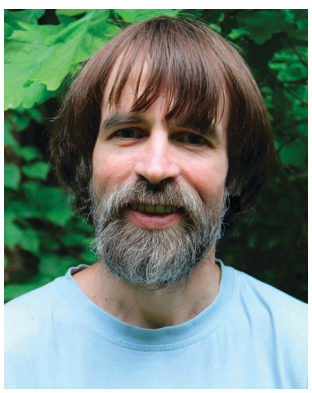

Andrey M. Popov

Andrey Popov is a senior scientific researcher at the Institute of Spectroscopy of Russian Academy of Science, Moscow. He received his MSci degree (1989) from the Moscow Institute of Physics and Technology, and his PhD in Physics (2007) from the Institute of Spectroscopy of Russian Academy of Science. Andrey is an author of 80 refereed publications including 4 reviews concerned with the energetics, structure, formation, transformation, thermodynamic and tribological properties of nanostructures and related nanotechnology problems, particularly applications of carbon nanotubes and graphene in nanoelectromechanical systems.

Elena Bichoutskaia

Elena Bichoutskaia is an Associate Professor in Theoretical and Computational Chemistry at the University of Nottingham, UK. Her research interests include the development of theoretical and computational approaches to prediction of materials properties; computational modelling of the behaviour, properties and manipulation of carbon nanomaterials; electrostatic interactions at the nanoscale; gas storage and interactions in porous solids. Elena is a recipient of EPSRC Career Acceleration Fellowship (2008–2014), New Directions for EPSRC Research Leaders Award (2012–2014), and ERC Consolidator Grant (2013–2017).

rather sensitive to the level of theory used in calculations. Section 2 details some common computational approaches to calculating the key parameters of thermally- and irradiation-induced structure transformations. Section 3 presents the structure of defects in graphene as well as their formation energies and barriers for atomic scale reactions in thermally activated processes. The threshold energies for reactions under irradiation are described in Section 4. Conclusions based on published results are discussed in Section 5, together with some problems which remain unsolved.

2. Computational approaches

2.1 Methods for calculating interatomic interactions in carbon nanostructures

Depending on the complexity of the problem under consideration, different methods should be chosen for the description of atomic interactions in carbon nanostructures. The most accurate results are obtained by quantum chemical methods that do not require *a priori* knowledge of any specific characteristics of the considered system. The optimal balance between accuracy and efficiency is achieved by density functional theory (DFT),[102,103] in which the total energy of the system is considered as a functional of the electron density and the description of the system is reduced to a set of self-consistent one-particle Schrödinger equations. In the simplest local density approximation (LDA),[104] the exchange–correlation energy depends only on the local electron density, which is sufficient for a description of periodic solids but can lead to significant errors for molecular systems and surfaces. Introduction of the dependence on the gradient of electron density in the generalized gradient approximation (GGA) improves results considerably. Perdew–Wang[105,106] (PW91) and Perdew–Burke–Ernzerhof[107,108] (PBE) GGA functionals are successfully used for calculations of defects in carbon nanostructures. Admixing of a fraction of exact exchange in hybrid functionals (PBE0,[109] B3LYP[110,111]) or inclusion of higher derivatives of the electron density in metaGGA functionals (such as M06-L[112,113]) further improves DFT performance, while dispersion corrections (vdW-DF,[114] DFT-D[115,116]) are important for accurate assessments of geometrical and energetic characteristics of defects in few-layer carbon nanostructures. The account of spin is critical for the analysis of defects with unpaired electrons, such as monovacancies, or graphene edges.

Though DFT offers an efficient framework for full-scale quantum modelling, the size of the considered systems is still limited to hundreds of atoms. Tight-binding models[117–124] represent a cheap alternative to first-principles methods, where quantum effects are captured by a direct, albeit simplified, description of electronic structure. Tight-binding parameters determining single-electron energies and a classical repulsive potential energy term are fitted to reference datasets or results of first-principles calculations. Tight-binding models can therefore be considered as a bridge between classical methods and full modelling of the quantum nature of chemical bonding. The incorporation of self-consistent calculations of the charge distribution[117,118] further improves the accuracy of tight-binding methods.

Classical force fields enable simulations with increased computational efficiency and system size, using analytical potentials to describe the interactions between atoms. These potentials are constructed and fitted to describe the particular behaviour of atoms in the system, observed in experiment or in accurate quantum mechanical calculations. Alongside simple analytical forms of pair potentials, such as the Morse potential,[125] more complex reactive potentials have been developed, capable of describing covalently bonded crystal structures such as graphene. In traditional forms of potentials all bonds are defined explicitly, which makes them unable to model chemical reactions due to the requirement of breaking and forming bonds. Reactive forms of potentials, however, deliberately avoid using explicit bonds in favour of bond orders, thus allowing for continuous bond formation and breaking. The development of reactive potentials is based on the decomposition of chemical bonding into individual contributions (angular, stretching, dihedral terms *etc.*) to the binding energy, while introducing cross-terms as a penalty for over- and/or under-coordination. Thirty years ago, Abell introduced a general expression for the binding energy as a sum of nearest neighbour pair interactions moderated by the local atomic environment.[126] In the 1990s, Tersoff[127] and Brenner[128] successfully applied the Abell formalism to various solid-state carbon structures including hydrocarbons. Subsequently, Brenner and Stuart *et al.* extended the original Brenner empirical potential into a second-generation reactive empirical bond order (REBO) potential energy expression for hydrocarbons[129] and non-bonded and dihedral-angle interactions were included (AIREBO).[130] Extensions of these potentials to metals[87,131–133] make simulations of complex catalytically activated processes possible. Van Duin, Goddard and co-workers developed a new formulation of the reactive potential, ReaxFF, based on accurate benchmarking density functional theory studies and extended its use to various materials, including hydrocarbon reactions,[134] transition metals,[135] silicon[136] and other materials such as polymers and ceramics.

In spite of this significant progress in the development of reactive empirical potentials for carbon systems, they are still not sufficiently accurate for studies of some problems related to graphene energetics. As mentioned below, the reactive bond-order potentials (initially developed for hydrocarbons) fail to reproduce the adequate ground state for monovacancies in graphene. Further improvement of existing potentials for the description of specific problems is possible, by fitting their parameters to certain properties that are important for the phenomena under consideration. For example, the parameters of the Brenner potential have recently been fitted to energies of zigzag and armchair graphene edges and elastic energies of the C_{60} and C_{70} fullerenes.[133] This modification of the potential improved the description of the balance between the fullerene elastic energy and graphene edge energies, which is important for the energetics of graphene formation or its transformation to other carbon nanostructures.

2.2 Analysis of thermally activated reactions of defects

A significant contribution to the understanding of the formation and transformation of defects in carbon nanostructures is provided by the analysis of their free energy surface. To reduce computational cost, these reactions are considered in simulation cells with periodic boundary conditions (PBC) or for finite-size flake models. The reliability of such calculations is determined not only by the accuracy of the description of the interatomic interactions, but also by the convergence of the results with respect to the size of the simulation cell (so that periodic images of the defects do not interact) or size of the finite model (to eliminate edge effects) and other simulation parameters. The saddle point in reactions of defects can be sought by restricting some degrees of freedom of the system or by modified geometry optimisation methods.[137,138] A more efficient nudged elastic band method,[139,140] which has been widely used in recent years, is based on the optimisation of the total energy of a string of system images connecting known initial and final states. Another useful method for searching for saddle points is action-derived molecular dynamics, which generates dynamical trajectories with fixed pre-assigned initial and final boundary conditions.[141] Such a method was used, for instance, to find a path with a set of saddle points for vacancies approaching and coalescing in graphene.[142] Using a simple Arrhenius formula, the reaction barriers obtained by these methods can be used to estimate the reaction rates at experimental conditions. The lifetime t_s of a state can be calculated in this way as

$$t_s = \nu^{-1} \exp(\Delta E_t / kT) \quad (1)$$

where ν is the characteristic frequency, ΔE_t is the barrier between states, k is the Boltzmann constant, and T is the temperature.

Molecular dynamics (MD)[143,144] and Monte Carlo[143,145] methods allow computational modelling of the evolution of carbon nanostructures with time. In Monte Carlo methods, one of the possible elementary processes at each simulation step is chosen on the basis of their probabilities, obtained according to their energetics. A list of possible elementary processes and their parameters can be known in advance or determined "on-the-fly" by probing the free energy surface. Molecular dynamics, in which trajectories of atoms are obtained by the numerical integration of Newton's equations of motion for nuclei, with the forces evaluated according to the classical force fields or *ab initio* methods, does not require any information on possible elementary processes or analysis of the free energy surface. However, even for classical systems, this method is typically limited by the time scales of microseconds. Limitations of *ab initio* molecular dynamics methods are much more severe and the corresponding numerical experiments are three orders of magnitude shorter in time. Practically all processes of formation and transformation of defects are activated and would not fit into this timeframe under experimental conditions (*e.g.*, at room temperature). A common approach to overcome this difficulty is to accelerate kinetics by increasing the simulation temperature. In this way, one can access valuable information on the process mechanism and gain insight into the kinetics of the process. However, extraction of kinetic parameters requires extensive statistics. Furthermore, care should be taken in the analysis of the results. Overheating the system in the numerical experiment distorts the free energy surface and affects the kinetics of various reactions in different ways, which may complicate the interpolation of the data to experimental conditions. Therefore, static analysis of the potential energy surface at zero temperature is still helpful for supplementing and verifying molecular dynamics results.

2.3 Calculations of threshold energies

The threshold energy of an irradiation-induced process is the minimum energy that must be transferred from an electron of the electron beam (e-beam) to an atom in graphene in order for the process to take place without immediate reversal. Although this can in principle be determined by experiment, due to the development of atomic resolution microscopy, currently there are few examples of experimentally determined thresholds.[146,267] The threshold energy of a process of interest is therefore usually obtained computationally, *via* a series of MD simulations. At the beginning of each simulation, a kinetic energy corresponding to the energy transferred from the beam electron is assigned to the impacted atom. The structural evolution of the entire system over time is then computed using MD in order to determine whether or not the process occurs. This is repeated over a range of initial kinetic energies, and occasionally over a range of impact angles, in order to determine the threshold energy to the desired accuracy. The binary search algorithm has previously been used[225] to choose the value of kinetic energy to apply in order to determine the threshold energy. However, if the computational cost of an individual MD simulation is high while the number of threshold energies to be determined is low (for example when calculating a single threshold energy at a very high level of theory), manual inspection of the MD trajectories and estimation of a suitable kinetic energy based on the results can be more efficient.

In addition to computationally inexpensive classical MD, density functional tight-binding (DFTB) has also been widely used to calculate threshold energies in graphene.[147,151,225,265,268] Its low computational cost relative to DFT enables calculations on systems with large numbers of atoms, or allows a large series of MD simulations to be run in order to obtain precise threshold energies. Apart from calculating threshold energies, DFTB can be generally very useful when modelling the effect of electron impacts on graphene structures, for example in the case of Stone–Wales rearrangements at a variety of impact angles,[147] in which the 27 000 DFTB-MD simulations performed would have been unfeasible at a higher level of theory. Despite the low computational cost, these calculations typically give comparable results to DFT for carbon atoms in graphene, although caution must be used when employing DFTB; emission threshold energies of zigzag edges in graphene for example have been shown to be overestimated by approximately 2.5 eV compared to the DFT case, ascribed to stronger local bonding in the DFTB relaxed structures (shown in Fig. 13).[148] Disparities for other systems have also been shown, such as in hexagonal boron

nitride (h-BN), for which DFTB simulations predicted similar threshold energies for the emission of boron and nitrogen[149] while DFT simulations[150] later agreed with the experimentally shown asymmetry. This discrepancy was assigned to an inadequate description of charge transfer in the DFTB model.

DFT-MD provides an increase in accuracy and versatility compared to DFTB, at the cost of increased calculation time. Calculations using LDA and GGA exchange–correlation functionals are commonly employed in calculations of threshold energies.[148,150,266,269,271] Higher levels of theory, such as hybrid exchange–correlation functionals that include a degree of exact exchange (most notably B3LYP), can be used to obtain more accurate values, but the computational cost of these methods tends to limit the possible system size.

Infinite graphene can be emulated computationally in one of two ways: by using PBC and by using large graphene flakes or nanoribbons. Supercells used in calculations using PBC must be large enough that the atom hit by the electron beam is not influenced by its periodic image, while graphene flakes must be large enough to negate edge effects, shown to extend at least 10 Å from the edge.[67] Simulations using PBC are far more commonly used for calculating threshold energies than large flakes, due to the requirement of a much larger number of atoms to neutralize the large effects of the extended edges compared to a point defect. The atomic processes of structure change studied in graphene in this way typically take of the order of 100 fs to occur when the energies close to the threshold energy are applied, and a 1 fs time step is usually used. Zero-point velocities or thermal vibrations derived from the Maxwell–Boltzmann distribution are used for the initial velocities of other atoms in the system.

2.4 The CompuTEM algorithm

The CompuTEM algorithm[15,151] is a method for linking molecular dynamics and high-resolution transmission electron microscopy (HRTEM) image simulations. The link is established by incorporating structural information from the MD simulations into multislice image simulations, as well as using realistic estimations of the signal-to-noise ratio from the electron dose rate and detector limitations. The effect of the e-beam on a sample is described by incorporating structural changes caused by the electron irradiation from the MD simulations, at realistic rates determined from the electron dose rate and threshold energies. Fig. 1 illustrates this algorithm, in which a random irradiation-induced event occurring in a sequence of such events is described as follows: (1) the nanostructure is equilibrated at a temperature corresponding to experimental conditions in HRTEM, (2) each atom in the nanostructure is classified with respect to the number and strength of its chemical bonds, (3) the probability of an irradiation-induced event (such as atom removal and/or changes to the local atomic structure) is assigned to each atom in accordance with the atom type determined at step 2, so that the sum of the probabilities over all atoms and all considered types of events for each atom is equal to unity, (4) a single random irradiation-induced event is introduced, (5) MD simulation at a temperature corresponding to experimental conditions for a duration sufficient for bond reorganisation or atom removal, (6) MD simulation at the elevated temperature taking into account the structure relaxation after the irradiation-induced event. The introduction of the irradiation-induced event can be described by one of two approaches, an in depth discussion of which can be found in ref. 15.

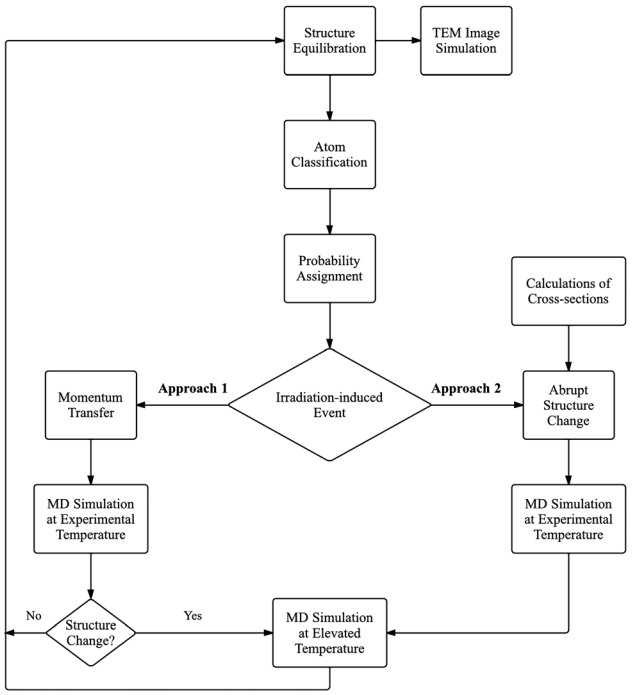

Fig. 1 CompuTEM algorithm for including irradiation-induced structure changes in TEM image simulations. Reprinted (adapted) from ref. 15.

3. Structure and energetics of defects in graphene

3.1 Vacancies

3.1.1 Effects of vacancies on mechanical, electronic and magnetic properties. The influence of vacancies on the physical properties of graphene has been widely studied. The Young modulus,[23–28] Poisson ratio,[25] and tensile strength[22,27,31] of graphene have been shown to decrease with an increase in vacancy concentration. The dependence of fracture strain on the concentration is non-monotonic; there is a decrease in strain at low concentrations and an increase at higher concentrations.[22] A set of calculations demonstrated that the presence of vacancies induces magnetism in graphene.[21,24,35,45–54] According to other calculations the presence of divacancies leads to a decrease of graphene conductivity.[33,34] A decrease in the conductivity of graphene nanoribbons is also observed upon the incorporation of vacancies.[41] Vacancies, as all local defects, do not affect the universal quantization of low-temperature thermal conductance, while they lead to a significant decrease in the thermal conductivity of graphene[26,27,58] and graphene nanoribbons[56,59,60] at room temperature. The thermal conductance of narrow graphene nanoribbons is found

to be very sensitive to the position of the vacancy relative to the edge.[56]

3.1.2 Structure and energetics of monovacancies. Although pioneer works consider the energetics of the monovacancy with D_{3h} symmetry and dangling bonds,[119,152] subsequent calculations showed that the local three-fold symmetry breaks down to C_{2v} symmetry due to Jahn–Teller distortion.[21,25,47,52,153–162] Most of these calculations show that the reconstructed vacancy has a 5/9 structure[21,47,52,67,119,152–162] where a new bond with length b_v arises between a pair of the three atoms with dangling bonds, forming a pentagon with displacement d_v of the third atom out of graphene plane (Fig. 2a). The structure of a reconstructed monovacancy with two new equivalent bonds and without any out of plane displacement of atoms has also been reported.[48] The formation energy of a defect is defined as $E_f = E_d + n\mu - E_p$, where E_d and E_p are total energy of defective and perfect systems, respectively, μ is the chemical potential estimated by calculations as the total energy per atom in graphene, and n is number of removed atoms for vacancies (positive value) or added adatoms (negative value). The values of formation energies E_v and structural parameters b_v and d_v of the monovacancy in graphene calculated using different methods[21,25,35,47,48,52,54,67,119,152–164] are listed in Table 1. To summarise the results presented in Table 1, recent DFT calculations for infinite graphene give vacancy formation energies in the range E_v = 7.6–7.9 eV and the length of the newly formed bond b_v = 1.8–2.0 Å. However, the out of plane distortions caused by defects in graphene are not fully understood. A reliable value for the out of plane displacement d_v has not yet been obtained, as these deformations are highly sensitive to the system size and edge structure (for flake geometries). Note that the calculated value for the length of the newly formed bond coincides with the experimental one b_v = 1.9 Å, measured by an aberration-corrected TEM study.[159] TEM studies cannot directly measure out of plane displacement, however the observation of the projections of two bonds of the third under-coordinated atom of the vacancy being compressed to 1.37 and 1.21 Å (ref. 159) can be considered as an indirect argument that out of plane displacement d_v takes place.

In graphite, the ground state of a single vacancy occurs when it is positioned over the hexagon centre of a neighbouring layer. This configuration has a lower formation energy than a vacancy positioned over an atom of a neighbour layer, by 0.03–0.04 eV for bulk graphite[47,160,165] and 0.03 eV for a graphite surface.[165] The newly formed bonds of this vacancy in graphite are 0.01 Å (ref. 47) and 0.03–0.04 Å (ref. 160 and 165) longer than when positioned over an atom of a neighbour layer. The formation energy of the vacancy on a graphite surface is found to be 0.7 eV lower than for bulk graphite.[165] Analogously to graphite, in AB-stacked bilayer graphene, a monovacancy positioned over a hexagon centre is preferred by up to 0.04 eV compared to a vacancy over a carbon atom.[35,54] The formation energy of a vacancy in twisted bilayer graphene is 0.01–0.07 eV larger than in AB-stacked bilayer graphene, depending on the relative positions of the layers.[35] The energetic and structural parameters of the vacancy in bulk graphite, on a graphite surface and in bilayer graphene, calculated using different methods,[35,47,54,152,160,165,166] are also listed in Table 1. The map of bond lengths around the vacancy in graphite at its ground and transition states has also been presented.[165]

According to DFT calculations, the barrier for transition between the three possible equivalent states of the 5/9 vacancy is only ΔE_t = 0.13 eV. This leads to a small lifetime of t_s = 15 ps and t_s = 32 μs at room and liquid helium temperature, respectively,[153] estimated by the Arrhenius formula (eqn (1)) with a characteristic frequency of $\nu \sim 10^{-13}$ s^{-1}. In the case of such a small lifetime, the superposition of three equivalent states should be observed in TEM observations, which have imaging timescales of the order of one second. However, both the reconstructed 5/9 vacancy[159,167,168] (observed for at least 90 s, ref. 159) and the symmetrical vacancy[159] have been found by HRTEM studies. The authors of this study proposed that the under-coordinated carbon atom is functionalised by a low mass contaminant such as hydrogen, precluding the oscillations between three equivalent states. However, the 80 keV electron beam used in this study should be able to easily remove hydrogen atoms. Note also that these rather old calculations giving the small barrier for transition between three equivalent states of the 5/9 vacancy were performed on a small graphene flake $C_{120}H_{17}$ where the considered vacancy is close to the edge even in the middle of the flake.[153] However as discussed below, the proximity of the edge has drastic effects on the energetic characteristics of the vacancy.[56,67,68] The barrier ΔE_t for transitions between equivalent states of the vacancy should correlate with values of the structural parameters b_v and d_v of the vacancy, which characterise the distortion of the symmetrical vacancy. Table 1 shows the wide spread of these parameters calculated using different methods. Note also the barrier ΔE_t cannot exceed the relaxation energy (the energy difference between vacancies with reconstructed 5/9 structure and the vacancy with all bond lengths as in pristine graphene and three-fold symmetry). The relaxation energy of the vacancy with D_{3h} symmetry into a 5/9 vacancy can be considered as upper estimate of the barrier ΔE_t. DFT-calculated values of this energy are also considerably scattered: 0.9 eV (ref. 156) and 0.29 eV (ref. 53) for graphene, 0.11–0.15 eV for bulk graphite,[165] and 0.14–0.16 eV for graphite surface.[165] Recent studies using density-functional methods show that the vacancy in graphene forms a dynamical JT centre in graphene (where the nuclei tunnel between the minima) owing to the small quantum mechanical barrier for nuclear tunnelling.[169] Note also that calculations for infinite

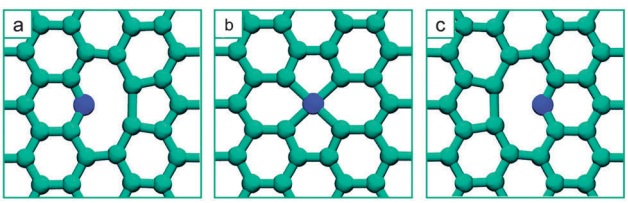

Fig. 2 Initial ground state (a), transition state (b), and final ground state (c) for one migration step of the reconstructed 5/9 monovacancy in graphene. Reprinted (adapted) from ref. 161.

Table 1 Energetic and structural parameters of the reconstructed monovacancy in graphene (see Fig. 2), graphite surface and bulk graphite: formation energy E_v (in eV), barrier ΔE_m for vacancy migration (in eV), bond length b_v of new formed bond and displacement d_v of the atom colored in dark blue out of graphene plane (both in Å). The system considered (periodic boundary conditions (PBC) or flake), number of atoms in the computational cell per layer without the vacancy and calculation method (SP and NSP stand for "spin-polarised" and "non-spin-polarised" calculations, respectively) are indicated

Ref.	System	Number of atoms	Method	E_v	ΔE_m	b_v	d_v
	Single-layer graphene						
21	PBC	128	DFT-PW91, SP	7.7		2.02	0.18
23, 24	PBC	128	DFT-PBE, SP		1.17		
35	PBC	56	DFT-LDA, SP	8.09			
			DFT-PBE, SP	7.72			
			DFT-PBE-D2, SP	7.77			
48	PBC	100	DFT-PW91, SP	7.80		2.40[a]	0[a]
49	PBC	72	DFT-PBE, SP	7.665		1.95	0.184
52	PBC	960	DFT-PBE, SP			1.96	
54	PBC	50	DFT-LDA/DZP, SP	7.83			
		32	DFT-M06-L/6-31G*, SP	7.78			
		50	DFT-vdW-DF/DZP, SP	7.40			
		72	DFT-vdW-DF/DZP, SP	7.44			
154			DFTB[120]	7.38			
155			DFTB[120]	7.6	1.4	~2	
			DFT-PW91	7.7	1.3	~2	
156	PBC	98	DFT-LDA	7.65		2.15	0.43
		200		7.3			
157	PBC	128	DFT-PW91, SP	7.85	1.37	2.37	0.29
158	PBC	72	LAPW[b]-PBE, SP	7.87		2.4	0
159	PBC	200	DFT-PBE			1.90	
160	PBC	288	DFT-LDA(PW91), SP	7.91	1.24	1.83	0
	PBC	288	DFT-PBE, SP	7.36	1.25	1.80	0
162	PBC	128	DFT-PBE/DNP, SP	7.73			
163	PBC	144	DFT-PW91, SP	7.63			
164	PBC		DFT-LDA, SP	7.40		2.10	
			DFTB, SP	7.51	1.29	2.20	
173	PBC	128	DFT-LDA, NSP		0.91		
			DFT-LDA, SP		1.01		
67	Flake C_{116}		DFT-B3LYP/6-31G*, SP	8.0		1.73	
153	Flake $C_{120}H_{17}$		DFT, NSP	7.4	1.6	2.1 ± 0.1	
25	PBC	968	TB model[119]	6.89		1.7	0.1
119	PBC	112	TB model[119]	7.3	1.0	—[c]	—[c]
	Graphite surface						
35	PBC[d]	56	DFT-LDA, SP	8.03			
			DFT-PBE, SP	7.71			
			DFT-PBE-D2, SP	7.72			
47	PBC[d]	256	DFT-LDA, SP			1.79	
54	PBC[d]	32	DFT-LDA/DZP, SP	8.01			
			DFT-M06-L/6-31G*, SP	7.90			
			DFT-vdW-DF/DZP, SP	7.50			
		50	DFT-vdW-DF/DZP, SP	7.42			
165	PBC[e]	96	cDFT[f]-PW91, SP	7.87	0.99		
	Bulk graphite						
152	PBC[g]	18	DFT-LDA	7.6	1.6	—[c]	—[c]
160	PBC[h]	288	DFT-LDA(PW91), SP	7.96	1.07	1.89	0
			DFT-PBE, SP	7.35	1.15	1.86	0
165	PBC[h]	64	cDFT[f]-PW91, SP	8.58	1.4	2.11	0
166	PBC[i]	18	DFT-PW91, NSP	7.6			

[a] The structure of reconstructed vacancy not is not 5/9 state, see text. [b] All-electron density-functional linear augmented plane wave method (LAPW). [c] Optimisation of structure is restricted by consideration of symmetrical vacancy. [d] Bilayer graphene in AB stacking. [e] Upper layer of three-layer graphene. [f] DFT with empirical van der Waals correction. [g] Three layers of graphite in ABC stacking. [h] Two layers of graphite in AB stacking. [i] Three layers of graphite in ABA stacking.

graphene based on the tight-binding (TB) model give a considerably greater barrier for the transition between equivalent states of vacancy, ΔE_t = 0.78 eV,[142] than the DFT calculations for the small graphene flake. Thus further experimental and theoretical studies are necessary to clarify the ground state structure of the vacancy in graphene.

3.1.3 Structure and energetics of divacancies. Three different reconstructed states of the divacancy in graphene are commonly observed on graphene under electron irradiation in HRTEM:[65,147,167,170] the V_2(5-8-5), V_2(555-777) and V_2(5555-6-7777) states, see Fig. 3. Divacancies with the 5-8-5 structure were also found by scanning tunnelling microscopy in Ar^+ irradiated graphene.[171] 60 kV HRTEM studies of monolayer graphene following bombardment with energetic gold particles allowed observation of the unreconstructed divacancy.[172] The transitions between the three reconstructed divacancy states under electron irradiation were observed in HRTEM.[65,147,167] The formation energies of the V_2(5-8-5) and V_2(555-777) divacancies

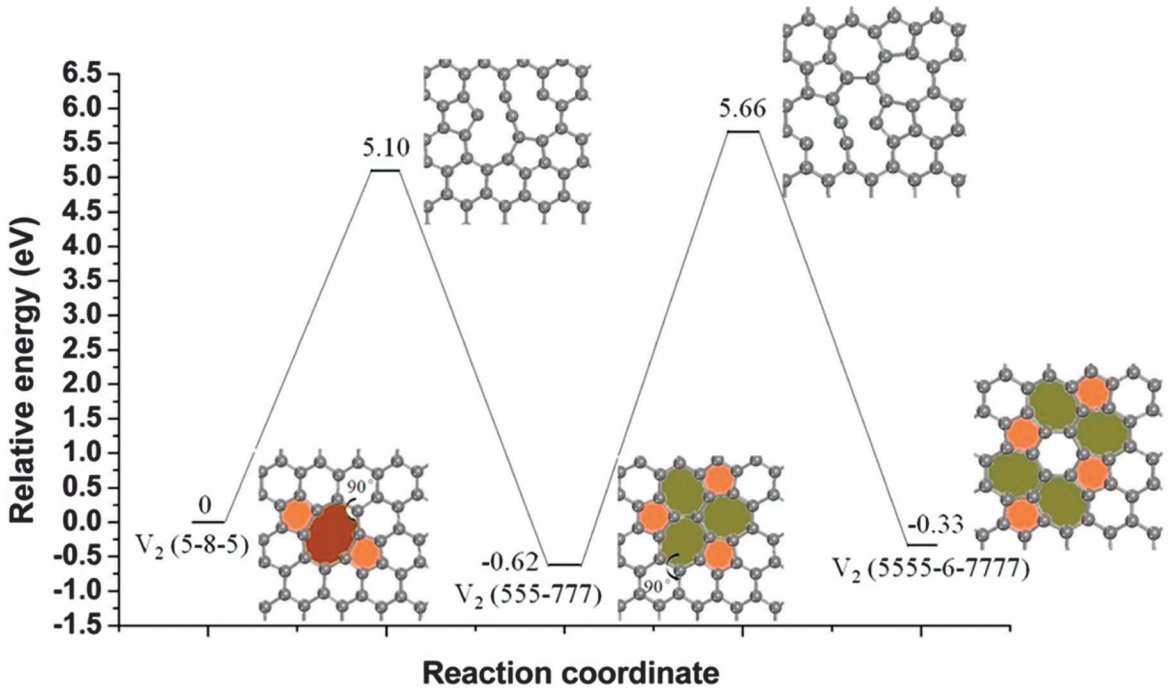

Fig. 3 Schematic representation of the structure and energetics for three states of a divacancy in graphene: V_2(5-8-5) state, V_2(555-777) state and V_2(5555-6-7777) state, and transition states for transition between V_2(5-8-5) and V_2(555-777) states and between V_2(555-777) and V_2(5555-6-7777) states. Reprinted (adapted) with permission from ref. 162. Copyright (2013) American Chemical Society.

and one structural parameter of V_2(5-8-5) divacancy in graphene,[25,33,34,49,50,153,154,156,157,160,162–164,171,173] calculated using TB,[119–121] and DFT methods, are listed in Table 2. To summarise the results presented in Table 2, recent DFT calculations for infinite graphene give formation energies of the V_2(5-8-5) divacancy in the range E_{2v} = 7.5–8.0 eV and energy gains for the transition from the V_2(5-8-5) to the V_2(555-777) state in the range ΔE_2 = 0.8–1.0 eV. The energy gain due to the transition from the V_2(5-8-5) to V_2(5555-6-7777) state was calculated to be 0.33 eV.[162] Maps of bond length changes around the divacancy have been presented.[25,161] The calculations of divacancy energetics in graphene and molecular dynamics simulations of its dynamical behaviour at high temperature (3000–4000 K) have also been performed[174] using the AIREBO potential. These calculations show that this potential gives the correct ground state of the divacancy but the wrong ground state of the monovacancy. Although 18 other possible states of the divacancy have been found during these simulations, these can only be considered as a qualitative description of possible divacancy metastable states. The barriers and transition states for transformation between the V_2(5-8-5) and V_2(555-777) states and between the V_2(555-777) and V_2(5555-6-7777) states have been found by DFT calculations[162] and are shown in Fig. 3. Close values of the barrier for the V_2(5-8-5) to V_2(555-777) transformation were found by other DFT studies, 5.27 eV,[170] 5.17 eV (ref. 173) and 5.1 eV.[160] All three states of divacancy are therefore stable at room temperature.

Table 2 Energetic and structural parameters of reconstructed divacancies in graphene (see Fig. 3): formation energy of the V_2(5-8-5) divacancy E_{2v} (in eV), energy difference between the V_2(5-8-5) and V_2(555-777) states of divacancy ΔE_2 (in eV) and bond length d_v of newly formed bond of pentagon of V_2(5-8-5) divacancy (in Å). The system considered (periodic boundary conditions (PBC) or flake), number of atoms in the computational cell per layer without the vacancy and calculation method (SP and NSP stand for "spin-polarised" and "non-spin-polarised" calculations, respectively) are indicated

Ref.	System	Number of atoms	Method	E_{2v}	ΔE_2	d_v
49	PBC	72	DFT-PBE, SP	8.998		1.78
50	PBC	72	DFT-PBE, SP	6.37		
154			DFTB[120]	7.52		
162	PBC	128	DFT-PBE/DNP, SP	6.79	0.62	
157	PBC	128	DFT-PW91, SP	7.53		1.82
171	PBC	128	DFT-vdW-DF/DZP	7.8	0.8	
160	PBC	288	DFT-LDA(PW91), SP	7.81	0.92	
		288	DFT-PBE, SP	7.11	1.07	
156	PBC	98	DFT-LDA	7.59		1.77
163	PBC	144	DFT-PW91, SP	8.08		
173	PBC	128	DFT-LDA, SP, NSP		0.91	
			DFT-PW91		0.90	
33, 34	PBC	98	DFT-LDA/DZP, NSP		0.9	
164	PBC		DFT-LDA, SP	8.25		1.72
			DFTB, SP	8.19		1.69
153	Flake $C_{120}H_{17}$		DFT, NSP	8.7		
25	PBC	968	TB model[119]	7.52	0.47	1.66

3.1.4 Structure and energetics of multi-vacancies. A set of studies is devoted to the structure and energetics of trivacancies and multi-vacancies in graphene, obtained by structure reconstruction after the removal of neighbour atoms without bond rearrangements.[49,50,156] The trivacancy with this structure was obtained by bombardment with energetic gold particles.[172] For the vacancies with structures in which an odd number of carbon atoms are missing, at least one dangling bond persists,

whereas for structures missing an even number of atoms (2, 4 and 6 missing atoms) more stable structures lacking dangling bonds are possible.[49,156] Other interesting types of multi-vacancies form in graphene as a result of vacancy coalescence and then subsequent bond rearrangement under electron irradiation in HRTEM.[65,66,167] In the case of multi-vacancies with an even number of missing atoms, the formation of lines of two or three V_2(5-8-5) vacancies is observed in the graphene membrane under electron irradiation in HRTEM.[65,66,167] In such pairs or lines, adjacent divacancies have a common pentagon when aligned in the zigzag direction, while a tetragon is formed when aligned in the armchair direction, due to the overlap of two pentagons. The DFT-calculated energy gain is 1.32 and 2.01 eV per divacancy pair, as compared to isolated divacancies, for alignment in the zigzag and armchair directions, respectively.[167] The multi-vacancy created by combining two and three V_2(5555-6-7777) divacancies has been considered.[167] The DFT-calculation-based comparison of formation energies for several types of multi-vacancies in graphene with even missing atoms has also been performed.[50,175,176] For the case of multi-vacancies with odd numbers of missing atoms, the formation of a bridging atom stabilizing the structure is observed in HRTEM.[66] The DFT-calculated energy gain is 1.55 eV for a trivacancy with a bridging atom, as compared to a trivacancy with a dangling bond.[66]

3.1.5 Vacancy migration. Recent DFT calculations of formation energies of mono- and divacancies in infinite graphene[50,156,157,160–163] show that the V_2(5-8-5) divacancy has a 7.2–8.7 eV lower energy than a pair of separated vacancies. This means that the coalescence of two monovacancies into one divacancy is an exothermic process, which can take place *via* the thermally activated diffusion of vacancies or under electron and ion irradiation. In a similar manner, trivacancies have a lower energy than a separated monovacancy and divacancy, and so on.[49,156] The coalescence of large numbers of vacancies can lead to the formation of amorphous graphene structure.[146] The directed motion of a vacancy to the edge, due to a decrease in total energy at each step towards the edge, has been proposed based on DFT calculations[67,68] and molecular dynamics simulations.[67] The rates of the above processes are determined by the barriers for vacancy motion. The structures of the initial, transition and final states corresponding to one step of monovacancy motion is shown in Fig. 2. The transition state is a so-called spiro structure, where the moving atom is of equal distance to four nearest neighbours.[161,165] Note that due to the high symmetry of the spiro structure it should correspond to the minimum, maximum or saddle point of the potential energy of the system. The described step of vacancy migration was directly observed by a TEM study.[159] It is interesting to note that during the time between two subsequent image exposures, this TEM study observed the migration of a vacancy by two steps significantly more frequently than the migration by one step. Calculated values of the barrier ΔE_m of migration of a vacancy in graphene,[23,24,152,153,155,157,160,164,173] bulk graphite[152,160,165] and on the graphite surface[165] are listed in Table 1. Some DFT calculations give the value of the barrier ΔE_m of migration of a vacancy in graphite as being 0.15–0.26 eV lower than in graphene,[160] whereas DFT calculations with an empirical van der Waals correction give the opposite result; the barrier ΔE_m is greater for graphite by 0.4 eV compared with the graphite surface.[165] Only two experimental estimates of the barrier ΔE_m are currently available for bulk graphite and its surface. The first, $\Delta E_m = 1.8 \pm 0.3$ eV, was obtained by Raman measurements of disorder relaxation in He^+ irradiated graphite.[177] Recent STM studies of vacancy aggregation on vacancy-decorated graphite surfaces at different temperatures give the value ΔE_m = 0.9–1 eV.[178] The calculated values of ΔE_m listed in Table 1 range between these two experimental estimates and are only in tentative agreement with few experiments. Further studies are necessary to obtain accurate values of the barriers for migration of vacancy in graphene, bulk graphite and graphite surface.

Contrary to monovacancy migration, the barrier for divacancy migration is considerably large. The estimation of this barrier for a small graphene flake ($C_{120}H_{17}$) gives the value of about 7 eV.[153] An estimation based on migration in two steps, *via* the dissociation and merging of two vacancies, gives the value 7.49 eV.[157] HRTEM studies reveal the migration of the V_2(5-8-5) divacancy under the action of electron irradiation through the formation of an intermediate metastable dislocation dipole (the V_2(55-77) state).[167,170] Divacancy migration under electron irradiation in HRTEM has also been observed as a result of transitions between the V_2(5-8-5), V_2(555-777) and V_2(5555-6-7777) divacancy states.[147,170] It has been found using DFT calculations in combination with careful analysis of HRTEM images that one step of the migration of the V_2(5-8-5) divacancy occurs through two intermediate V_2(55-77) states which have a higher total energy by 3.44 eV (other DFT calculations 3.72 eV (ref. 167)). The barrier for transformation from the V_2(5-8-5) to V_2(55-77) state is 5.27 eV, whereas the migration of the V_2(555-777) divacancy occurs through a transformation to the V_2(5-8-5) state with a barrier of 6.20 eV.[170] Thus, thermally activated migration of divacancies at room temperature can be excluded.

3.1.6 Effects of edges and deformation on the energetics of vacancies. The structure and energetics of the monovacancy near the edge of the graphene layer have been studied on examples of narrow graphene nanoribbons with the vacancy in the middle,[52,56] graphene flakes with dangling bonds at the edge[67] and graphene flakes with the edge terminated by hydrogen atoms[68,69] with different positions of the vacancy. Note that the case of an edge with dangling bonds is realised under the action of electron irradiation in TEM and is important when considering irradiation-induced processes such as the graphene flake to fullerene transformation.[8] It is evident that the structural parameters and formation energy of vacancies should change near the edge. For armchair graphene nanoribbons with widths of 7 and 5 hexagons, a stronger new bond is formed for the reconstructed 5/9 vacancy with the length b_v of 1.9 and 1.8 Å, respectively, slightly less than the value b_v = 1.96 Å obtained for bulk graphene using the same parameters of spin-polarised DFT calculations.[52] DFT-calculated formation energies of reconstructed 5/9 vacancies in the middle of graphene flakes (ranging in size from C_{52} to C_{116}) with dangling bonds at the edge[67] are listed in Table 3. Table 3 also presents the difference ΔE in the

Table 3 The DFT-calculated energy characteristics of flakes with a monovacancy located at distance d (in Å) from the edge: E_v (in eV) is the energy of vacancy formation, and ΔE (in eV) is the difference in the total energy between a flake with the vacancy in the middle and at the edge. Reprinted (adapted) from ref. 67

Flake	E_v	ΔE	d
C_{52}	6.8	7.3	4.3
C_{69}	7.3	6.6	7.1
C_{88}	7.3	7.3	7.1
C_{103}	7.7	8.9	8.6
C_{116}	8.0	7.6	8.6

total energy of the flake with the vacancy in the middle and at the edge. A considerable difference of ΔE = 6.6–8.9 eV in the total energies has been found for all flakes. The total energies corresponding to the subsequent steps of vacancy motion from the middle to the edge have been calculated for the C_{116}[67] and $C_{41}H_{16}$[68] graphene flakes.

Moreover, upon decreasing the distance between the vacancy and the graphene layer edge, a change of energetic and structural parameters of the reconstructed 5/9 vacancy is predicted, as well as a drastic change of the whole vacancy structure.[56,67,68] DFT calculations show that the vacancy in the middle of an armchair graphene nanoribbon with the width of 5 hexagons has a spiro ground state with an sp^3 atom with four equivalent bonds 1.64 Å in length[56] in the centre of the vacancy (the same bond lengths as in the spiro state monovacancy in the middle of the C_{116} graphene flake[67]). The coexistence of the 5/9 and spiro states of the monovacancy near the graphene edge has been obtained by DFT calculations for graphene flakes with both dangling bonds[67] and hydrogen atoms[68] at the edge. It was also found that the spiro state of the vacancy is more stable than the 5/9 state in the middle of a graphene flake with hydrogen atoms at the edge when the distance between the vacancy and the edge is less than 7 Å.[68] Furthermore, these calculations give the stable spiro state of the vacancy even at a distance of 15.6 Å from the edge,[68] contrary to in infinite graphene where it corresponds to a saddle point.[161] Note that calculations using the old version of the Brenner potential gives the 5/9 structure for the ground state of the vacancy whereas the new version of this potential gives the spiro structure.[154] The influence of the vacancy on the surrounding structure is more significant near the edge than in infinite graphene. For flakes consisting of approximately one hundred carbon atoms, the presence of a vacancy in the centre resulted in considerable bending of the entire structure, for both flakes with dangling bonds at the edge[67] and flakes terminated at the edge by hydrogen atoms.[69,153] Vacancies in the spiro state in the middle of narrow graphene nanoribbons causes them to coil into spiral helices.[68]

The vicinity of the edge has an even more drastic effect on vacancy migration than on its structure and energetics.[67,68] As both 5/9 and spiro states of the vacancy near the graphene edge correspond to local potential energy minima, the only vacancy migration step near the edge is the transition between the 5/9 and spiro states.[67] The scheme of possible vacancy migration steps near the edge is presented in Fig. 4. A transition from the initial 5/9A state to two spiro states SA and SB is possible. Four transitions are possible from each spiro state SA and SB, which can be achieved by breaking one of the four bonds: a return to the initial 5/9A state, transition to another 5/9 state of

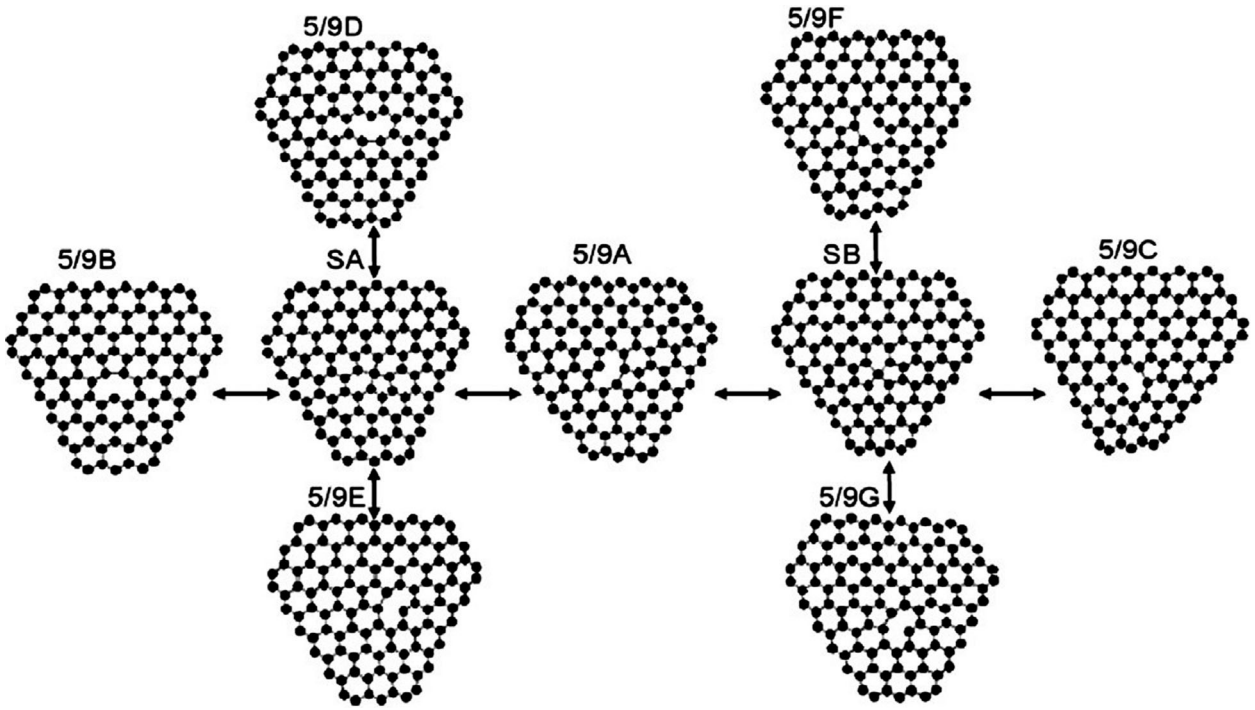

Fig. 4 Scheme of possible transitions between the neighbouring 5/9 and spiro vacancy states in the middle of the C_{116} flake. Reprinted (adapted) from ref. 67.

the same vacancy (5/9B and 5/9F) and migration of the vacancy (5/9C, 5/9D, 5/9E, and 5/9G).[67] The energies of local minima and transition states for vacancy migration in the middle of the C_{116}[67] and from the middle to the edge of the $C_{41}H_{16}$[68] graphene flakes have been calculated. These calculations reveal that the barrier for vacancy motion towards the edge is considerably lower than the barrier for motion away from the edge. Thus, both the difference in the total energy of graphene with the vacancy at the edge and at distance d from the edge (see Table 3) and the barrier to vacancy migration decrease with the decrease of distance d. This leads to the conclusion that thermally activated directional motion of the vacancy towards the edge should take place,[67,68] as confirmed by molecular dynamics simulations.[67] As these barriers for the vacancy motion towards the edge are smaller than barriers for vacancy motion in infinite graphene, the motion to the edge will occur too fast to be observed by STM or TEM studies at room temperature.

According to DFT calculations, a 3% compression of graphene leads to a change in the ground state of the vacancy to the spiro state.[51] The deformation of graphene also exerts considerable influence on the barriers ΔE_m for vacancy migration. DFT calculations show that the value for pristine graphene ΔE_m = 1.17 eV changes to 3.15 and 0.75 eV for elongation by 5% in the armchair and zigzag directions, respectively, and to 0.12 and 1.79 eV for compression by 5% in armchair and zigzag directions, respectively.[23] Thus the possibility of directional motion of vacancies caused by applied graphene layer deformation has been proposed.[23]

3.1.7 Interaction and coalescence of vacancies. A set of studies is devoted to the interaction of vacancies and their coalescence into divacancies.[50,142,157,160,162,173] This set includes a TB molecular dynamics study of the convergence and coalescence of vacancies,[173] action-derived molecular dynamics for energetics of certain paths of vacancies migrating towards each other,[142] DFT calculations of energies of the subsequent states at the convergence of vacancies and barriers between these states,[160,162] and barriers of the final step of coalescence of pairs of vacancies.[157,160,162,173] The formation energy of vacancies in graphene as a function of their concentration has also been studied.[50] Thorough DFT calculations give the energies of pairs of vacancies for different neighbour locations, as well as barriers to transition between these locations.[160] The barriers for the final step of coalescence of a pair of vacancies into a V_2(5-8-5) divacancy are found in this work to be 2.10 and 0.82 eV, for different final neighbour locations[160] (in agreement with previous DFT calculations: 1.52 eV (ref. 173) and 2.17 eV (ref. 157)). Another DFT study revealed two different transition paths for the final step of coalescence into the V_2(5-8-5) divacancy, with barriers of 1.17 and 1.92 eV.[162] Two examples of energy changes for the migration towards and coalescence of vacancies, based on a TB model, are shown in Fig. 5.[142] These calculations give the values of the barrier for the final step of coalescence as 1.3 and 1.9 eV for different approaching pathways with V_2(555-777) divacancy formation. Detailed DFT-calculated maps of energies of vacancies located near the V_2(5-8-5) divacancy and a trivacancy, as well as transition barriers between neighbouring vacancy positions, have been used to study the dynamical evolution of the coalescence of monovacancies with divacancies and trivacancies by kinetic Monte Carlo simulations.[161] Analogously to the coalescence of a pair of monovacancies, the barriers for the final stage of coalescence depend on the pathway of the vacancy approaching the di- and trivacancies. These barriers lie in the range 0.9 to 4.7 eV and 0.9 to 1.5 eV for different neighbour positions for the V_2(5-8-5) divacancy and trivacancy, respectively.[161] Examples of the final steps of coalescence of the monovacancy and V_2(5-8-5) divacancy are shown in Fig. 6.

3.2 Adatoms

The healing of various defects of graphene by the migration of adatoms has been observed by HRTEM.[64,65] Possible magnetism of adatoms on graphene has been discussed,[179,180] and the structure and energetics of the adatom on graphene have been considered in a set of papers.[157,163,179–183] A DFT study gives three stable positions of the adatom on graphene: a bridge position over the centre of a bond, a dumbbell arrangement where the adatom has bonds with three atoms of graphene, and an off-top structure where the adatom and one atom of graphene each have four bonds and the same position relative the graphene plane.[181] The bridge position is found to be a ground state,[166,179,181] with the dumbbell arrangement and off-top structure having 0.37 and 0.22 eV higher energies, respectively.[181] The bridge position of an adatom on graphene was observed by HRTEM[184] and scanning transmission electron microscopy (STEM).[185] DFT calculations give the adsorption energy of an adatom as 1.40 eV (ref. 179) and 1.7 eV (ref. 53 and 166) and low values for the barrier to adatom migration on graphene: 0.35 eV,[53] 0.45 eV,[183] 0.47 eV,[179] 0.52 eV,[163,180] and 0.53 eV.[157] The DFT-based TB method gives the same ground state bridge position of the adatom, and close values of the adsorption energy (2 ± 0.3 eV) and barrier for migration (0.4 ± 0.1 eV).[182,183] The migration of adatoms can therefore easily take place at room temperature. DFT calculations predict an energy gain of up to 0.25 eV for close positions of neighbour adatoms, with a decrease of the barrier to migration to only 0.225 eV,[180] meaning that the agglomeration of adatoms at low temperatures is possible. The structure and energetics of adatom pairs on graphene (*i.e.* the case where chemical bonds exist between adatoms) have been also considered by DFT.[181] The most stable pair is found to be the so-called 7-5-5-7 defect that is comprised of two pentagons and two heptagons and introduces a local elevation of 2 Å out of the graphene plane.

As monovacancies can easily migrate and merge into divacancies, whereas thermally activated migration of divacancies is not possible, the interaction of adatoms with divacancies is an important process observed by HRTEM.[184] DFT energy calculations of states of an adatom and divacancy approaching one another, as well as the barriers between these states, have been performed.[162,163] For the V_2(5-8-5) divacancy, the coalescence of the divacancy and adatom takes place with three barriers during the approach of the adatom (0.91, 0.73 and 1.36 eV) before the coalescence and a total energy release of 5.79 eV,[162] whereas a different study gives even higher barriers

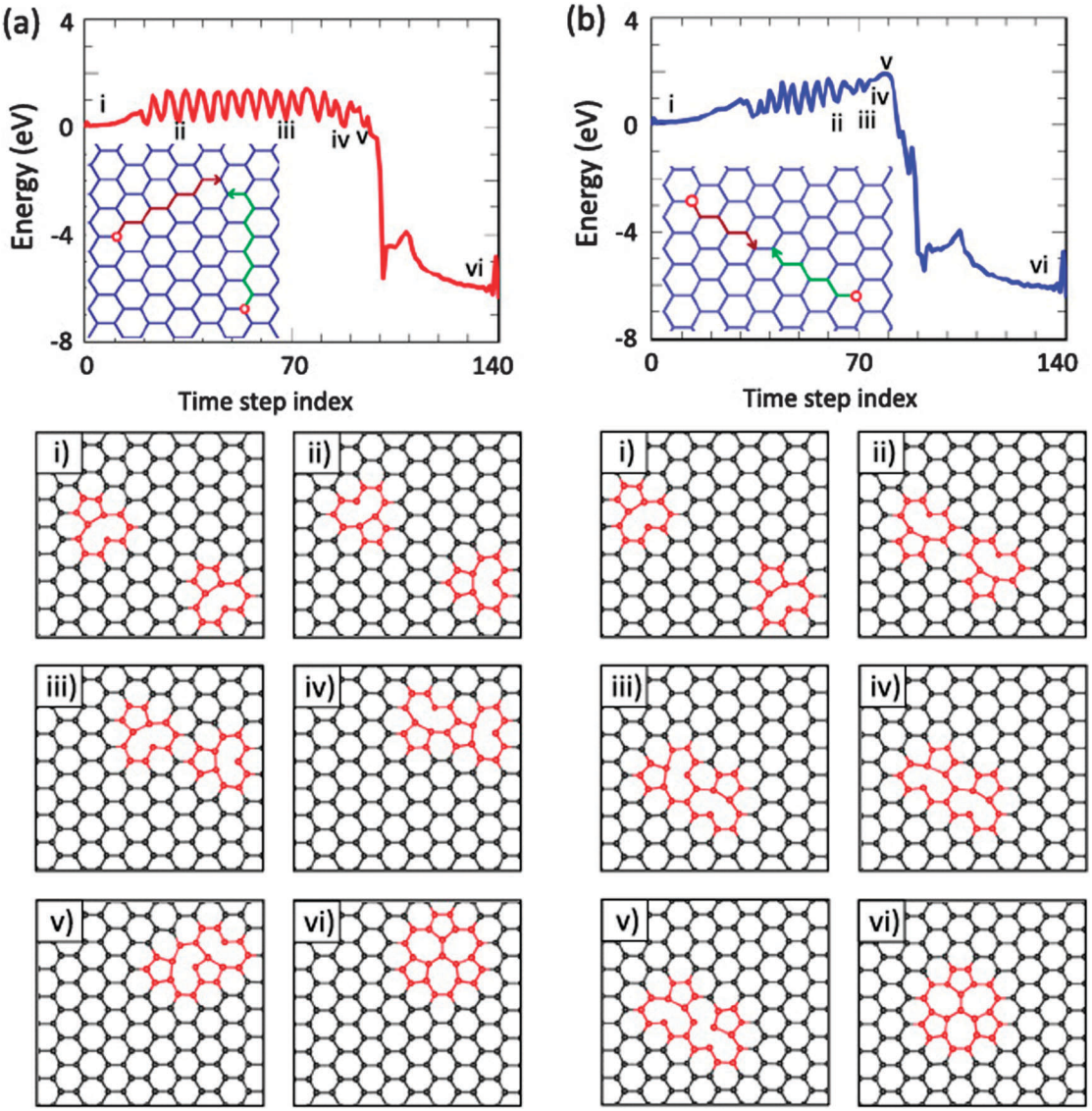

Fig. 5 The process of merging monovacancies into a V_2(555-777) divacancy for different pathways for the approaching migration of vacancies. The potential energy of system relative to the initial state along migration pathways is shown as function of time step index in action-derived molecular dynamics simulation. Reprinted (adapted) from ref. 142. Reproduced by permission of IOP Publishing. All rights reserved.

of 1.55 and 2.49 eV between neighbouring bridge positions near the V_2(5-8-5) divacancy.[163] Thus a state in which an adatom near a V_2(5-8-5) divacancy is stable at room temperature is possible, in agreement with HRTEM observations.[184] However, the adatom does not coalesce with the V_2(555-777) divacancy – a dumbbell-like configuration is formed where the adatom is adsorbed over the central atom of the V_2(555-777) divacancy.[162] The motion of the adatom to this final location occurs with the subsequent barriers 0.43, 1.00, 0.78, 0.39 and 0.56 eV and the total energy release is 1.8 eV. The creation of an inverse Stone–Wales defect on the periphery of a divacancy, by one adatom hopping within the vicinity of another, was proposed.[163]

3.3 Topological defects and bond-realignment reactions

An important class of reactions in carbon nanostructures is related to bond rotations that lead to the formation or transformation of topological defects, while not being accompanied by a loss or addition of atoms. The simplest example of such a reaction is the 90 degree rotation of a bond in a perfect hexagonal network, leading to the formation of a Stone–Wales (SW) defect[72,168] comprised of two pentagons and two heptagons (Fig. 7a).

3.3.1 Effects of SW defects on mechanical, electronic and magnetic properties. SW defects only very weakly affect the elastic properties of graphene such as the Young modulus[26–30] and Poisson ratio,[30] although this effect becomes more pronounced with increased defect concentrations.[26–28] Numerous studies show that pre-existing SW defects serve as nucleation centres for fracture[22,27] and substantially decrease the failure strain and tensile strength of graphene.[22,27,29,31,32] The accumulation of SW defects in graphene degrades the ultimate tensile strength and failure strain to saturated levels that are 30–50% lower than in pristine graphene.[22,27] The SW transformations

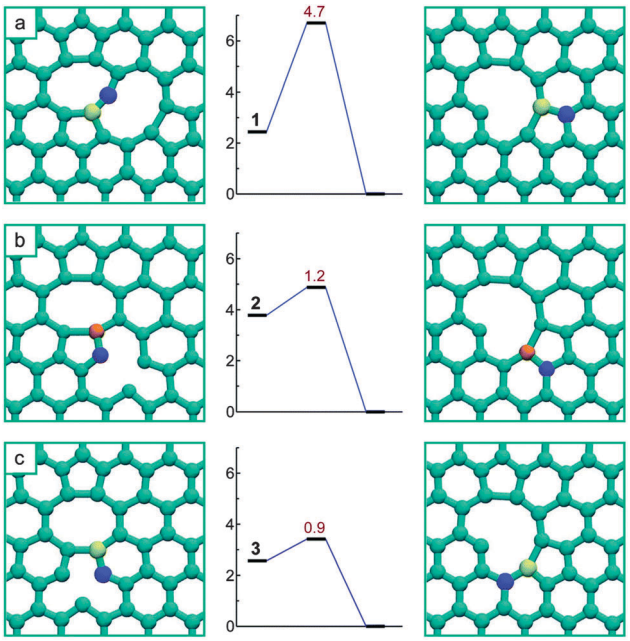

Fig. 6 The final steps of the merging of a 5/9 monovacancy with a V_2(5-8-5) divacancy, from the three non-equivalent 3rd nearest neighbour positions (a), (b), and (c), where the two atoms involved in each transition have been coloured to track their movement. The energies of initial and transition states relative the final state are indicated. Reprinted (adapted) from ref. 161.

are also direct participants of plastic deformation in graphene, which is discussed below.

The analysis of the density of states in graphene showed that p_z orbitals of the carbon atoms of the rotated bond in SW defects give rise to a defect band $\sim$0.5 eV above the Fermi level, with the width and height dependent on the defect concentration.[33–40] The conductivity of defected graphene exhibits systematic degradations around defect resonance energies.[33,34] Electron backscattering regions are also introduced in transmission spectra of graphene nanoribbons with SW defects.[41–44] SW defects generally do not carry a magnetic moment[33–35,40] and are neutral,[40] although some charge transfer was detected between layers of defected bilayer graphene[35] and asymmetric arrangements of SW defects in graphene nanoribbons can affect their magnetic moment.[55] The effect of SW defects on the thermal conductivity of graphene[26,27,57,58] and graphene nanoribbons[59–61] is similar to that of other local defects, such as vacancies.

3.3.2 Structure and energetics of SW defects. The combined DFT[35,36,54,70,164,166,186–188] and TB data[164,189] show that the formation energy of a SW defect in a graphene layer is 4.5–5.0 eV (Table 4). A slightly larger formation energy (by 0.3 eV) is predicted on the basis of quantum Monte Carlo (QMC) simulations.[186] Significant variations[35,36,53,54,70,91,119,152,164,166,173,186–194] are observed depending on the supercell used in the calculations (Table 4), due to interactions of periodic images of SW defects through generated long-range stress and strain fields.[190,191] In the calculations for finite graphene flakes, the formation energy[195–198] of SW defects might be affected by the vicinity of the edges. While the results of TB methods[119,121–123] are very close to those of DFT,[188] the semiempirical potentials[127–129] and continuum models[199] are

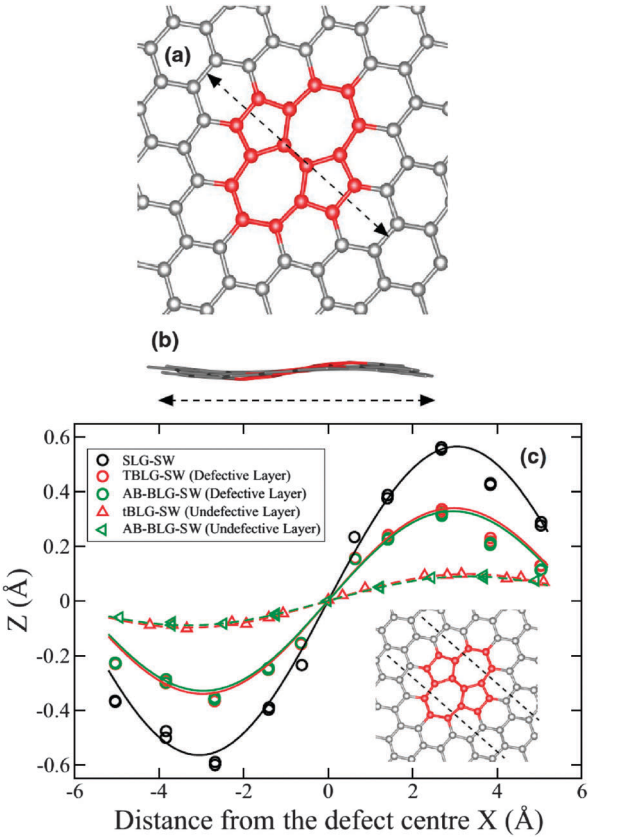

Fig. 7 Structure of the SW defect in single-layer graphene (SLG): (a) top view and (b) side view showing the distortion of the defective graphene sheet. The side view in (b) is taken by viewing perpendicular to the dashed line in (a). (c) The distortion pattern for the SW defects in SLG, twisted bilayer graphene (TBLG) and bilayer with the AB stacking (AB-BLG). A distortion amplitude of zero corresponds to the centre of the SW defect. The dashed line in the inset encloses the atoms over which the deviations from zero are measured. Reprinted (adapted) from ref. 35. Copyright (2014) by the American Physical Society.

not very accurate in exact numerical values for energies.[70,71,138,200–202] However, they give the correct trends and qualitative behaviour for bond realignment reactions.[70,91,188,202–204]

It is seen that although all atoms in a SW defect have the same number of bonds as in the perfect hexagonal network, it has a significant formation energy. The reason is that upon the SW rotation, many bonds get compressed or stretched[36,152,164,166,186,198,205,206] (Table 5), and the angles between the bonds deviate from 120°. The angle of the pentagons at the atoms forming the rotated bond was calculated to be 115.5°,[36] 115.0°[206] and 118.2°.[205] The most deformed bond is the central rotated bond (separating two heptagons in the SW defect), which experiences compression by almost 10% (Table 5 and Fig. 8a).[152,164,166,186,198,205,206] Some compression is also observed for the bonds between pentagons and hexagons, while the bonds between heptagons and hexagons and the bonds between heptagons and pentagons are stretched[152,164,166,205,206] (Fig. 8a). This behaviour is in agreement with general observations that pentagons and heptagons are centres of compression and tensile stress, respectively.[207–210]

Table 4 Formation energy E_{SW}, activation energy $E_{a,SW}$, energy gain from out-of-plane buckling δE_b (in eV) and maximum difference in out-of-plane coordinate of atoms h (in Å) for SW defects in single-layer and bilayer graphene and graphite. The system considered (periodic boundary conditions (PBC) or flake), number of atoms in the computational cell per layer and calculation method are indicated

Ref.	System	Number of atoms in cell	Method	E_{SW} (eV)	$E_{a,SW}$ (eV)	δE_b (eV)	h (Å)
	Single-layer graphene						
35	PBC	56	DFT-LDA	5.25		0.22	1.2
			DFT-PBE	5.14		0.21	
			DFT-PBE-D2	5.09		0.23	
36	PBC	98	DFT-LDA	5.16		0.28	1.3
		Infinite-size limit	DFT-LDA	4.66			
53	PBC	128	DFT-PBE	5.70			
54	PBC	72	DFT-LDA/DZP	4.43			
	PBC	50	DFT-LDA/DZP	4.29			
			DFT-M06-L/6-31G*	4.31			
			DFT-vdW-DF/DZP	4.26			
70	PBC		DFT	5.16	9.91		
91	PBC		DFT-PBE	5.4	9.4		
166	PBC	50	DFT-PW91	4.8	9.2		
			DFT-LDA	5.2	9.4		
186	PBC	242	DFT-PBE	4.59		0.231	1.61
	PBC	50	DFT-PBE	5.26		0.269	1.16
			DFT-LDA	5.42		0.210	1.07
			DFT-PBE0	5.63		0.061	0.79
			QMC	5.82 ± 0.03		0.096 ± 0.020	
164	PBC		DFT-LDA	4.86			
			DFTB[121]	4.85	10.4		
187	PBC	98	DFT-GGA	3.83			
190, 191	PBC	32–192	DFT-LDA	4.20 to 5.90			
188	PBC		DFT-LDA	5	9.9		
192	PBC	60	DFT-LDA	5.4, 4.8[a]			
193	PBC	128	DFT-LDA/DZ, PW	5.9	11.0, 10.3		
	Adatom-catalysed			2.6	4		
194	PBC	48	DFT-PBE	4.82	9.3	0.07	
195	Flake $C_{248}H_{42}$		DFT-PBE/3-21G		10.0		
196	Flake $C_{62}H_{20}$		DFT-LDA	3.4	9.0		
	Adatom-catalysed			1.6	2.3		
198	Flake, $C_{42}H_{16}$		DFT -B3LYP/6-31G(d)		6.2		
	Adatom-catalysed				0.86		
197	Flake, 6 shells		Hückel		6.02		
173	PBC	128	TB model[123]		10.2		
189	PBC	572	TB model[122]	4.43			
119	PBC	112	TB model[119]	5.8	9.8		
200	PBC		Tersoff–Brenner[128]		5.9		
138	PBC		Tersoff–Brenner[128]	3	6		
202	PBC		Tersoff–Brenner[128]	2.54	6.16		
70, 71	PBC		Tersoff–Brenner[128]	4.43	7.88		
199	PBC		Classical continuum model	3.7			
	PBC		Gauge field theory	3.2			
	Bilayer graphene[b]						
35	PBC	56	DFT-LDA	5.39		0.08	
			DFT-PBE	5.15		0.23	
			DFT-PBE-D2	5.27		0.04	
54	PBC	72	DFT-LDA/DZP	4.66			
	PBC	50	DFT-LDA/DZP	4.93			
			DFT-M06-L/6-31G*	5.15			
			DFT-vdW-DF/DZP	4.83			
	Bulk graphite[c]						
152	PBC	18	DFT-LDA	10.4	13.7		

[a] Dependent on orientation. [b] With AB stacking. [c] Graphite with ABC stacking.

Geometrical optimisation of a SW defect starting with all atoms in the same plane yields a flat SW defect structure.[119,152,166,190,191,205] However, this structure has two imaginary frequencies, and the true minimum is characterised by the carbon atoms forming the rotated bond at the defect core buckling out-of-plane above and below the graphene plane[35,36,186,194] (Fig. 7b). The energy gain from out-of-plane buckling of the core atoms is 60 – 300 meV depending on the method used and the supercell considered,[35,36,186,194] and comes from slight elongation of the compressed rotated bond at the defect core.[186] The maximum displacement between atoms perpendicular to the graphene plane in the buckled energy minimum configuration is 0.8–1.6 Å (ref. 35, 36 and 186) (Fig. 7b).

Table 5 Geometry of SW defect in single-layer graphene: lengths (in Å) of bonds between two heptagons (r_{77}), between a heptagon and a pentagon (r_{57}), between a pentagon and a hexagon (r_{56}) and between a heptagon and a hexagon (r_{76}). The system considered (periodic boundary conditions (PBC) or flake), cell size, number of atoms in the computational cell and calculation method are indicated

Ref.	System	Number of atoms	Method	r_{77}	r_{57}	r_{56}	r_{76}
36	PBC	98	DFT-LDA	1.31			
152	PBC	18	DFT-LDA	1.28	1.50	1.43–1.45	1.43–1.45
186	PBC	242	DFT-PBE	1.32			
164			DFT	1.32	1.46		1.45
			DFTB[121]	1.32	1.45		1.44
166	PBC	50	DFT-PW91	1.28	1.47	1.35, 1.44	1.44
206	PBC		DFTB[121]	1.338	1.466		1.450, 1.459
198	Flake, $C_{42}H_{16}$		DFT-B3LYP/6-31G	1.35			
205	PBC		Tersoff–Brenner[128]	1.38	1.43	1.39	1.43

The analysis of correlation effects in the formation energy of two SW defects has revealed that both repulsion and attraction between two SW defects is possible, depending on their relative position and orientation.[138,201] Attraction valleys correspond to a 'diagonal' location of defects with respect to each other for both aligned[138] and misaligned defects.[201] The most energetically favourable configuration is immediately adjacent but not overlapping.

The formation of SW defects in bilayer graphene with the AB stacking of graphene layers (AB-BLG)[35,54] and with twisted graphene layers (TBLG)[35] was investigated. It was shown that in bilayer graphene, SW defects are also stabilised by out-of-plane buckling, but the magnitude of this distortion is reduced to 0.7 Å compared to 1.2 Å in single-layer graphene (SLG),[35] *i.e.* the presence of the second layer inhibits the distortion. The stabilization energy from buckling is also decreased from 220 meV in SLG to 40 meV in AB-BLG and 60 meV in TBLG.[35] The defect formation energy in TBLG was found to be almost the same as in AB-BLG, while there was only slight variation (by tens of meV) for different positions of the SW defect due to the differences in the interlayer coupling.[35] Compared to in SLG, creation of a SW defect requires an additional 140–180 meV (ref. 35) in TBLG and 180 meV (ref. 35) (230 meV (ref. 54)) in AB-BLG. This difference was mostly attributed to the inefficient energy relaxation by out-of-plane buckling in the presence of the second layer.

Typical DFT values for the activation energy of the SW transformation lie in the range 9–11 eV[70,91,119,164,166,188,193–196] (Table 4 and Fig. 8b). The barriers calculated with semiempirical potentials can be substantially underestimated,[70,71,138,197,200,202] although they are still large enough to reflect that two carbon bonds are broken at the same time in this transformation. The transition state for the SW transformation corresponds to a rotation of the carbon bond by 45–55° (Fig. 8b).[119,138,152,166,194,195,200] As in the final SW defect, compressive stress in the transition state caused by the shortened rotating bond (1.29 Å)[194] and other bonds of the central carbon atoms (1.36 Å)[194] is relieved by out-of-plane buckling[138,194,195,200] with an energy gain of about 0.9 eV,[194] 0.4 eV (ref. 138) or 0.3 eV.[200] Different modes of the transition state (Fig. 9) in which (1) both of the central atoms are displaced in the same direction out of the plane (S_{++}), (2) both are displaced in different directions out of the plane (S_{-+}), (3) only one of the atoms is displaced out of the plane (S_{+}), and

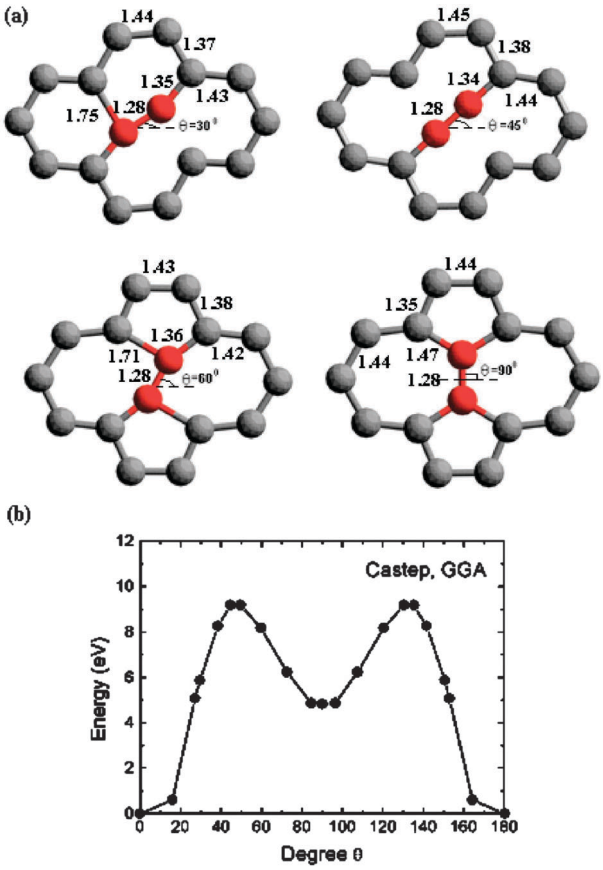

Fig. 8 The Stone–Wales transformation: (a) Intermediate structures corresponding to different angles of bond rotation θ (in degrees) as indicated in the panels. The atoms at the defect core are shown in red. All the bond lengths are in Å. (b) The corresponding formation energy as a function of the rotation angle θ. Reprinted (adapted) from ref. 166. Copyright (2005) by the American Physical Society.

(4) both of the atoms lie in plane (S_0) have been compared. According to the Tersoff–Brenner potential,[128] the reaction path S_{-+} is the most probable, followed by S_{+}, S_{++} and finally S_0.[138,200] However, DFT studies[194,195] predict that the true transition state with only one imaginary frequency corresponds to the S_{+} structure with the central bond tilted by 15°[195] or one of the central atoms buckling out by 0.95 Å.[194] The maximum displacement between atoms perpendicular to the graphene

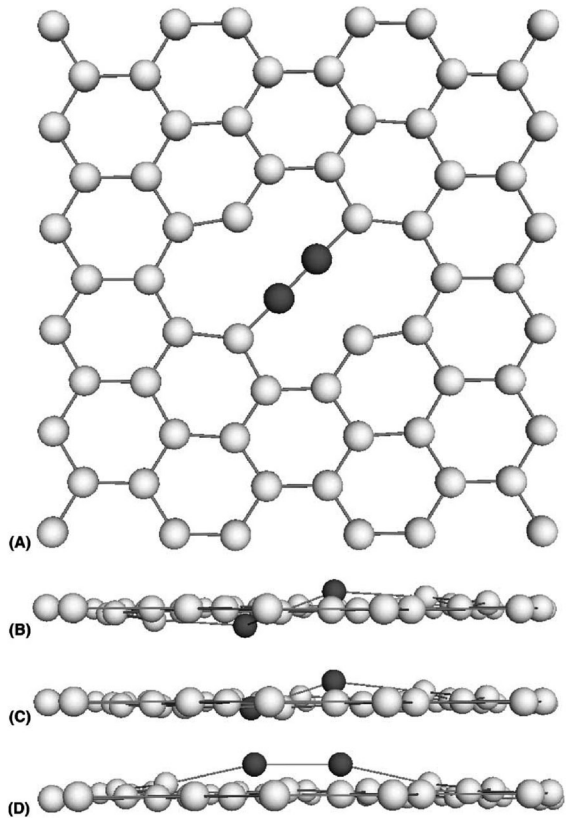

Fig. 9 Atomic configurations for the four modes of the SW transition state. All the modes correspond to bond orientations about 45° (A): (B) S_{-+}, (C) S_{+}, (D) S_{++}. Mode S_0 is not shown and corresponds to all atoms in the plane. Reprinted (adapted) from ref. 138.

plane in the buckled transition state configuration is of the order of that in the final SW defect, at 1.42 Å.[194]

It has been shown that the barrier to the SW transformation can be considerably reduced in the presence of carbon adatoms,[193,196,198] hydrogen and hydroxyl groups[194] or transition metals.[91] Participation of a nickel atom reduces the activation energy of the SW transformation in graphene by 1.8 eV.[91] One hydrogen atom, two hydrogen atoms and two hydroxyl groups reduce the activation energy by 2.5 eV, 5.6 eV and 3.4 eV respectively.[194] The effect of a carbon adatom is even more pronounced as the corresponding mechanism involves only one bond breaking at a time and the activation energy is decreased by 5–7 eV (Table 4).[193,196,198]

3.3.3 Modification of SW energetics by strain. It is seen that the activation energy for a SW transformation is very high, both for the formation of non-hexagonal rings and their annihilation. Therefore, SW defects are unlikely to be formed in pristine graphene even at high temperatures. However, additional manipulations such as electron irradiation or mechanical deformation can induce the formation of SW defects. As the rotated bond of the SW defect is highly compressed, stretching a graphene layer along the direction of the rotated bond leads to a decrease in the formation energy of SW defects[138,188,193,195,199–204,206,211] and activation energy of SW transformations.[31,138,188,193,195,200,202,211] The formation of SW defects can therefore be facilitated by strain, and it has been considered as the first step in the plastic deformation of carbon nanotubes and graphene. The energy gain associated with the rotation of a bond depends on its orientation, and increases with a reduction in the angle of the rotated bond with respect to the loading direction.[31,138,188,195,199–201,206,211] This implies that relieving lateral strain in graphene by SW rotations is most efficient when the layer is stretched along the zigzag direction. The critical strain at which formation of SW defects in graphene becomes thermodynamically favourable was calculated to be 6–9%[188,193,199,202] and 12–17%[188,199] when the strain is applied in the zigzag and armchair directions, respectively. The annihilation of unfavourably oriented SW defects under strain has been demonstrated with MD simulations.[212]

Although both the formation energy of SW defects and activation energy of SW transformations are reduced by several eV at the critical strain, such transformations are still kinetically limited[138,188,193,195,200,202,211] and greater strains should be applied to observe them experimentally. The Arrhenius equation was used to estimate that the yield strain at which the formation of SW defects should take place during experiments at room temperature is on the order of 17–22%[195] for different loading directions in graphene or nanotubes of different chirality, in agreement with the experimentally measured yield strains for carbon nanotubes up to 10%[213] and 17%.[214] The minimum activation energy was reached for an intermediate angle of the rotated bond between 0° and 30° with respect to the loading direction. Calculations[200] on the basis of the Tersoff–Brenner potential[128] predicted that this angle is 11°, while DFT calculations[195] for nanotubes gave an estimate of 22°. The approximate formation energy of SW defects[138,201] and activation energy for SW transformations[195,200] have been proposed as functions of strain magnitude and angle of the rotated bond with respect to the loading direction.

3.3.4 Dislocations. Nucleation of a SW defect "unlocks" carbon nanostructures for further plastic relaxation under strain:[215] (1) plastic flow[138,203,204,211,216,217] and (2) the generation of multiple SW defects[138,203,204] and large rings, such as octagons.[138,216] The first scenario that explains experimentally observed superelongation of carbon nanotubes under strain[18,19] is realised by a separation of pentagon–heptagon (57) pairs[184,218,219,220] (Fig. 10) that represent crystal dislocations[138,190,191,203,204,211,216] (a SW defect is a dislocation dipole in which two edge dislocations with opposite Burgers vectors are displaced by one lattice unit). Separated 57 pairs introduce long-ranged stress fields and consequently high local strain energies. These strain energies can, nevertheless, be partially relieved by the buckling of graphene and formation of protrusions of 2–3 Å (ref. 221 and 222) height near the defects, providing a finite formation energy of isolated 57 pairs of 7.5 eV,[221] 6.2 eV (ref. 203) and 5 eV (ref. 223) according to different calculations.

The glide of 57 pairs, *i.e.* displacement by one Burgers vector at a time, is possible by a SW rotation of the bond between the heptagon and the hexagon adjacent to the pentagon (Fig. 10A, B, D, E). In unstrained graphene,[138,190,191,211,218] separating 57 pairs with one intervening hexagon costs 1–6 eV, although the energy required decreases with further separation of the 57 pairs[211,216,218] (Fig. 11). As with the initial formation of a SW

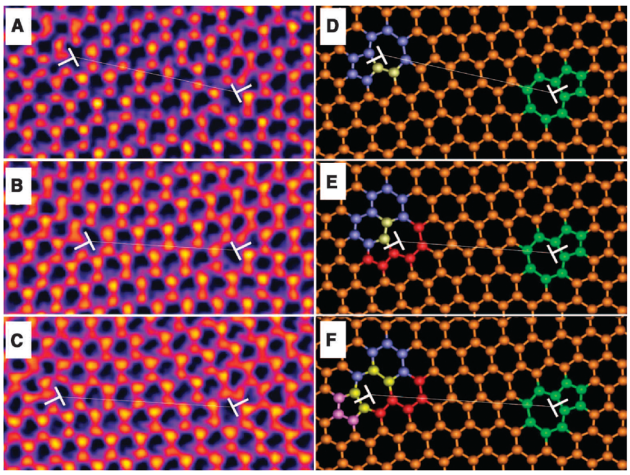

Fig. 10 Real-time dislocation dynamics. HRTEM images showing changes in the position of an edge glide dislocation with time under continuous electron beam irradiation. Time (A) 0 s. (B) 141 s. (C) 321 s. (D to F) Atomic models illustrating the structures inferred from (A) to (C), respectively. The white T indicates the position of the dislocation. The transition from structures (A, D) to (B, E) corresponds to a glide of the dislocation core, while the transition from (B, E) to (C, F) corresponds to a climb step, associated with the emission of a pair of atoms. Reprinted (adapted) from ref. 218 with permission from AAAS.

defect, separation of 57 pairs is stabilised by the application of an appropriate load.[138,203,204,211,216] Therefore, the long range strain fields favour gliding of 57 dislocation cores in opposite directions, while the local curvature energy of two oppositely directed 57 pairs is minimised when they are adjacent and form a SW defect.[138,190,191,203,204,211,216,218] The glide of 57 pairs can also be facilitated by the formation of chains of dislocation dipoles (so-called ''dislocation worms''), which effectively screen stress fields of the separated 57 pairs.[203,204]

In addition to the glide of dislocation cores by SW rotations, another type of motion, a climb step, is possible. Emission of a pair of carbon atoms from the edge between the pentagon and the hexagon adjacent to the heptagon[217] (Fig. 10B, C, E, F) results in motion along the defect axis in the direction from the heptagon to the pentagon. This was shown to be responsible for nanotube sublimation that preserves perfect hexagonal structure even upon significant loss of mass.[224] A combination of the two mechanisms, glide and climb, explains the motion of 57 pairs along any arbitrary trajectory.[217] A combined motion of 57 pairs in graphene by both glide and climb[218,225] (Fig. 10) as well as by glide, assisted by the formation of ''dislocation worms'',[225] was demonstrated for graphene experimentally and is in agreement with HRTEM observations[219,226] for carbon nanotubes.

Unlike in nanotubes, in graphene the formation of a second SW defect is preferable to the dissociation of the first SW defect into 57 pairs, both under strain and in its absence.[138,203,204] Simple dissociation of SW defects into 57 pairs in graphene is therefore thermodynamically unfavourable, and in most cases the plastic deformation of a graphene layer should start through the formation of additional defects, multiple SW defects or larger rings such as octagons. Once the defects are present in graphene, subsequent SW rotations become much easier. For example, the activation energy of the transformation of the V_2(5-8-5) structure to V_2(555-777) was found to be 5.74 eV, according to the TB calculation[173] (5.17 eV according to LDA calculation), which is almost half the 10.2 eV activation energy for the formation of a SW defect in perfect graphene, obtained in the same paper. It is important to note, however, that plastic deformation through the creation of multiple defects can also finally lead to the formation of isolated 57 pairs. For instance, chains of SW defects are known to rearrange giving 57 pairs screened by ''dislocation worms''.[203,204]

Deformation of graphene under strain, nevertheless, is hardly the main source of lone separated 57 pairs so frequently observed in HRTEM.[218,227,228] Creation of dislocations under HRTEM conditions can be explained by the reconstruction of vacancies and adatoms introduced by electron irradiation.

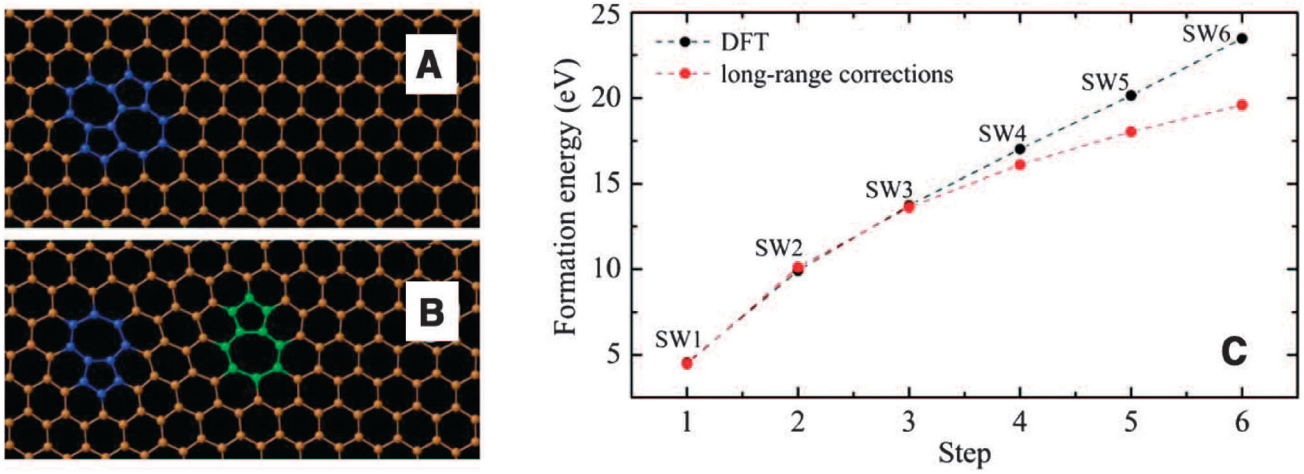

Fig. 11 (A and B) Atomistic models obtained within DFT for one and four Stone–Wales bond rotations (steps 1 and 4). (C) Formation energy at each step (one dislocation is stationary and the other one is moving along the glide direction). The black dots represent the DFT data. The red dots represent the DFT data corrected for long-range strain-field interactions. Reprinted (adapted) from ref. 218 with permission from AAAS.

Tight-binding molecular dynamics simulations for carbon nanotubes with multi-vacancies demonstrate that such nanotubes are sewed up almost perfectly with only two separated 57 pairs left and a reduced diameter.[92,93] The transformation of graphene with a chain of missing atoms to a nearly ideal layer with only two separated 57 pairs was shown to be preferred over the formation of a local haeckelite structure composed of collective 555-777 defects when the multivacancy size exceeds ten,[176] in agreement with the experimental data.[225] The formation of separated 57 pairs was found to be favourable over other possible reconstructions for multivacancy sizes above 4 in narrow graphene nanoribbons of width within 1 nm, and above 26 in wide graphene nanoribbons of width greater than 10 nm.[175]

According to the experimental data,[225,228] however, even scattered vacancies tend to reconstruct and form a nearly ideal hexagonal network with only two separated 57 pairs. Divacancies can dissociate into 57 pairs by glide and pseudoclimb similar to SW defects.[217,227] However, 57 pairs formed in this way turn out to be unstable, as seen in tight-binding molecular dynamics simulations.[228] Stable dislocations are rather produced by agglomeration and collective reconstruction of several vacancies assisted by carbon adatoms helping to convert non-hexagonal rings into hexagons, as follows both from computer simulations[228,229] and experimental observations.[228]

The geometry of stable dislocations depends critically on whether they are formed from adatoms or vacancies.[225,228] The dislocation cores formed from adatoms (*i.e.* pointing towards each other) have only shallow minima at nanometre distances associated with the antisymmetric hillock–basin configuration, while at short distances they prefer the symmetric hillock–hillock configuration and tend to migrate towards one another by SW rotations.[225] The dislocation cores formed by multi-vacancy reconstruction, on the other hand, repel at short distances and have only one minimum at the distance determined by the number of vacancy units, in which the antisymmetric hillock–basin configuration is slightly preferred over the symmetric hillock–hillock one.[228]

In addition to 57 pairs, double pentagon (octagon) rings have been recently identified as dislocation cores in graphene.[230] As with separated 57 pairs, these defects are formed by the reconstruction of vacancy constellations and move by glides involving one bond rotation at each step.[230]

3.3.5 Graphene grain boundaries. The non-hexagonal rings in polycrystalline graphene play an important structural role as grain boundaries[20,231–236] between arbitrarily oriented graphene flakes. Dislocations characterised by any Burgers vector as well as grain boundaries, covering the whole range of possible misorientation angles, can be constructed on the basis of coupled ((1,0) dislocation) and dissociated ((1,1) dislocation) 57 pairs separated by hexagons[221–223,237] (Fig. 12). The stress fields of isolated dislocation cores in the limit of misorientation angles $\theta \rightarrow 0^\circ$ and $\theta \rightarrow 60^\circ$, which correspond to small-angle armchair and zigzag regimes, respectively, induce strong buckling of graphene with protrusion heights on the order of 2–3 Å.[221,222] The possibility of such buckling in free-standing graphene results in a considerable reduction of the grain boundary energy.[203,204,221,238,239] These theoretical results are supported by experimental STM images

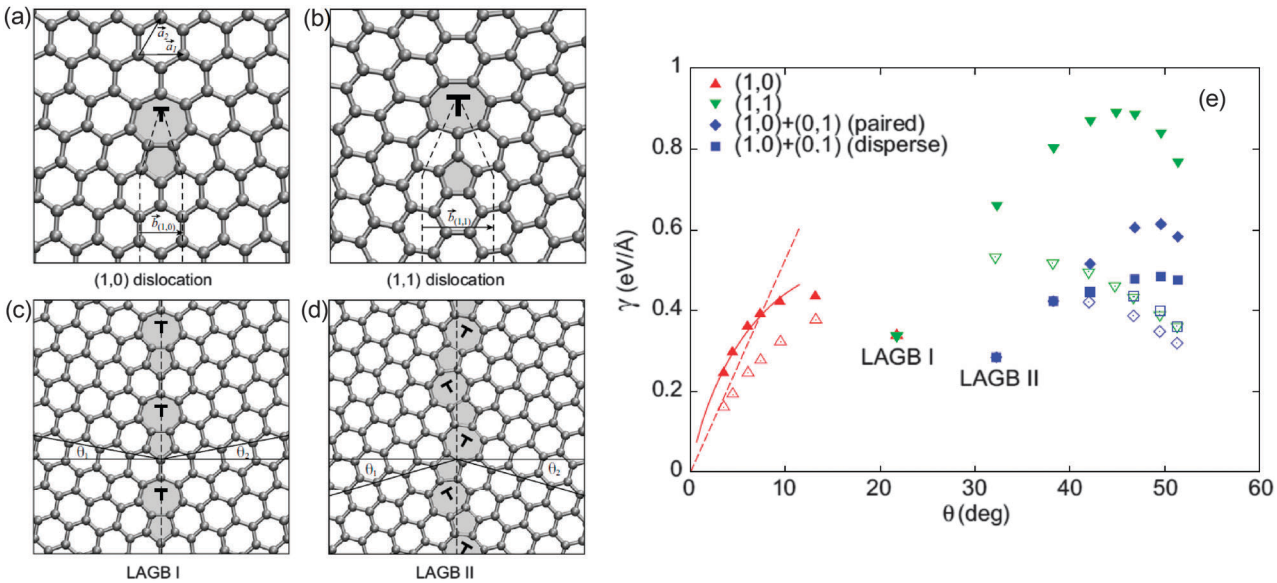

Fig. 12 (a, b) Atomic structures of (1,0) and (1,1) dislocations. The dashed lines delimit the semi-infinite strips of graphene introduced at the dislocation core. Non-hexagonal rings are shaded. (c, d) Atomic structures of the θ = 21.8° (LAGB I) and the θ = 32.2° (LAGB II) symmetric large-angle grain boundaries, respectively. The dashed lines show the boundary lines and the solid lines definite angles θ_1 and θ_2 ($\theta = \theta_1 + \theta_2$) defining orientations of the graphene grains. (e) Grain-boundary energy per unit length γ as a function of misorientation angle θ for various flat (filled symbols) and buckled (open symbols) grain-boundary structures. The two energetically favorable large-angle grain boundaries, LAGB I and LAGB II, are labeled. The dashed curve shows the asymptotic linear dependence of γ for the buckled small-angle armchair grain boundaries (E_f = 7.5 eV). Reprinted figures with permission from ref. 221. Copyright (2010) by the American Physical Society.

of graphene on Ir[232] and SiC,[233] where hillocks with large separations are observed at small-angle grain boundaries. Buckling is also predicted to take place in disordered grain boundaries.[240]

The energies of the most favourable straight grain boundaries covering all angle ranges lie within 0.5 eV Å^{-1} (Fig. 12e),[221–223,238,239,241] *i.e.* they are smaller than typical values for bare graphene edges (1.0–1.2 eV Å^{-1}).[96,164,242–248] Especially stable large-angle grain boundaries are formed by close packing of (1,0) (LAGBI) and (1,1) (LAGBII) dislocation cores (Fig. 12c–e).[221] These grain-boundaries with misorientation angles 21.8° and 32.2° have formation energies of only 0.338 eV Å^{-1} and 0.284 eV Å^{-1}, respectively.[221] Though they contain the maximum number of dislocation cores, their stress fields mutually cancel each other providing the lowest formation energy and maximum mechanical strength.[208,221,249,250] Unlike in small-angle grain boundaries, these structures are flat,[220,221] as confirmed by the experimental data.[233] The formation energy of LAGBII per 57 pair is almost half that of SW defects (1.3 eV *vs.* 2.5 eV according to ref. 251), leading to its abundance in experimental observations[233–236] and realisation of grain boundaries at other large angles as pieces of LAGB II separated by kinked sites.[235] Similar results were obtained for rotational grain boundaries, where the structure formed by a loop of six alternating pentagons and heptagons (the flower defect) was identified as the topological defect with the lowest formation energy per dislocation core (1.2 eV),[251] explaining why its formation is frequently observed *via* coalescence of mobile dislocations or SW defects.[20,225]

The glide and climb of 57 pairs constituting grain boundaries[222,252] make their migration possible.[20] The driving force for this migration depends only on the local in-plane boundary curvature and does not depend on the atomistic structure, providing that curved grain boundaries tend to become straight, while grain boundary loops annihilate upon annealing.[20] Tight-binding molecular dynamics simulations[252] of grain boundary motion showed that C_2 dimer emission, corresponding to a climb of the 57 pairs, is preceded by the formation of an adatom.

3.3.6 Effects of edges on the formation of SW defects. The close vicinity of graphene edges allows for a more efficient relaxation of SW defects, providing a decrease in both the formation energy of SW defects and the activation energy for this process.[70,71] The formation energy of SW defects was shown to reduce from 4.4 eV inside a large graphene flake to 2.3 eV at the zigzag flake edge[70,71] according to the Tersoff–Brenner potential[128] and from 5.2 eV to 3.1 eV according to DFT calculations.[70] The corresponding changes in the activation energy were from 7.9 eV to 6.7 eV according to the semiempirical potential[70,71] and from 9.9 eV to 6.8 eV according to DFT calculations.[70] The formation energy and barrier for SW defects at the armchair edge of the flake were calculated to be 2.8 eV and 7.4 eV, respectively.[71]

3.3.7 Edge reconstructions. In addition to the effect on the energetics of reactions inside graphene layers, edges enable new reactions with the participation of under-coordinated atoms at the very edge. As these atoms are already destabilised compared to ones in the graphene interior, the corresponding reactions have considerably reduced barriers and reaction energies[70,71] This means that such processes can occur at experimentally accessible times at high temperatures even without the assistance of catalysts, strain or irradiation, as opposed to SW transformations inside the layers.

In particular, reconstruction of the zigzag (ZZ) edge *via* the transformation of pairs of adjacent hexagons to pentagon–heptagon pairs (Fig. 13a) is energetically favourable[77,96,148,164,242–248,253] and is often observed experimentally.[13,75,254,255] This reconstruction (ZZ(57)) decreases the zigzag edge energy by 0.1–0.4 eV Å^{-1}, making it even slightly more stable than the armchair (AC) edge (Table 6). These results can be understood by considering edge geometries. The pristine zigzag edge is known to be much more expensive energetically than the armchair one, as two-coordinated atoms at the zigzag edge have dangling bonds,

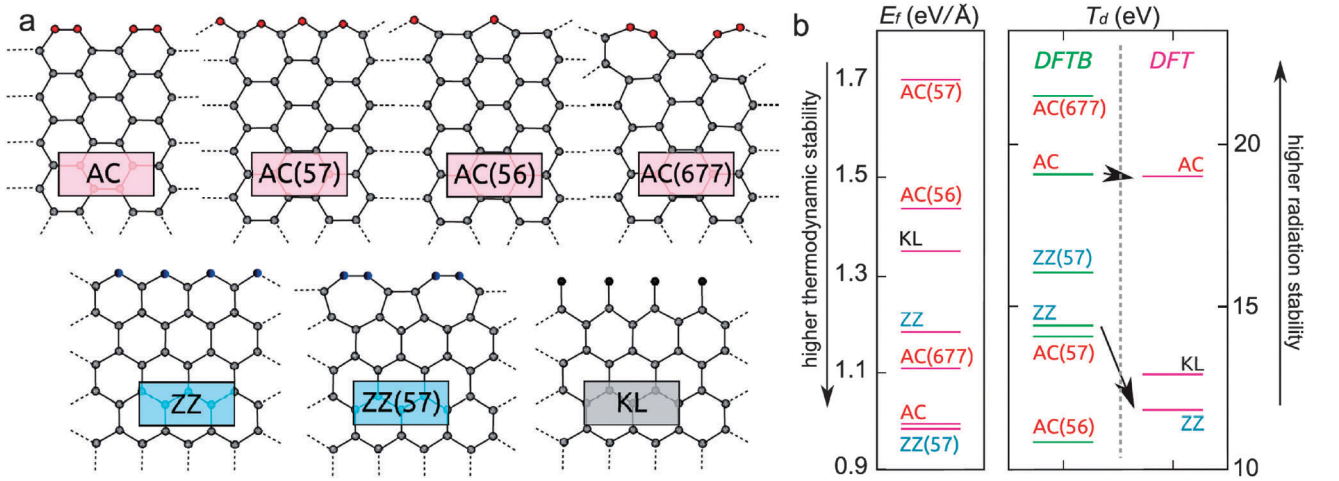

Fig. 13 (a) Different edge reconstructions as optimised by DFT and (b) their formation energies E_f and displacement thresholds T_d. Displacement thresholds as calculated with both DFT and DFTB are presented, showing the disagreement between DFT and DFTB for ZZ edges. Uncertainties in the T_d are of the order of 0.1 eV. Reprinted (adapted) with permission from ref. 148. Copyright (2014) American Chemical Society.

Table 6 Energies (in eV Å^{-1}) of pristine zigzag (ZZ), pristine armchair (AC), reconstructed zigzag (ZZ(57)) and reconstructed armchair (AC(677)) edges of graphene. The calculation method (SP and NSP stand for "spin-polarised" and "non-spin-polarised" calculations, respectively) is indicated

Ref.	Method	ZZ(57)	AC	AC(677)	ZZ
96	DFT-LDA	1.06	1.09		1.43
	TB model[124]	1.10	1.12		1.41
164	DFTB[121]	1.07	1.08		1.21
242	DFT-LDA, SP	1.09	1.10		1.34
243	DFT-PBE	0.96	0.98	1.11	1.31
244	DFT-PW91, SP	0.97			1.21
245	DFT-PBE/DZP, SP	0.98	1.02		1.15
	DFT-PBE/DZP, NSP	0.98	1.02		1.34
	Modified LCBOPII[245]	0.81	0.75		1.05
246	DFT-PBE, SP	0.965	1.008		1.145
247	DFT, SP	0.97	1.00	1.08	1.17
248	DFT-LDA/DZP, NSP	1.147	1.202		1.543
	DFT-LDA/DZP, SP	1.147	1.202		1.391

while two-coordinated atoms at the armchair edge form triple bonds, as seen by short bond lengths between such atoms (1.22–1.25 Å,[164,242,243,245] close to the 1.20 Å triple bond in acetylene (Table 7)). The same triple bonds of 1.23–1.26 Å length[78,164,242,243,245,247,253] are observed between two-coordinated atoms in the reconstructed ZZ(57) zigzag edge, guaranteeing its stability (Table 7). The initial compressive stress of the pristine zigzag edge of −0.5 eV Å^{-1},[247] −2.05 eV Å^{-1},[76] and −2.09 eV Å^{-1} [248] is completely reversed to a tensile stress of 1.5 eV Å^{-1},[247] 0.24 eV Å^{-1},[76] and 0.14 eV Å^{-1} [248] in the reconstructed ZZ(57) edge that provides its planarity. The 100% reconstructed edge also becomes non-spin-polarised.[73,247,248]

Reconstruction of the armchair edge through the transformation of three adjacent hexagons to two heptagons and a pentagon (an incomplete SW defect, Fig. 13a, AC(677)) was shown to be energetically unfavourable although still preferred over the unreconstructed zigzag edge (Table 6).[243,247] Nevertheless, it was also predicted that partial reconstruction of the armchair edge can further stabilise it.[247] The minimum edge energy of 0.98 eV Å^{-1}, very close to the edge energy of the reconstructed ZZ(57) zigzag edge, was calculated for about 25% of hexagons transformed into 6757 fragments.[247] Such a structure was also shown to have a small edge stress, indicating that it is stable against deformations, while the fully reconstructed armchair edge has a considerable tensile stress of 4 eV Å^{-1}.[247]

It should be emphasised, however, that these considerations are only valid at very low hydrogen pressures, while at ambient conditions the edges are passivated and no dangling bonds are left.[246] In this case, reconstruction of the edges has a considerable energy cost, while the edges consisting only of hexagons and with two-coordinated atoms bonded to hydrogen are the most preferred.[192,246,253,256] The energetics and warping of various hydrogen-passivated reconstructed edges was analysed.[192,246,256] The reconstruction of the zigzag edge into a sequence of alternating pentagons and heptagons is also unfavourable on transition metal surfaces, while other new types of reconstructions with an increased number of low-coordinated carbon atoms become possible.[257] Decoration of graphene edges with silicon[258] and other adatoms[259] is also known to affect their structure.

The activation energy for simultaneous and complete reconstruction of the zigzag edge is proportional to the edge length, and was calculated to be 0.6 eV per hexagon pair.[243] The simulations using a semiempirical potential[245] gave a rather close value of 0.7 eV at the low temperature limit.[245] Though it was shown to have non-monotonic behaviour at high temperatures (increasing up until 700 K and slowly decreasing at higher temperatures[245]), the cost for this simultaneous transformation remains too high and the transformation actually occurs step-by-step *via* the formation of pentagon–heptagon pairs. Therefore, sequential steps of the process have to be analysed.

3.3.8 Bond rotation reactions at graphene edges. The formation energy of a 57 pair at the zigzag edge of a 12-atom square hole in graphene was found to be 1.35 eV by first-principles calculations, much smaller than 3.83 eV for the SW transformation inside the layer.[187] The formation energy of a 57 pair at the pristine zigzag edge of a graphene flake was found to be about 1 eV according to the semiempirical potential,[128] 3.4 eV smaller than for a SW defect inside the graphene flake.[70,71] The activation energy of this reaction was found to be around 3 eV, which is less than half that of the SW transformation inside the layer.[70,71] Such a decrease was explained by the fact that bond switching at the edge requires only one bond to be broken at a time, compared to two in the perfect graphene layer.

A consecutive energy decrease by 1.51 eV and 1.78 eV was observed in successive steps of the generation of 57 pairs[96] according to TB and unpolarised LDA calculations, which are known to underestimate the stability of the pristine

Table 7 Geometry of graphene edges: lengths (in Å) of triple (central) edge bonds of heptagons (r_{7c}), other edge bonds of heptagons (r_7), edge bonds of pentagons (r_5), between heptagons and pentagons (r_{57}), between heptagons and hexagons (r_{76}), between pentagons and hexagons (r_{56}) in the reconstructed zigzag edge, edge bonds in the pristine zigzag edge (r_z), triple (central) edge bonds of hexagons (r_{a1}) and other edge bonds (r_{a2}) of the pristine armchair edge. The calculation method is indicated

Ref.	Method	r_{7c}	r_7	r_5	r_{57}	r_{76}	r_{56}	r_z	r_{a1}	r_{a2}
78	DFT-LDA	1.24	1.39	1.43	1.45	1.43	1.40			
164	DFTB[121]	1.24	1.43	1.43				1.40	1.25	1.42
242	DFT-LDA	1.24	1.38	1.45				1.42	1.22	1.38
243	DFT-PBE	1.24	1.41	1.44	1.47			1.39	1.24	1.39
247	DFT	1.23								
248	DFT-LDA/DZP							1.40	1.26	
253	DFT-PBE/DZP	1.26								
245	Modified LCBOPII[245]	1.28	1.41	1.41	1.47			1.40	1.28	1.40

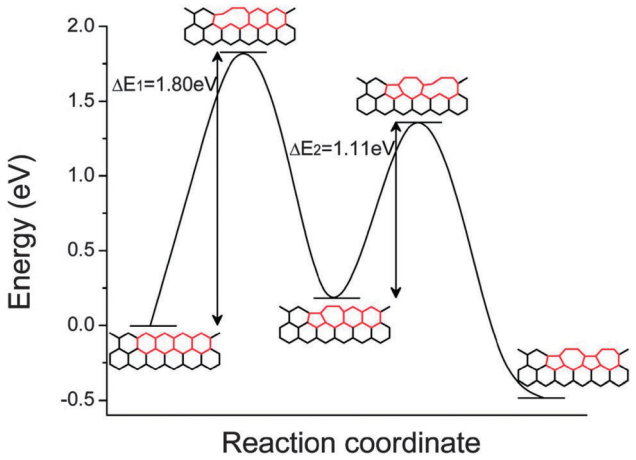

Fig. 14 The minimum energy path of the first and second step transitions from a hexagon–hexagon pair to a pentagon–heptagon pair. Reprinted (adapted) from ref. 77.

zigzag edge.[77,245,247,248] Activation energies of just 0.69 eV and 0.44 eV for each respective step were obtained, indicating that such a transformation should take place spontaneously at room temperature.[96] A similar free energy barrier of 0.83 eV was obtained at room temperature using a semiempirical potential.[245] The barrier was shown to increase up to 1 eV with increasing temperature.[245] Recent spin-polarised DFT calculations have, however, refined these values. The energy increase by about 0.3 eV was found for the formation of the first 57 pair, followed by a total energy gain of 0.6 eV from the generation of the second one[77] (Fig. 14). An activation energy of 1.80 eV (ref. 77) or 1.12 eV (ref. 73) was obtained for the first step, and 1.11 eV for the second one[77] (Fig. 14), demonstrating that the pristine zigzag edge is stable at room temperature, as confirmed by experiments.[72,74,260] An energy decrease of 0.21 eV was predicted for the formation of the first 57 pair in ref. 79 and the activation energy for this reaction was found to be 1.61 eV. It was also suggested that the formation of these pairs can occur through the recombination of an adatom and a vacancy, with an activation energy of just 0.89 eV.[79] The barriers for the migration of an adatom and vacancy on the zigzag edge were calculated in the same paper to be 0.76 eV and 2.12 eV, respectively.

Tensile stress was shown to increase energies of the pristine and defected zigzag edges, decreasing the activation energy for the first-step transformation with 0.21 eV per % rate.[73] Therefore, a uniaxial strain of 5% is sufficient to provoke reconstruction of the zigzag edge at room temperature.[73,77] Fracture of a monolayer graphene was shown to be governed by the competition between bond breaking and bond rotation at a crack tip.[261] Using atomistic reaction pathway calculations, a kinetically favourable fracture path was identified as an alternating sequence of bond rotation at the graphene edge and bond breaking.[261] The generation of 57 defects was also shown to play a crucial role in graphene evaporation, as the emission of carbon atoms was found to proceed preferentially from heptagons.[96] In particular, the energy gain from the formation of several 57 pairs at the zigzag edge was revealed to be sufficient to compensate for atom evaporation.[96]

Similar energetics are observed for other defects and graphene edges. The formation of a 757 fragment on the armchair edge of a hole in graphene was calculated to be 2.01 eV, which is significantly reduced as compared to the formation energy of a SW defect.[187] The energetics of various defects at zigzag and armchair edges of graphene flakes were investigated.[70,71] Similar barriers on the order of 3 eV were obtained for all reactions proceeding through the breaking of only one bond, including diffusion of pentagons and heptagons along the edges. Reactions forming carbon chains by breaking a bond between adjacent rings were recognised as important for all types of edges at high temperatures. Though the potential energy change in such reactions is relatively high, on the order of 2 eV, the formation of carbon chains becomes favourable at high temperatures due to an increase in entropy, related to their low-frequency vibrations.[70,71] The formation of carbon chains and their reconnection followed by edge reconstruction was shown to be the principal mechanism of transformation of a graphene flake to a fullerene[70,71,87] and formation of nanotube caps from open nanotube ends.[88] The transformation of narrow graphene nanoribbons into carbon chains was observed experimentally under electron irradiation.[13,14] The formation of carbon chains also took place in simulations of strained graphene nanoribbons at high temperature.[262,263]

4. Reactions under irradiation

While the important values when discussing thermally activated reactions are the activation and formation energies, threshold energies are key for irradiation-induced reactions. The threshold energy of a process is the minimum energy required for that process to occur without immediate reversal, considering a specific direction of atom motion induced by the electron beam. The difference between the activation energy and threshold energy for the same reaction can be explained as follows. Firstly, as the reaction pathway for an irradiation-induced reaction is determined by the direction of momentum transferred to a given atom from the incident electron, it does not necessarily coincide with the optimal reaction way for the thermally activated reaction. Secondly, even for optimal directions of transferred momentum (at the minimum threshold energy), the collective motion of multiple atoms will usually not coincide with the optimal reaction way for thermally activated reactions. The threshold energy of an irradiation-induced process therefore tends to be higher than the activation energy of the equivalent thermally induced process.

Under the electron beam, graphene is constantly exposed to an external stimulus. In these non-equilibrium conditions, low formation energies do not therefore imply the structures most likely to form and survive. In fact, the presence of possible routes induced by the beam towards a structure and the subsequent stability of the structure against the electron irradiation are key. The preferred configuration of graphene edges in TEM is a good example of the importance of these considerations. Two main edge configurations are observed: zigzag (ZZ) and armchair (AC). Although early observations and calculations[260] concluded that the ZZ configuration would be the most stable, the consideration

of dynamic effects following electron impacts demonstrated the very high stability of AC edges with respect to irradiation.[148]

For another demonstration of this effect consider the structure of the most commonly observed tetravacancy, the extended linear structure.[264] It was proposed that the high occurrence of the most common V_4 structures in TEM images is due to the specifics of the irradiation-induced pathways towards their creation, but an explanation for the long lifetime of the linear structure over the more frequently modelled structures is perhaps due to the shared structural features between this vacancy and the V_2(5555-6-7777) divacancy (or 'butterfly' vacancy). It has been shown that the central atoms of this divacancy have an even larger emission threshold than pristine graphene,[147] implying a very strong stability against electron irradiation. It would therefore be expected that this is also true of the very similar tetravacancy structure.

4.1 Atom emission

4.1.1 From pristine graphene. The emission of carbon atoms from pristine graphene in TEM has been extensively studied, both theoretically and experimentally. It has been observed that in order to eliminate atom emission and the creation of holes and defects, an accelerating voltage of 80 kV or lower must be used. This corresponds to a maximum transmittable energy to a stationary carbon atom of 15.8 eV, implying that the emission threshold energy of carbon must be slightly above this. However, Meyer *et al.*[146,267] demonstrated the importance of including the effects of the thermal motions of the graphene lattice when considering the transfer of momentum from beam electron to sample atom, explaining the apparent overestimation of theoretical emission thresholds compared to experiment. This inconsistency had previously been attributed to the absence of any beam-induced electronic excitations in calculations,[150,265] but was revealed to be an effect of the increased transmittable energy from the beam due to thermal motion of the atoms; the threshold energies are generally accurate when taking this into consideration (Table 8). An experimentally derived rate of atom emission from graphene was found at various accelerating voltages and dose rates, and used to calculate the threshold energy of 23.6 eV including these lattice vibration effects.[146,267] It is worth noting that this is higher than any published theoretical value, by at least 0.6 eV. A comparison[266] of theoretical threshold energies calculated by DFT to excited state time-dependent DFT (TDDFT) calculations that explicitly included the electron dynamics concluded that the ground state Born–Oppenheimer dynamics universally used when calculating threshold energies is indeed justified. Qualitative trends were very similar between DFT and TDDFT, despite small quantitative differences; DFT resulted in the transfer of slightly more energy to the surrounding graphene lattice, while TDDFT showed similar kinetic behaviour of the emitted atom and the graphene lattice at a delay of 10 fs.

Although areas of pristine graphene are generally considered to be protected from irradiation damage at or below 80 kV, the use of very high electron dose rates ($>10^8$ e nm^{-2} s^{-1}) at 80 kV has been shown to create defects.[65] Similar defect creation is not witnessed under lower dose rates ($<10^6$ e nm^{-2} s^{-1}) and long irradiation times, where large total numbers of electrons are passed through the sample ($\sim 10^{10}$ e nm^{-2}),[146,267] meaning that a dose-rate dependent effect is either lowering the threshold energy or increasing the energy that can be transferred by increasing the out-of-plane atomic vibrations. This lowered threshold energy is calculated to be 19.7 eV, and weakening of the bonds due to ionization or plasmon excitations was suggested as a possible cause. Alternatively, while beam-induced heating effects were shown to be not responsible, a flexural phonon mode induced by inelastic collisions could result in the required increase in out-of-plane vibrations. This electron

Table 8 Threshold energies E_d (in eV) calculated for various processes in graphene. The system considered (periodic boundary conditions (PBC), flake or nanoribbon), number of atoms in the computational cell and calculation method are indicated

Process	Ref.	System	Size of supercell	Method	E_d (eV)
Emission from pristine graphene	146,267	Experimental measurement	—	—	23.6
	268			DFTB	22
	265	PBC	7 × 7 supercell	DFTB	23
	150	PBC	4 × 6 supercell	DFT-PBE	22.03
	147		120–200 atoms	DFTB	22.50
	266	PBC	478 atoms (converged to 1342)	DFT-LDA	23
	151	Graphene flake		DFTB	23.0
	225 (ESI)	PBC	152 atoms	DFTB	21.34
	269	PBC	160 atoms	DFT-PW91, SP	22
Emission from V_1(5-9)	148	PBC		DFT-PBE	14.7
Emission from V_2(5-8-5)	148	PBC		DFT-PBE	16.2
Emission from pentagon site	151	Graphene flake		DFTB	16.9
Emission from 2-coordinated edge	151	Graphene flake		DFTB	13.4
Emission from AC edge	148	Graphene nanoribbon, PBC	6–7 graphene unit cells wide	DFT-PBE	19.0
Emission from ZZ edge	148	Graphene nanoribbon, PBC	6–7 graphene unit cells wide	DFT-PBE	12.0
Emission from KL edge	148	Graphene nanoribbon, PBC	6–7 graphene unit cells wide	DFT-PBE	12.9
SW formation	266	PBC	478 atoms (converged to 1342)	DFT-LDA	19
	271	PBC	72 atoms	DFT-LDA/DZP	22.5
	271	PBC graphene with h-BN substrate	144 atoms	DFT-LDA/DZP	31
SW healing	266	PBC	478 atoms (converged to 1342)	DFT-LDA	13
	271	PBC	72 atoms	DFT-LDA/DZP	14
	271	PBC graphene with h-BN substrate	144 atoms	DFT-LDA/DZP	17

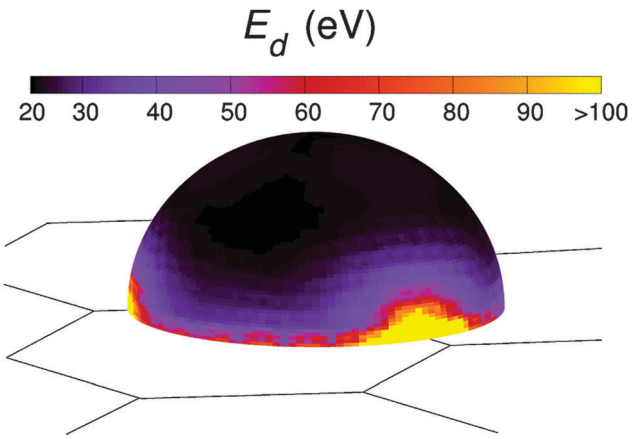

Fig. 15 Mapping of the threshold energy for emission of an atom from pristine graphene as a function of the angle of transferred momentum from the e-beam. The threshold energy of 23 eV rises very rapidly to large energies at angles parallel to the graphene sheet. Reprinted figure with permission from ref. 265. Copyright (2007) by the American Physical Society.

dose rate dependent effect has been exploited with the ability to create defects at a high dose rate and then observe their dynamics without creating additional defects at a lower dose rate, all at an 80 kV accelerating voltage.[65,159,264]

The threshold energies given for atom emission only correspond to the case when the transmission of energy from beam electron to graphene atom occurs perfectly perpendicular to the graphene plane. This is the angle at which a minimum energy will be required to emit the atom, while more energy will be needed if transferred at a shallower angle. When energy is transferred at non-perpendicular angles, there will also be a variation in threshold energy with the azimuthal angle φ; the in-plane direction of energy transfer. In the typical setup of the electron beam being perpendicular to the graphene sheet, this minimum threshold energy coincides with the angle at which most energy can be transferred ($\theta = \pi$, where θ is the electron scattering angle). This means that for emission processes, the single value of the threshold energy is highly informative, despite the anisotropic dependence of threshold energy on angles of momentum transfer. For other processes, such as the SW rearrangement discussed later, this overlap of the minimum threshold energy E_d with the angle at which the maximum energy can be transferred from the beam does not hold, and so mapping of the anisotropy is vital. Mapping of the anisotropy of the threshold energy of emission from pristine graphene, shown in Fig. 15,[265] confirmed the very sharp increase in E_d at $\theta < \pi$, rising from 23 eV to 43–780 eV at $\theta = \frac{\pi}{2}$, depending on φ.

4.1.2 From vacancy structures. Following the emission of a single atom from pristine graphene, a symmetrical vacancy or reconstructed 5-9 structure is formed. In any structure with an odd number of missing atoms, there will always be at least one under-coordinated atom bonded to fewer than three atoms. These atoms will be more easily lost *via* collisions with electrons from the e-beam due to a decreased emission threshold, calculated as 12 eV for the unreconstructed vacancy[266] and 14.7 eV in the case of the reconstructed monovacancy.[148] As this energy is easily accessible to even an 80 kV electron beam, correlated sputtering of two atoms from areas of pristine graphene is normally observed. Even-numbered vacancies are fully coordinated with three bonds to each atom and subsequently have larger threshold energies, although the value varies depending on the ring size and to a smaller extent on the specific local structure. For example, atoms in pentagons typically have threshold energies around 16.9 eV,[151] depending on the local atomic structure. This generally leads to the formation of separate divacancies on the graphene lattice, as once a divacancy is formed there is a much smaller preference as to which atom will be emitted next, and the typically low concentration of defect sites means that additional emissions are likely to occur on pristine graphene.

This effect is increased with the existence of the two commonly observed reconstructed divacancy structures shown in Fig. 3. As the central atoms of these structures have been shown to have a larger emission threshold than pristine graphene,[147] the probability of direct trivacancy formation is further reduced.

In dislocation dipoles, the emission of two atoms leads to a climb step, increasing the distance between the two dislocations (shown in Fig. 10).[218] Emission of atoms from the area surrounding the dislocation has been observed to occur more frequently than in pristine graphene, confirmed by calculations of the threshold energies for all surrounding atoms.[225] The threshold energies ranged from 18.64 to 24.14 eV, compared to 21.34 eV calculated for emission from pristine graphene using the same method. This study also demonstrated the importance of the beam direction in defects which introduce out-of-plane topology. As the buckled structure of the dislocation is not flat, there are two distinct directions in which it can be oriented with respect to the beam, up or down. Depending on the direction of the e-beam in the *z*-axis, the emission threshold energy of an individual atom varied by up to 2.9 eV (Fig. 16).

4.1.3 From graphene edges. A study of the emission threshold energies of various simple and reconstructed edge configurations used graphene nanoribbons of various widths.[148] DFTB calculations were undertaken for all edge configurations shown in Fig. 13. Termination of various edge configurations by hydrogen atoms was shown to have no effect on the emission threshold energies of edge atoms. The threshold energies calculated by this method are shown, ranging from $\sim$11 eV for the AC(56) edge to $\sim$22 eV for the AC(677) edge. Also shown are the results of more computationally demanding DFT simulations, carried out for the unreconstructed AC (19.0 eV), ZZ (12.0 eV) and KL (12.9 eV) edges. This set of calculations showed that the specific local structure of edges has a very large impact on the irradiation stability, and demonstrated the lack of correlation between irradiation stability and low formation energy; the AC and KL edges exhibit very flexible behaviour following impacts from the electron beam, which increases their resistance to atom emission. The discrepancy between these predictions of the stability of AC configurations over ZZ, compared to experimental observations of preferential ZZ formation in holes in graphene,[260] was attributed to the differences between an approximately circular hole and extended edges.

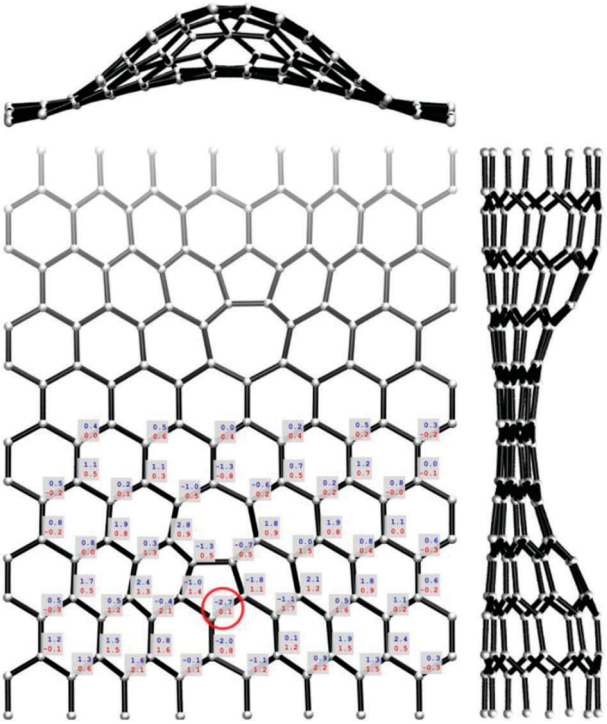

Fig. 16 Emission threshold energies calculated for atoms surrounding a dislocation core. Values are given as deviations from the pristine value calculated using the same method (21.34 eV). As the structure is buckled out-of-plane (side views), it is not symmetrical, resulting in different threshold energies when the momentum is transferred upwards (blue numbers) and downwards (red numbers). Reprinted (adapted) from ref. 225 (ESI).

The predicted stability of the KL edge under the e-beam was very recently confirmed by experimental HRTEM images showing their existence in graphene nanoribbons and at the edge of bulk graphene.[270]

4.2 Bond rotations

4.2.1 In pristine graphene. Other than emission, the only major process of irradiation-induced atomic structure change in graphene is the Stone–Wales (SW) rearrangement, a 90° rotation of a single carbon–carbon bond. In pristine graphene a SW rearrangement leads to a SW defect, composed of two 5- and two 7-membered rings. This has been observed in TEM and is seen to heal quickly, on the order of the electron dose per image used ($\sim 10^7$ e nm^{-2}).[147] Theoretical calculations confirmed the creation of the SW defect *via* impacts with electrons from the e-beam, revealing two mechanisms of formation. The energy required for SW defect formation was calculated as being typically 1 eV lower than the emission threshold (calculated as 22.5 eV), with 2 eV below this resulting in SW formation at certain space angles of transferred momentum.

The threshold energies for the formation and healing of a SW defect were calculated as being 22.5 eV and 14 eV respectively, confirming the reversible nature of the defect.[271] The same study revealed the ability of substrates to alter the energy required for each process; placing the graphene on hexagonal boron-nitride increased them to 31 eV and 17 eV respectively. An additional study[266] (using a much larger, converged supercell) gives comparable numbers for the pristine graphene case, although giving slightly lower values of 19 eV and 13 eV for formation and healing of the SW defect. The anisotropy of the energy required to heal the SW defect at space angles (θ,φ) was mapped,[266] revealing the strong dependence on the direction of momentum transfer, as previously discussed for atom emission. In addition, this paper revealed the ability of a SW defect to migrate due to a single electron impact, provided one of two combinations of space angles and energy (18 or 20 eV) are achieved.

4.2.2 Vacancy structure rearrangements. Divacancy structures have been seen to convert between different stable states under electron irradiation.[147] These transformations can be understood in terms of individual or multiple SW rearrangements on bonds in the vacancy structures. A very in-depth study[266] mapped the threshold energies required for single-impact structure changes at different space angles for each of the V_2(5-8-5), V_2(555-777), V_2(555-6-777) and V_2(55-77) divacancy structures. It showed that the amount of energy required for a SW rearrangement is highly dependent on the angles of transferred momentum, ranging from 14 to 22 eV, and that different structures can result from impacts on the same atom, depending on the direction of momentum transfer. Fig. 17 shows a summary of these findings, giving the threshold energy for each SW rearrangement indicated by an arrow. It is worth noting the inclusion of the reconstructed V_2(55-77) divacancy, as typically only the previous three structures are discussed.[99] This structure can be achieved *via* the rotation of a different bond in the V_2(5-8-5) structure, however with a threshold energy of 21 eV compared to the 16 eV required for the V_2(5-8-5) to V_2(555-777) transformation. In addition, the reverse process of V_2(55-77) to V_2(5-8-5) has the lowest threshold energy of any divacancy rearrangement at 14 eV, and so while this structure should be able to form under irradiation, it would be expected to have a shorter lifetime compared to the other reconstructed divacancies. Indeed, while it is very rarely seen in TEM, an example of this structure forming from a V_2(5-8-5) vacancy, before quickly undergoing the reverse transformation, has been observed.[167] This structure also provides a low energy route to the formation of trivacancies, with only 14 eV required to remove an atom and form the V_3(5-10-5) structure.

Although the SW rearrangement has been shown to be responsible for a wide range of dynamical behaviour in larger vacancy structures, the need to map the anisotropy of the threshold energy, combined with an increasing number of inequivalent atoms and potential structures in larger vacancies, makes the calculation of threshold energies prohibitive. While several key structures of particular stability were found for the tetravacancy,[264] a large number of other structures were observed experimentally, each living for seconds at a time. Fig. 18 shows the 17 most frequently observed tetravacancy structures together with the SW rearrangements required to convert between them. Tight-binding MD simulations were carried out in order to demonstrate the evolution of the tetravacancy under electron irradiation in this manner,[264] however a full search of the impact angle space in order to

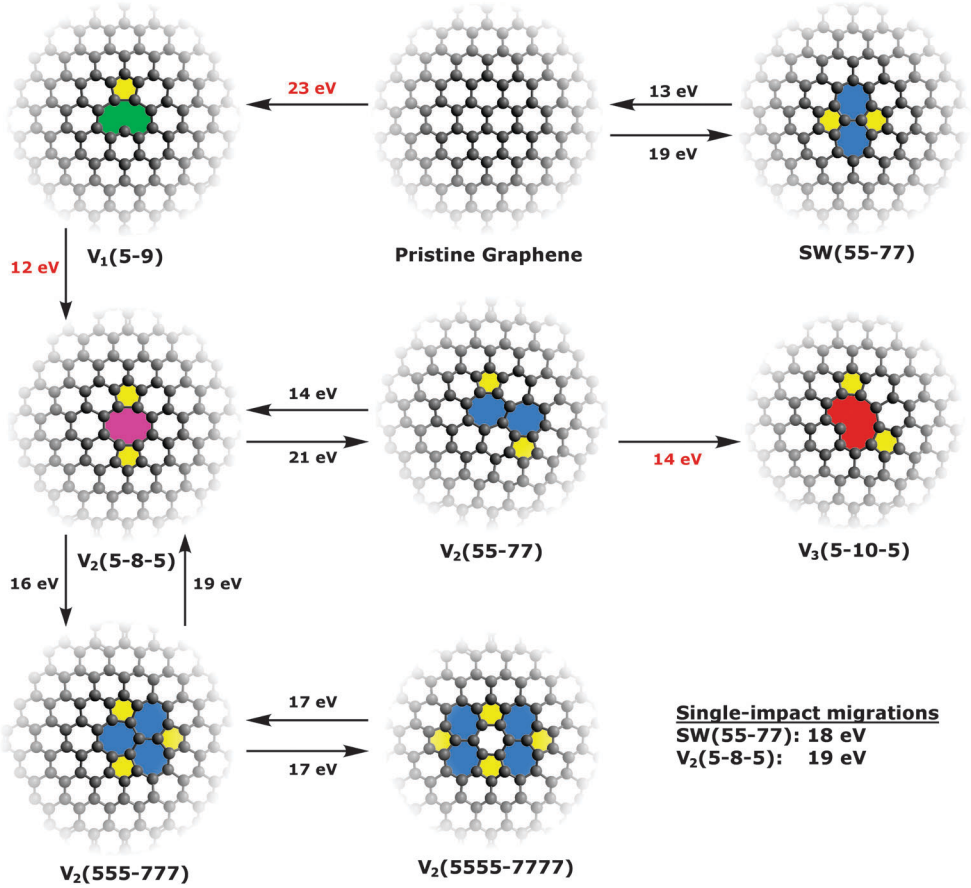

Fig. 17 A summary of the threshold energies calculated for irradiation-induced processes in ref. 266. Emission processes are labelled in red and bond rotations (SW rearrangements) in black. Rings are coloured according to their size: 5, yellow; 6, white; 7, blue; 8, purple; 9, green; 10, red. Threshold energies are also given for the direct migration of structures across the graphene lattice due to a single impact from the e-beam, only witnessed for a small number of combinations of angle space and transferred energy.

determine threshold energies for defect structures larger than divacancies has not been performed.

4.2.3 Vacancy migration. In addition to conversion between different stable structures, vacancy structures have been observed to migrate across the graphene lattice.[167] As the barrier to the thermal migration of monovacancies is in the region of 1–1.5 eV (Table 1), it is assumed that the monovacancy migration is primarily thermally driven. Impacts from the electron beam will typically transfer much more energy than this (at 80 kV the maximum transferrable energy to a carbon atom is 15.8 eV), and so electron impacts on monovacancies are generally assumed to result in the emission of the under-coordinated carbon atom, as discussed above. However, the barriers for thermal migration of larger vacancy structures are unreasonably large, and so the effects of the e-beam are assumed to be responsible for the experimentally witnessed migration. Two consecutive SW rearrangements are proposed to be responsible for a migration of the V_2(5-8-5) vacancy by one lattice unit *via* the V_2(55-77) structure.[167] The theoretical study described above[266] provided confirmation of the possibility of this proposed two-step mechanism; it confirms the ability of SW rearrangements to convert between the two divacancy structures, and the low irradiation stability of the V_2(55-77) structure (with the lowest threshold energy calculated, 14 eV) provides an explanation for both rearrangements happening in quick succession. An additional two step mechanism was proposed[167] for the V_2(5-8-5) vacancy rotating 60° around a pentagon, *via* an intermediate V_2(555-777) structure. The calculated threshold energies of these two steps, 16 eV and 19 eV, suggest that while this mechanism will be less likely to occur than the migration *via* the V_2(55-77) structure, it will be possible given an electron beam of sufficient energy. During the mapping of the threshold energies of various divacancy structures,[266] a previously unpredicted single-impact mechanism of V_2(5-8-5) migration was discovered, *via* bond breaking and reforming rather than through a direct bond rotation. The threshold energy of this process is 19 eV, and due to the requirement of only one electron impact it would be expected that this mechanism of migration would be especially prevalent at sufficiently high e-beam energies.

4.2.4 At graphene edges. The threshold energies for the bond rotation between the zigzag (ZZ) and reconstructed zigzag pentagon–heptagon ZZ(57) edges in graphene were calculated from experimental TEM images of torn graphene.[255] These calculations assumed that every scattering event that transferred energy

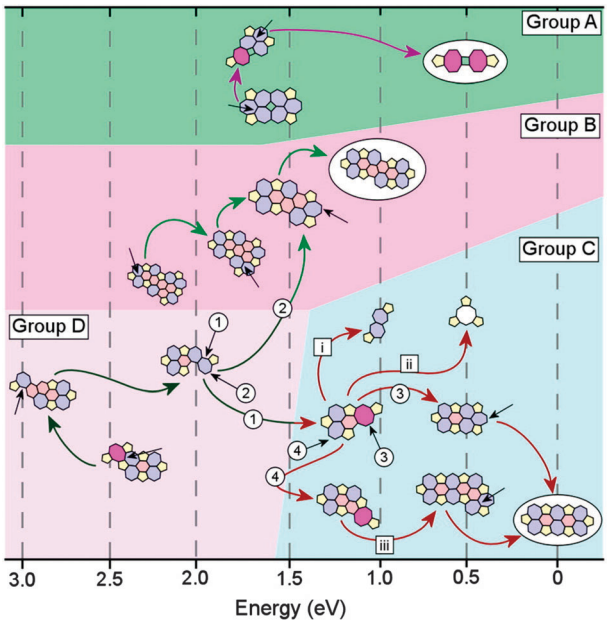

Fig. 18 SW rotations that allow for the conversion between different experimentally observed tetravacancy structures, the most frequently observed of which are circled. Each coloured arrow indicates a single SW rotation, except those numbered with Roman numerals which require two bond rotations. The bonds which rotate are indicated by black arrows. Configurations which can develop in one of two ways have numbered pathways corresponding to the respective numbered bond rotation. Reprinted (adapted) from ref. 264. Copyright (2014) American Chemical Society.

above the threshold energy would result in a transformation; they ignored the anisotropic dependence of the threshold energy. By observing the rates of conversion between the two structures, it was shown that the threshold for the ZZ to ZZ(57) rotation is 1.3 eV, while the ZZ(57) to ZZ rotation is 2.5 eV. These values are far lower than theoretical calculations of thresholds for SW rearrangements in the graphene interior, consistent with the smaller number of bonds that must be broken at the edge in order for a SW rearrangement to take place. It would be expected that in general, bond rotations will be far more prevalent at the edge than in the graphene interior.

In addition to conversions between the ZZ and ZZ(57) structures *via* a bond rotation, other SW rearrangements have been observed occurring during simulations of electron impacts below the emission threshold at various edge configurations.[148] Conversions between the AC and AC(57) edges and the AC and AC(667) edges were witnessed, while the AC to AC(56) transformation was always seen to occur following the emission of an atom. Threshold energies of these and other similar processes have not yet been calculated, but the knowledge of rates of conversion between structures could provide valuable insights into the dynamical behaviour of graphene edges under electron irradiation.

5. Conclusions

In the present paper we review the recent studies devoted to the energetics of formation, transformation, migration, coalescence and healing of defects in graphene. The cases of various vacancy-type and topological defects created due to bond realignment reactions in the graphene interior and at the graphene edge are considered, with both thermally activated and irradiation-induced processes taken into account.

The structure and formation energies for the monovacancy and many types of multi-vacancies in the graphene interior have been studied in detail. It has also been found that adatoms and single vacancies have low barriers for migration, about 0.5 eV and 1.0–1.4 eV, respectively, whereas barriers for divacancy migration exceed 5 eV. Thermally activated processes related to multi-vacancy formation and healing at room temperature will therefore be determined by the migration of adatoms and single vacancies. However, contradictory results have been obtained for the values of out-of-plane displacement, the barrier for transition between equivalent states of the 5/9 vacancy, and influence of interlayer interaction on the barrier for 5/9 vacancy motion in graphite. DFT calculations demonstrate a drastic change in the structure and energetics of a single vacancy near the graphene edge, and predict the fast directional motion of the vacancy to the edge at room temperature.[67,68] However these results have only been obtained on a few examples of rather small graphene flakes and narrow nanoribbons. Further detailed studies of the energetics of the vacancy near armchair and zigzag edges of semi-infinite graphene, both with dangling bonds and terminated by hydrogen and other atoms are necessary. A set of multi-vacancies with various structures formed due to vacancy coalescence have been found for free standing graphene. As strain has a drastic effect on the barrier to vacancy migration,[23,161] local strain could be used to control vacancy coalescence. Studies investigating the possibility of such control remain an open problem.

First-principles calculations clearly demonstrate that bond realignment reactions in the graphene interior have large barriers and should not take place even at high temperatures. The effect of strain on these reactions has been extensively studied in recent years, shedding light on the mechanisms of plastic deformations of graphene and carbon nanotubes. The catalytic effects of metal, carbon and hydrogen adatoms have been considered. Similar to vacancies, topological defects have been shown to result in out of plane buckling of graphene layers thus providing stress relaxation. However, the magnitude and energetics of the out of plane distortions are very sensitive to the calculation method used and the size of the periodic cell (or a finite system) considered. Therefore, more accurate studies are still required to get reliable data for the out of plane deformations caused by defects in graphene.

Graphene edges are found to be much more reactive than the graphene interior, and in the absence of strain or catalysing agents high-temperature transformations in graphene are concentrated at the edges. Significant efforts have been made to describe the reconstruction of zigzag edges. However, other types of bond realignment reactions at the edge have mostly been studied using semiempirical potentials, which are only qualitatively correct. Moreover, the investigation of sequential steps of defect generation has been focused on free (unfunctionalised) edges. More detailed first-principles analysis of various bond realignment reactions and

the inclusion of functionalised edges into consideration are therefore of interest. In particular, the formation of carbon chains at edges has been shown to play a leading role in high-temperature transformations of graphene flakes[70,71,87] and open-ended nanotubes,[88] and has been observed experimentally for graphene nanoribbons under electron irradiation.[13] More detailed investigation into chain formation reactions is required to understand these processes.

Quantitative studies of irradiation-induced processes of structure change in graphene overwhelmingly deal with the case of atom emission, predominantly from pristine graphene. The threshold energy for this process is very well known, with good agreement between experiment[146,267] and theoretical studies (Table 8), but similar studies for interesting defective types of graphene structure are lacking. While simulations considering edges[148] and small vacancy structures (up to divacancies)[266] have produced useful insights into the dynamics of these areas under electron irradiation, these remain the minority of cases. Even among the various divacancy structures, the V_2(55-77) dislocation dipole typically receives little attention, presumably due to it being a much rarer sight experimentally. However, the presence of low energy routes from this structure mean that it could be playing an important part in irradiation-induced vacancy dynamics. A threshold energy of 14 eV for the rearrangement back to the V_2(5-8-5) structure provides an accessible mechanism of divacancy migration, and a threshold energy of only 14 eV for the emission of an atom provides a low energy pathway to trivacancies and therefore to the creation of larger vacancy structures. Indeed, the low number of experimental observations of this structure may merely indicate that it typically has a short lifetime under the e-beam due to the presence of these low threshold processes.

Larger vacancy structures and commonly observed structures remain to be examined at all in terms of threshold energies of irradiation-induced processes. An especially important example of this is the stability and migration of grain boundaries in graphene. Emission threshold energies of different grain boundary configurations could help to explain experimentally seen structures, while the HRTEM observation of the atom-by-atom migration of a grain boundary has been reported,[20] mediated by individual bond rotations.

Bond rotations have been shown to be responsible for a wide range of atomic structure transformations in graphene, providing accessible routes between different stable structures. However, the theoretical estimation of threshold energies for this kind of process remains difficult due to the requirement of mapping the energy over the range of impact angles. This is reflected in the severe lack of data available for SW rearrangements in non-pristine graphene, with only several key studies providing quantitative understanding of these processes. For example, despite knowledge of the irradiation stabilities of a variety of edge configurations with respect to emission,[148] one of the very few examples of a quantitative study of bond rotations at the edge only deals with the conversion between a single pair of edge configurations,[255] and the threshold energies are calculated from the experimentally observed rates of conversion. As this makes the large assumption that any impact above the threshold energy would result in a bond rotation, theoretical calculations are necessary for comparison; mapping the anisotropy of this case as has been performed for divacancies[266] could provide accurate values of the threshold energy. Simulations have shown that similar conversions can occur between a variety of other edge reconstructions,[148] however even the relative threshold energies of these processes, and therefore the relative likelihood of their occurrence under the e-beam, are unknown.

Knowledge of threshold energies of irradiation-induced processes are key to understanding the dynamical behaviour of graphene under the e-beam, with multiple examples showing that this behaviour cannot be explained by simply considering the equilibrium energetics. Despite this, and with HRTEM increasingly becoming the *de facto* tool for the experimental study of the atomic structure of graphene, theoretical calculations of threshold energies and resulting cross-sections remain scarce compared to the wealth of data on thermal activation and formation energies.

In summary, there are several areas in which further calculations of the energetic characteristics of atomic scale structure changes in graphene are necessary: (1) the presence and magnitude of out of plane displacements in 5/9 monovacancies, SW defects, dislocation cores and other defects, (2) the barrier for the transition between equivalent states of the 5/9 vacancy, (3) detailed energetics for the vacancy migration to graphene edges, (4) the control of vacancy migration and coalescence by local strain, (5) detailed energetics for bond realignment reactions at graphene edges, beyond the formation of pentagon–heptagon pairs at the zigzag edge, (6) detailed energetics of bond realignment reactions at hydrogenated and other types of functionalised edges, (7) detailed energetics of the formation of carbon chains at different types of edges, (8) threshold energies of structure changes (emission and migration by bond rotation) at grain boundaries, (9) both qualitative (relative rates) and quantitative (threshold energies) details of conversions between different edge configurations, (10) threshold energies of processes involving vacancy structures larger than divacancies.

Acknowledgements

EB acknowledges ERC Consolidator Grant for financial support. AP and IL acknowledge Russian Foundation of Basic Research (14-02-00739-a). IL acknowledges support by the Marie Curie International Incoming Fellowship within the 7th European Community Framework Programme (Grant Agreement PIIF-GA-2012-326435 RespSpatDisp), Grupos Consolidados del Gobierno Vasco (IT-578-13).

Notes and references

1 S. Iijima, *Nature*, 1991, **354**, 56–58, DOI: 10.1038/354056a0.
2 K. S. Novoselov, A. K. Geim, S. V. Morozov, D. Jiang, Y. Zhang, S. V. Dubonos, I. V. Grigorieva and A. A. Firsov, *Science*, 2004, **306**, 666–669, DOI: 10.1126/science.110. 2896.

3 A. Chuvilin, E. Bichoutskaia, M. C. Gimenez-Lopez, T. W. Chamberlain, G. A. Rance, N. Kuganathan, J. Biskupek, U. Kaiser and A. N. Khlobystov, *Nat. Mater.*, 2011, **10**, 687–692, DOI: 10.1038/nmat3082.
4 T. W. Chamberlain, J. Biskupek, G. A. Rance, A. Chuvilin, T. J. Alexander, E. Bichoutskaia, U. Kaiser and A. N. Khlobystov, *ACS Nano*, 2012, **6**, 3943–3953, DOI: 10.1021/nn300137j.
5 W. A. De Heer and D. Ugarte, *Chem. Phys. Lett.*, 1993, **207**, 480–486, DOI: 10.1016/0009-2614(93)89033-E.
6 S. Bandow, M. Takizawa, K. Hirahara, M. Yadasako and S. Iijima, *Chem. Phys. Lett.*, 2001, **337**, 48–54, DOI: 10.1016/S0009-2614(01)00192-0.
7 B. Song, G. F. Schneider, Q. Xu, G. Pandraud, C. Dekker and H. Zandbergen, *Nano Lett.*, 2011, **11**, 2247–2250, DOI: 10.1021/nl200369r.
8 A. Chuvilin, U. Kaiser, E. Bichoutskaia, N. A. Besley and A. N. Khlobystov, *Nat. Chem.*, 2010, **2**, 450–453, DOI: 10.1038/nchem.644.
9 D. Ugarte, *Nature*, 1992, **359**, 707–709, DOI: 10.1038/359707a0.
10 D. Ugarte, *Chem. Phys. Lett.*, 1993, **207**, 473–479, DOI: 10.1016/0009-2614(93)89032-D.
11 J. Sloan, R. E. Dunin-Borkowski, J. L. Hutchison, K. S. Coleman, V. C. Williams, J. B. Claridge, A. P. E. York, C. G. Xu, S. R. Bailey, G. Brown, S. Friedrichs and M. L. H. Green, *Chem. Phys. Lett.*, 2000, **316**, 191–198, DOI: 10.1016/S0009-2614(99)01250-6.
12 C. S. Allen, Y. Ito, A. W. Robertson, H. Shinohara and J. H. Warner, *ACS Nano*, 2011, **5**, 10084–10089, DOI: 10.1021/nn204003h.
13 A. Chuvilin, J. C. Meyer, G. Algara-Siller and U. Kaiser, *New J. Phys.*, 2009, **11**, 083019, DOI: 10.1088/1367-2630/11/8/083019.
14 C. Jin, H. Lan, L. Peng, K. Suenaga and S. Iijima, *Phys. Rev. Lett.*, 2009, **102**, 205501, DOI: 10.1103/PhysRevLett.102.205501.
15 S. T. Skowron, I. V. Lebedeva, A. M. Popov and E. Bichoutskaia, *Nanoscale*, 2013, **5**, 6677–6692, DOI: 10.1039/c3nr02130k.
16 P. M. Ajayan, V. Ravikumar and J.-C. Charlier, *Phys. Rev. Lett.*, 1998, **81**, 1437–1441, DOI: 10.1103/PhysRevLett.81.1437.
17 C. Jin, K. Suenaga and S. Iijima, *Nano Lett.*, 2008, **8**, 1127–1130, DOI: 10.1021/nl0732676.
18 J. Y. Huang, S. Chen, Z. Q. Wang, K. Kempa, Y. M. Wang, S. H. Jo, G. Chen, M. S. Dresselhaus and Z. F. Ren, *Nature*, 2006, **439**, 281, DOI: 10.1038/439281a.
19 J. Y. Huang, S. Chen, Z. F. Ren, Z. Wang, K. Kempa, M. J. Naughton, G. Chen and M. S. Dresselhaus, *Phys. Rev. Lett.*, 2007, **98**, 185501, DOI: 10.1103/PhysRevLett.98.185501.
20 S. Kurasch, J. Kotakoski, O. Lehtinen, V. Skákalová, J. Smet, C. E. Krill, A. V. Krasheninnikov and U. Kaiser, *Nano Lett.*, 2012, **12**, 3168–3173, DOI: 10.1021/nl301141g.
21 Y. Ma, P. O. Lehtinen, A. S. Foster and R. M. Nieminen, *New J. Phys.*, 2004, **6**, 68, DOI: 10.1088/1367-2630/6/1/068.
22 L. Xu, N. Wei and Y. Zheng, *Nanotechnology*, 2013, **24**, 505703, DOI: 10.1088/0957-4484/24/50/505703.
23 A. S. Fedorov, D. A. Fedorov, Z. I. Popov, Y. E. Anan'eva, N. S. Eliseeva and A. A. Kuzubov, *J. Exp. Theor. Phys.*, 2011, **112**, 820–824, DOI: 10.1134/S1063776111040042.
24 A. S. Fedorov, Z. I. Popov, D. A. Fedorov, N. S. Eliseeva, M. V. Serjantova and A. A. Kuzubov, *Phys. Status Solidi B*, 2012, **249**, 2549–2552, DOI: 10.1002/pssb.201200105.
25 R. Dettori, E. Cadelano and L. Colombo, *J. Phys.: Condens. Matter*, 2012, **24**, 104020, DOI: 10.1088/0953-8984/24/10/104020.
26 F. Hao, D. Fang and Z. Xu, *Appl. Phys. Lett.*, 2011, **99**, 041901, DOI: 10.1063/1.3615290.
27 B. Mortazavi and S. Ahzi, *Carbon*, 2013, **63**, 460–470, DOI: 10.1016/j.carbon.2013.07.017.
28 N. Jing, Q. Xue, C. Ling, M. Shan, T. Zhang, X. Zhou and Z. Jiao Z, *RSC Adv.*, 2012, **2**, 9124–9129, DOI: 10.1039/c2ra21228e.
29 R. Ansari, S. Ajori and B. Motevalli, *Superlattices Microstruct.*, 2012, **51**, 274–289, DOI: 10.1016/j.spmi.2011.11.019.
30 S. P. Wang, J. G. Guo and L. J. Zhou, *Physica E*, 2013, **48**, 29–35, DOI: 10.1016/j.physe.2012.11.002.
31 M. C. Wang, C. Yan, L. Ma, N. Hu and M. W. Chen, *Comput. Mater. Sci.*, 2012, **54**, 236–239, DOI: 10.1016/j.commatsci.2011.10.032.
32 C. Baykasoglu and A. Mugan, *Eng. Fract. Mech.*, 2012, **96**, 241–250, DOI: 10.1016/j.engfracmech.2012.08.010.
33 A. Lherbier, S. M.-M. Dubois, X. Declerck, S. Roche, Y.-M. Niquet and J.-C. Charlier, *Phys. Rev. Lett.*, 2011, **106**, 046803, DOI: 10.1103/PhysRevLett.106.046803.
34 A. Lherbier, S. M.-M. Dubois, X. Declerck, Y.-M. Niquet, S. Roche and J.-C. Charlier, *Phys. Rev. B: Condens. Matter Mater. Phys.*, 2012, **86**, 075402, DOI: 10.1103/PhysRevB.86.075402.
35 K. Ulman and S. Narasimhan, *Phys. Rev. B: Condens. Matter Mater. Phys.*, 2014, **89**, 245429, DOI: 10.1103/PhysRevB.89.245429.
36 S. N. Shirodkar and U. V. Waghmare, *Phys. Rev. B: Condens. Matter Mater. Phys.*, 2012, **86**, 165401, DOI: 10.1103/PhysRevB.86.165401.
37 J. Kang, J. Bang, B. Ryu and K. J. Chang, *Phys. Rev. B: Condens. Matter Mater. Phys.*, 2008, **77**, 115453, DOI: 10.1103/PhysRevB.77.115453.
38 S. Chowdhury, S. Baidya, D. Nafday, S. Halder, M. Kabir, B. Sanyal, T. Saha-Dasgupta, D. Jana and A. Mookerjee, *Physica E*, 2014, **61**, 191–197, DOI: 10.1016/j.physe.2014.04.002.
39 V. H. Crespi, M. L. Cohen and A. Rubio, *Phys. Rev. Lett.*, 1997, **79**, 2093–2096, DOI: 10.1103/PhysRevLett.79.2093.
40 J. C. Carlsson and M. Scheffler, *Phys. Rev. Lett.*, 2006, **96**, 046806, DOI: 10.1103/PhysRevLett.96.046806.
41 D. Selli and F. Mercuri, *Carbon*, 2014, **75**, 190–200, DOI: 10.1016/j.carbon.2014.03.052.
42 G. Wang, *Phys. Chem. Chem. Phys.*, 2011, **13**, 11939–11945, DOI: 10.1039/c1cp20541b.
43 H. Zeng, J.-P. Leburton, Y. Xu and J. Wei, *Nanoscale Res. Lett.*, 2011, **6**, 254, DOI: 10.1186/1556-276X-6-254.
44 Y. Ren and K.-Q. Chen, *J. Appl. Phys.*, 2010, **107**, 044514, DOI: 10.1063/1.3309775.
45 P. O. Lehtinen, A. F. Foster, Y. Ma, A. V. Krasheninnikov and R. M. Nieminen, *Phys. Rev. Lett.*, 2004, **93**, 187202, DOI: 10.1103/PhysRevLett.93.187202.

46 O. V. Yazyev and L. Helm, *Phys. Rev. B: Condens. Matter Mater. Phys.*, 2007, **75**, 125408, DOI: 10.1103/PhysRevB.75.125408.
47 S. Choi, B. W. Jeong, S. Kim and G. Kim, *J. Phys.: Condens. Matter*, 2008, **20**, 235220, DOI: 10.1088/0953-8984/20/23/235220.
48 R. Singh and P. Kroll, *J. Phys.: Condens. Matter*, 2009, **21**, 196002, DOI: 10.1088/0953-8984/21/19/196002.
49 X. Q. Dai, J. H. Zhao, M. H. Xie, Y. N. Tang, Y. H. Li and B. Zhao, *Eur. Phys. J. B*, 2011, **80**, 343–349, DOI: 10.1140/epjb/e2011-10955-x.
50 R. Faccio and A. W. Mombrú, *J. Phys.: Condens. Matter*, 2012, **24**, 375304, DOI: 10.1088/0953-8984/24/37/375304.
51 E. J. G. Santos, S. Riikonen, D. Sánchez-Portal and A. Ayuela, *J. Phys. Chem. C*, 2012, **116**, 7602–7606, DOI: 10.1021/jp300861m.
52 B. Wang and S. T. Pantelides, *Phys. Rev. B: Condens. Matter Mater. Phys.*, 2012, **86**, 165438, DOI: 10.1103/PhysRevB.86.165438.
53 V. O. Özçelik, H. H. Gurel and S. Ciraci, *Phys. Rev. B: Condens. Matter Mater. Phys.*, 2013, **88**, 045440, DOI: 10.1103/PhysRevB.88.045440.
54 P. A. Denis, R. Faccio and F. Iribarne, *Comput. Theor. Chem.*, 2012, **995**, 1–7, DOI: 10.1016/j.comptc.2012.06.014.
55 P. Lu, Z. Zhang and W. Guo, *Phys. Lett. A*, 2009, **373**, 3354–3358, DOI: 10.1016/j.physleta.2009.07.031.
56 J.-W. Jiang, B.-S. Wang and J.-S. Wang, *Appl. Phys. Lett.*, 2011, **98**, 113114, DOI: 10.1063/1.3567768.
57 Z. G. Fthenakis, Z. Zhu and D. Tománek, *Phys. Rev. B: Condens. Matter Mater. Phys.*, 2014, **89**, 125421, DOI: 10.1103/PhysRevB.89.125421.
58 Y. Y. Zhang, Y. Cheng, Q. X. Pei, C. M. Wang and Y. Xiang, *Phys. Lett. A*, 2012, **376**, 3668–3672, DOI: 10.1016/j.physleta.2012.10.048.
59 Z. X. Xie, K.-Q. Chen and W. Duan, *J. Phys.: Condens. Matter*, 2011, **23**, 315302, DOI: 10.1088/0953-8984/23/31/315302.
60 J. Haskins, A. Kınacı, C. Sevik, H. Sevinçli, G. Cuniberti and T. Çağın, *ACS Nano*, 2011, **5**, 3779–3787, DOI: 10.1021/nn200114p.
61 D. Yang, F. Ma, Y. Sun, T. Hu and K. Xu, *Appl. Surf. Sci.*, 2012, **258**, 9926–9931, DOI: 10.1016/j.apsusc.2012.06.052.
62 A. V. Krasheninnikov, K. Nordlund and J. Keinonen, *Phys. Rev. B: Condens. Matter Mater. Phys.*, 2002, **65**, 165423, DOI: 10.1103/PhysRevB.65.165423.
63 J.-W. Jiang and J.-S. Wang, *J. Appl. Phys.*, 2010, **108**, 054303, DOI: 10.1063/1.3481004.
64 B. Song, G. F. Schneider, Q. Xu, G. Pandraud, C. Dekker and H. Zandbergen, *Nano Lett.*, 2011, **11**, 2247–2250, DOI: 10.1021/nl200369r.
65 A. W. Robertson, C. S. Allen, Y. A. Wu, K. He, J. Olivier, J. Neethling, A. I. Kirkland and J. H. Warner, *Nat. Commun.*, 2012, **3**, 1144–1151, DOI: 10.1038/ncomms2141.
66 A. W. Robertson, G.-D. Lee, K. He, E. Yoon, A. I. Kirkland and J. H. Warner, *Nano Lett.*, 2014, **14**, 3972–3980, DOI: 10.1021/nl501320a.
67 A. Santana, A. M. Popov and E. Bichoutskaia, *Chem. Phys. Lett.*, 2013, **557**, 80–87, DOI: 10.1016/j.cplett.2012.11.077.
68 X. Gao, L. Liu, S. Irle and S. Nagase, *Angew. Chem., Int. Ed.*, 2010, **49**, 3200–3202, DOI: 10.1002/anie.200907347.
69 M. W. C. Dharma-wardana and M. Z. Zgierski, *Physica E*, 2008, **41**, 80–83, DOI: 10.1016/j.physe.2008.06.007.
70 I. V. Lebedeva, A. A. Knizhnik, A. A. Bagatur'yants and B. V. Potapkin, *Physica E*, 2008, **40**, 2589–2595, DOI: 10.1016/j.physe.2007.09.155.
71 I. V. Lebedeva, A. A. Knizhnik and B. V. Potapkin, *Russ. J. Phys. Chem. B*, 2007, **1**, 675–684, DOI: 10.1134/S1990793107060255.
72 A. W. Robertson and J. H. Warner, *Nanoscale*, 2013, **5**, 4079–4093, DOI: 10.1039/c3nr00934c.
73 Y. C. Cheng, H. T. Wang, Z. Y. Zhu, Y. H. Zhu, Y. Han, X. X. Zhang and U. Schwingenschlögl, *Phys. Rev. B: Condens. Matter Mater. Phys.*, 2012, **85**, 073406, DOI: 10.1103/PhysRevB.85.073406.
74 Z. Liu, Y.-C. Lin, C.-C. Lu, C.-H. Yeh, P.-W. Chiu, S. Iijima and K. Suenaga K, *Nat. Commun.*, 2014, **5**, 4055, DOI: 10.1038/ncomms5055.
75 P. Koskinen, S. Malola and H. Häkkinen, *Phys. Rev. B: Condens. Matter Mater. Phys.*, 2009, **80**, 073401, DOI: 10.1103/PhysRevB.80.073401.
76 C. D. Reddy, A. Ramasubramaniam, V. B. Shenoy and Y.-W. Zhang, *Appl. Phys. Lett.*, 2009, **94**, 101904, DOI: 10.1063/1.3094878.
77 Y. C. Cheng, Z. Y. Zhu and U. Schwingenschlögl, *J. Mater. Chem.*, 2012, **22**, 24676–24680, DOI: 10.1039/c2jm34068b.
78 J. N. B. Rodrigues, P. A. D. Gonçalves, N. F. G. Rodrigues, R. M. Ribeiro, J. M. B. Lopes dos Santos and N. M. R. Peres, *Phys. Rev. B: Condens. Matter Mater. Phys.*, 2011, **84**, 155435, DOI: 10.1103/PhysRevB.84.155435.
79 J. Li, Z. Li, G. Zhou, Z. Liu, J. Wu, B.-L. Gu, J. Ihm and W. Duan, *Phys. Rev. B: Condens. Matter Mater. Phys.*, 2010, **82**, 115410, DOI: 10.1103/PhysRevB.82.115410.
80 J. Bhattacharjee, *J. Chem. Phys.*, 2012, **137**, 094705, DOI: 10.1063/1.4747547.
81 S. M.-M. Dubois, A. Lopez-Bezanilla, A. Cresti, F. Triozon, B. Biel, J.-C. Charlier and S. Roche, *ACS Nano*, 2010, **4**, 1971–1976, DOI: 10.1021/nn100028q.
82 P. Hawkins, M. Begliarbekov, M. Zivkovic, S. Strauf and C. P. Search, *J. Phys. Chem. C*, 2012, **116**, 18382–18387, DOI: 10.1021/jp304676h.
83 S. Ihnatsenka and G. Kirczenow, *Phys. Rev. B: Condens. Matter Mater. Phys.*, 2013, **88**, 125430, DOI: 10.1103/PhysRevB.88.125430.
84 L. T. Nguyen, C. H. Pham and V. L. Nguyen, *J. Phys.: Condens. Matter*, 2011, **23**, 295503, DOI: 10.1088/0953-8984/23/29/295503.
85 H. Zheng, J. Zhao, D. Xu, J. Wei and H. Zhang, *Eur. Phys. J. B*, 2013, **86**, 80, DOI: 10.1140/epjb/e2013-30754-7.
86 J. Lan, Y. Cai, G. Zhang, J.-S. Wang and Y.-W. Zhang, *J. Phys. D: Appl. Phys.*, 2014, **47**, 265303, DOI: 10.1088/0022-3727/47/26/265303.
87 I. V. Lebedeva, A. A. Knizhnik, A. M. Popov and B. V. Potapkin, *J. Phys. Chem. C*, 2012, **116**, 6572–6584, DOI: 10.1021/jp212165g.

88 G. Zheng, S. Irle, M. Elstner and K. Morokuma, *J. Phys. Chem. A*, 2004, **108**, 3182–3194, DOI: 10.1021/jp0373090.
89 M. Volpe and F. Cleri, *J. Chem. Phys.*, 2001, **115**, 3308–3314, DOI: 10.1063/1.1387448.
90 S. S. Han, K. S. Lee and H. M. Lee, *Chem. Phys. Lett.*, 2004, **383**, 321–325, DOI: 10.1016/j.cplett.2003.11.033.
91 L. Meng, J. Jiang, J. Wang and F. Ding, *J. Phys. Chem. C*, 2014, **118**, 720–724, DOI: 10.1021/jp409471a.
92 G.-D. Lee, C. Z. Wang, E. Yoon, N. M. Hwang and K. M. Ho, *Appl. Phys. Lett.*, 2008, **92**, 043104, DOI: 10.1063/1.2837632.
93 G.-D. Lee, C. Z. Wang, E. Yoon, N. M. Hwang and K. M. Ho, *Phys. Rev. B: Condens. Matter Mater. Phys.*, 2007, **76**, 165413, DOI: 10.1103/PhysRevB.76.165413.
94 I. V. Lebedeva, T. W. Chamberlain, A. M. Popov, A. A. Knizhnik, T. Zoberbier, J. Biskupek, U. Kaiser and A. N. Khlobystov, *Nanoscale*, 2014, **6**, 14877, DOI: 10.1039/c4nr05006a.
95 S. Haghighatpanah, A. Börjesson, H. Amara, C. Bichara and K. Bolton, *Phys. Rev. B: Condens. Matter Mater. Phys.*, 2012, **85**, 205448, DOI: 10.1103/PhysRevB.85.205448.
96 G.-D. Lee, C. Z. Wang, E. Yoon, N.-M. Hwang and K. M. Ho, *Phys. Rev. B: Condens. Matter Mater. Phys.*, 2010, **81**, 195419, DOI: 10.1103/PhysRevB.81.195419.
97 A. V. Krasheninnikov and F. Banhart, *Nat. Mater.*, 2007, **6**, 723–733, DOI: 10.1038/nmat1996.
98 A. V. Krasheninnikov and K. Nordlund, *J. Appl. Phys.*, 2010, **107**, 071301, DOI: 10.1063/1.3318261.
99 F. Banhart, J. Kotakoski and A. V. Krasheninnikov, *ACS Nano*, 2011, **5**, 26–41, DOI: 10.1021/nn102598m.
100 H. Terrones, R. Lu, M. Terrones and M. S. Dresselhaus, *Rep. Prog. Phys.*, 2012, **75**, 062501, DOI: 10.1088/0034-4885/75/6/062501.
101 A. Bachmatiuk, J. Zhao, S. M. Gorantla, I. G. G. Martinez, J. Wiedermann, C. Lee, J. Eckert and M. H. Rummeli, *Small*, 2015, **5**, 515–542, DOI: 10.1002/smll.201401804.
102 P. Hohenberg and W. Kohn, *Phys. Rev.*, 1964, **136**, B864–B871, DOI: 10.1103/PhysRev.136.B864.
103 W. Kohn and L. J. Sham, *Phys. Rev.*, 1965, **140**, A1133–A1138, DOI: 10.1103/PhysRev.140.A1133.
104 J. P. Perdew and A. Zunger, *Phys. Rev. B: Condens. Matter Mater. Phys.*, 1981, **23**, 5048–5079, DOI: 10.1103/PhysRevB.23.5048.
105 J. P. Perdew, in *Electronic Structure of Solids '91*, ed. P. Ziesche and H. Eschrig, Akademie Verlag, Berlin, 1991, pp. 11–20.
106 J. P. Perdew, J. A. Chevary, S. H. Vosko, K. A. Jackson, M. R. Pederson, D. J. Singh and C. Fiolhais, *Phys. Rev. B: Condens. Matter Mater. Phys.*, 1992, **46**, 6671–6687, DOI: 10.1103/PhysRevB.46.6671.
107 J. P. Perdew, K. Burke and M. Ernzerhof, *Phys. Rev. Lett.*, 1996, **77**, 3865–3868, DOI: 10.1103/PhysRevLett.77.3865.
108 J. P. Perdew, K. Burke and M. Ernzerhof, *Phys. Rev. Lett.*, 1997, **78**, 1396, DOI: 10.1103/PhysRevLett.78.1396.
109 C. Adamo and V. Barone, *J. Chem. Phys.*, 1999, **110**, 6158–6170, DOI: 10.1063/1.478522.
110 S. F. Boys and F. Bernardi, *Mol. Phys.*, 1970, **19**, 553–566, DOI: 10.1080/00268977000101561.
111 E. Ruiz, A. Rodríguez-Fortea, J. Tercero, T. Cauchy and C. Massobrio, *J. Chem. Phys.*, 2005, **123**, 074102, DOI: 10.1063/1.1999631.
112 Y. Zhao and D. G. Truhlar, *J. Chem. Phys.*, 2006, **125**, 194101, DOI: 10.1063/1.2370993.
113 Y. Zhao and D. G. Truhlar, *Acc. Chem. Res.*, 2008, **41**, 157–167, DOI: 10.1021/ar700111a.
114 M. Dion, H. Rydberg, E. Schröder, D. C. Langreth and B. I. Lundqvist, *Phys. Rev. Lett.*, 2004, **92**, 246401, DOI: 10.1103/PhysRevLett.92.246401.
115 S. Grimme, *J. Comput. Chem.*, 2004, **25**, 1463–1473, DOI: 10.1002/jcc.20078.
116 S. Grimme, *J. Comput. Chem.*, 2006, **27**, 1787–1799, DOI: 10.1002/jcc.20495.
117 T. Frauenheim, G. Seifert, M. Elstner, Z. Hajnal, G. Jungnickel, D. Porezag, S. Suhai and S. Scholz, *Phys. Status Solidi B*, 2000, **217**, 41–62, DOI: 10.1002/(SICI)1521-3951(200001)217:1<41::AID-PSSB41>3.0.CO;2-V.
118 M. Elstner, D. Porezag, G. Jungnickel, J. Elsner, M. Haugk, T. Frauenheim, S. Suhai and G. Seifert, *Phys. Rev. B: Condens. Matter Mater. Phys.*, 1998, **58**, 7260–7268, DOI: 10.1103/PhysRevB.58.7260.
119 C. H. Xu, C. L. Fu and D. F. Pedraza, *Phys. Rev. B: Condens. Matter Mater. Phys.*, 1993, **48**, 13273–13279, DOI: 10.1103/PhysRevB.48.13273.
120 T. Frauenheim, G. Seifert, M. Elstner, T. Niehaus, C. Köhler, M. Amkreutz, M. Sternberg, Z. Hajnal, A. Di Carlo and S. Suhai, *J. Phys.: Condens. Matter*, 2002, **14**, 3015–3047, DOI: 10.1088/0953-8984/14/11/313.
121 http://www.dftb-plus.info/.
122 M. S. Tang, C. Z. Wang, C. T. Chan and K. M. Ho, *Phys. Rev. B: Condens. Matter Mater. Phys.*, 1996, **53**, 979–982, DOI: 10.1103/PhysRevB.53.979.
123 A. J. Lu and B. C. Pan, *Phys. Rev. Lett.*, 2004, **92**, 105504, DOI: 10.1103/PhysRevLett.92.105504.
124 G.-D. Lee, C. Z. Wang, E. Yoon, N.-M. Hwang and K. M. Ho, *Phys. Rev. B: Condens. Matter Mater. Phys.*, 2006, **74**, 245411, DOI: 10.1103/PhysRevB.74.245411.
125 P. M. Morse, *Phys. Rev.*, 1929, **34**, 57–64, DOI: 10.1103/PhysRev.34.57.
126 G. C. Abell, *Phys. Rev. B: Condens. Matter Mater. Phys.*, 1985, **31**, 6184–6196, DOI: 10.1103/PhysRevB.31.6184.
127 J. Tersoff, *Phys. Rev. Lett.*, 1988, **61**, 2879–2882, DOI: 10.1103/PhysRevLett.61.2879.
128 D. W. Brenner, *Phys. Rev. B: Condens. Matter Mater. Phys.*, 1990, **42**, 9458–9471, DOI: 10.1103/PhysRevB.42.9458.
129 D. W. Brenner, O. A. Shenderova, J. A. Harrison, S. J. Stuart, B. Ni and S. B. Sinnott, *J. Phys.: Condens. Matter*, 2002, **14**, 783–802, DOI: 10.1088/0953-8984/14/4/312.
130 S. J. Stuart, A. B. Tutein and J. A. Harrison, *J. Chem. Phys.*, 2000, **112**, 6472–6486, DOI: 10.1063/1.481208.
131 K. Albe, K. Nordlund and R. S. Averback, *Phys. Rev. B: Condens. Matter Mater. Phys.*, 2002, **65**, 195124, DOI: 10.1103/PhysRevB.65.195124.

132 K. O. E. Henriksson and K. Nordlund, *Phys. Rev. B: Condens. Matter Mater. Phys.*, 2009, **79**, 144107, DOI: 10.1103/PhysRevB.79.144107.
133 A. S. Sinitsa, I. V. Lebedeva, A. A. Knizhnik, A. M. Popov, S. T. Skowron and E. Bichoutskaia, *Dalton Trans.*, 2014, **43**, 7499–7513, DOI: 10.1039/c3dt53385a.
134 A. C. T. van Duin, S. Dasgupta, F. Lorant and W. A. Goddard III, *J. Phys. Chem. A*, 2001, **105**, 9396–9409, DOI: 10.1021/jp004368u.
135 K. D. Nielson, A. C. T. van Duin, J. Oxgaard, W. Q. Deng and W. A. Goddard III, *J. Phys. Chem. A*, 2005, **109**, 493–499, DOI: 10.1021/jp046244d.
136 M. J. Buehler, A. C. T. van Duin and W. A. Goddard III, *Phys. Rev. Lett.*, 2006, **96**, 095505, DOI: 10.1103/PhysRevLett.96.095505.
137 C. Peng and H. B. Schlegel, *Isr. J. Chem.*, 1993, **33**, 449–454, DOI: 10.1002/ijch.199300051.
138 Ge. G. Samsonidze, G. G. Samsonidze and B. I. Yakobson, *Comput. Mater. Sci.*, 2002, **23**, 62–72, DOI: 10.1016/S0927-0256(01)00220-8.
139 G. Henkelman, B. P. Uberuaga and H. A. Jonsson, *J. Chem. Phys.*, 2000, **113**, 9901–9904, DOI: 10.1063/1.1329672.
140 E. Bitzek, P. Koskinen, F. Gähler, M. Moseler and P. Gumbsh, *Phys. Rev. Lett.*, 2006, **97**, 170201, DOI: 10.1103/PhysRevLett.97.170201.
141 D. Passerone and M. Parrinello, *Phys. Rev. Lett.*, 2001, **87**, 108302, DOI: 10.1103/PhysRevLett.87.108302.
142 A. T. Lee, B. Ryu, I.-H. Lee and K. J. Chang, *J. Phys.: Condens. Matter*, 2014, **26**, 115303, DOI: 10.1088/0953-8984/26/11/115303.
143 M. P. Allen and D. J. Tildesley, *Computer simulation of liquids*, Clarendon Press, Oxford, 1987.
144 M. J. Field, *A practical introduction to the simulation of molecular systems*, Cambridge University Press, Cambridge, 2007.
145 K. Binder and D. Heermann, *Monte Carlo simulation in statistical physics – an introduction*, Springer-Verlag, Berlin Heidelberg New York, 2010.
146 J. C. Meyer, F. Eder, S. Kurasch, V. Skakalova, J. Kotakoski, H. J. Park, S. Roth, A. Chuvilin, S. Eyhusen, G. Benner, A. V. Krasheninnikov and U. Kaiser, *Phys. Rev. Lett.*, 2012, **108**, 196102, DOI: 10.1103/PhysRevLett.108.196102.
147 J. Kotakoski, J. C. Meyer, S. Kurasch, D. Santos-Cottin, U. Kaiser and A. V. Krasheninnikov, *Phys. Rev. B: Condens. Matter Mater. Phys.*, 2011, **83**, 245420, DOI: 10.1103/PhysRevB.83.245420.
148 J. Kotakoski, D. Santos-Cottin and A. V. Krasheninnikov, *ACS Nano*, 2012, **6**, 671–676, DOI: 10.1021/nn204148h.
149 A. Zobelli, A. Gloter, C. P. Ewels, G. Seifert and C. Colliex, *Phys. Rev. B: Condens. Matter Mater. Phys.*, 2007, **75**, 245402, DOI: 10.1103/PhysRevB.75.245402.
150 J. Kotakoski, C. H. Jin, O. Lehtinen, K. Suenaga and A. V. Krasheninnikov, *Phys. Rev. B: Condens. Matter Mater. Phys.*, 2010, **82**, 113404, DOI: 10.1103/PhysRevB.82.113404.
151 A. Santana, A. Zobelli, J. Kotakoski, A. Chuvilin and E. Bichoutskaia, *Phys. Rev. B: Condens. Matter Mater. Phys.*, 2013, **87**, 094110, DOI: 10.1103/PhysRevB.87.094110.
152 E. Kaxiras and K. C. Pandey, *Phys. Rev. Lett.*, 1988, **61**, 2693–2697, DOI: 10.1103/PhysRevLett.61.2693.
153 A. A. El-Barbary, R. H. Telling, C. P. Ewels, M. I. Heggie and P. R. Briddon, *Phys. Rev. B: Condens. Matter Mater. Phys.*, 2003, **68**, 144107, DOI: 10.1103/PhysRevB.68.144107.
154 J. Kotakoski, A. V. Krasheninnikov and K. Nordlund, *Phys. Rev. B: Condens. Matter Mater. Phys.*, 2006, **74**, 245420, DOI: 10.1103/PhysRevB.74.245420.
155 A. V. Krasheninnikov, P. O. Lehtinen, A. S. Foster and R. M. Nieminen, *Chem. Phys. Lett.*, 2006, **418**, 132–136, DOI: 10.1016/j.cplett.2005.10.106.
156 M. Saito, K. Yamashita and T. Oda, *Jpn. J. Appl. Phys.*, 2007, **46**, L1185–1187, DOI: 10.1143/JJAP.46.L1185.
157 H. Zhang, M. Zhao, X. Yang, H. Xia, X. Liu and Y. Xia, *Diamond Relat. Mater.*, 2010, **19**, 1240–1244, DOI: 10.1016/j.diamond.2010.06.010.
158 B. R. K. Nanda, M. Sherafati, Z. S. Popović and S. Satpathy, *New J. Phys.*, 2012, **14**, 083004, DOI: 10.1088/1367-2630/14/8/083004.
159 A. W. Robertson, B. Montanari, K. He, C. S. Allen, Y. A. Wu, N. M. Harrison, A. I. Kirkland and J. H. Warner, *ACS Nano*, 2013, **7**, 4495–4502, DOI: 10.1021/nn401113r.
160 C. D. Latham, M. I. Heggie, M. Alatalo, S. O. Öberg and P. R. Briddon, *J. Phys.: Condens. Matter*, 2013, **25**, 135403, DOI: 10.1088/0953-8984/25/13/135403.
161 T. Trevethan, C. D. Latham, M. I. Heggie, P. R. Briddon and M. J. Rayson, *Nanoscale*, 2014, **6**, 2978–2986, DOI: 10.1039/c3nr06222h.
162 L. Wu, T. Hou, Y. Li, K. S. Chan and S.-T. Lee, *J. Phys. Chem. C*, 2013, **117**, 17066–17072, DOI: 10.1021/jp405130c.
163 M. T. Lusk and L. D. Carr, *Phys. Rev. Lett.*, 2008, **100**, 175503, DOI: 10.1103/PhysRevLett.100.175503.
164 A. Zobelli, V. Ivanovskaya, P. Wagner, I. Suarez-Martinez, A. Yaya and C. P. Ewels, *Phys. Status Solidi B*, 2012, **249**, 276–282, DOI: 10.1002/pssb.201100630.
165 G. Teobaldi, H. Ohnishi, K. Tanimura and A. L. Shluger, *Carbon*, 2010, **48**, 4145–4161, DOI: 10.1016/j.carbon.2010.07.029.
166 L. Li, S. Reich and J. Robertson, *Phys. Rev. B: Condens. Matter Mater. Phys.*, 2005, **72**, 184109, DOI: 10.1103/PhysRevB.72.184109.
167 J. Kotakoski, A. V. Krasheninnikov, U. Kaiser and J. C. Meyer, *Phys. Rev. Lett.*, 2011, **106**, 105505, DOI: 10.1103/PhysRevLett.106.105505.
168 J. C. Meyer, C. Kisielowski, R. Erni, M. D. Rossell, M. F. Crommie and A. Zettl, *Nano Lett.*, 2008, **8**, 3582–3586, DOI: 10.1021/nl801386m.
169 Z. S. Popović, B. R. K. Nanda and S. Satpathy, *Phys. Rev. B: Condens. Matter Mater. Phys.*, 2012, **86**, 85458, DOI: 10.1103/PhysRevB.86.085458.
170 Y. Kim, J. Ihm, E. Yoon and G.-D. Lee, *Phys. Rev. B: Condens. Matter Mater. Phys.*, 2011, **84**, 075445, DOI: 10.1103/PhysRevB.84.075445.
171 M. M. Ugeda, I. Brihuega, F. Hiebel, P. Mallet, J.-Y. Veuillen, J. M. Gómez-Rodríguez and F. Ynduráin, *Phys. Rev. B: Condens. Matter Mater. Phys.*, 2012, **85**, 121402, DOI: 10.1103/PhysRevB.85.121402.

172 H. Wang, Q. Wang, Y. Cheng, K. Li, Y. Yao, Q. Zhang, C. Dong, P. Wang, U. Schwingenschlögl, W. Yang and X. X. Zhang, *Nano Lett.*, 2012, **12**, 141–144, DOI: 10.1021/nl2031629.

173 G.-D. Lee, C. Z. Wang, E. Yoon, N.-M. Hwang, D.-Y. Kim and K. M. Ho, *Phys. Rev. Lett.*, 2005, **95**, 205501, DOI: 10.1103/PhysRevLett.95.205501.

174 J.-M. Leyssale and G. L. Vignoles, *J. Phys. Chem. C*, 2014, **118**, 8200–8216, DOI: 10.1021/jp501028n.

175 L. Wang, F. Yan, H. L. W. Chan and F. Ding, *Nanoscale*, 2012, **4**, 7489–7493.

176 B. W. Jeong, J. Ihm and G.-D. Lee, *Phys. Rev. B: Condens. Matter Mater. Phys.*, 2008, **78**, 165403, DOI: 10.1103/PhysRevB.78.165403.

177 E. Asari, M. Kitajima, K. G. Nakamura and T. Kawabe, *Phys. Rev. B: Condens. Matter Mater. Phys.*, 1993, **47**, 11143, DOI: 10.1103/PhysRevB.47.11143.

178 J. I. Paredes, P. Solís-Fernández, A. Martínez-Alonso and J. M. D. Tascón, *J. Phys. Chem. C*, 2009, **113**, 10249–10255, DOI: 10.1021/jp901578c.

179 P. O. Lehtinen, A. S. Foster, A. Ayuela, A. V. Krasheninnikov, K. Nordlund and R. M. Nieminen, *Phys. Rev. Lett.*, 2003, **91**, 017202, DOI: 10.1103/PhysRevLett.91.017202.

180 I. C. Gerber, A. V. Krasheninnikov, A. S. Foster and R. M. Nieminen, *New J. Phys.*, 2010, **12**, 113021, DOI: 10.1088/1367-2630/12/11/113021.

181 L. Tsetserisa and S. T. Pantelides, *Carbon*, 2009, **47**, 901–908, DOI: 10.1016/j.carbon.2008.12.002.

182 A. V. Krasheninnikov, K. Nordlund, P. O. Lehtinen, A. S. Foster, A. Ayuela and R. M. Nieminen, *Carbon*, 2004, **42**, 1021–1025, DOI: 10.1016/j.carbon.2003.12.025.

183 A. V. Krasheninnikov, K. Nordlund, P. O. Lehtinen, A. S. Foster, A. Ayuela and R. M. Nieminen, *Phys. Rev. B: Condens. Matter Mater. Phys.*, 2004, **69**, 073402, DOI: 10.1103/PhysRevB.69.073402.

184 A. Hashimoto, K. Suenaga, A. Gloter, K. Urita and S. Iijima, *Nature*, 2004, **430**, 870–873, DOI: 10.1038/nature02817.

185 U. Bangert, M. H. Gass, A. L. Bleloch, R. R. Nair and J. Eccles, *Phys. Status Solidi A*, 2009, **206**, 2115–2119, DOI: 10.1002/pssa.200982207.

186 J. Ma, D. Alfè, A. Michaelides and E. Wang, *Phys. Rev. B: Condens. Matter Mater. Phys.*, 2009, **80**, 033407, DOI: 10.1103/PhysRevB.80.033407.

187 L. Chen, Y. Ouyang, Y. Wang, Y. Sun and H. Pan, *Physica E*, 2010, **43**, 593–597, DOI: 10.1016/j.physe.2010.10.003.

188 Q. Zhao, M. Buongiorno Nardelli and J. Bernholc, *Phys. Rev. B: Condens. Matter Mater. Phys.*, 2002, **65**, 144105, DOI: 10.1103/PhysRevB.65.144105.

189 B. C. Pan, W. S. Yang and J. Yang, *Phys. Rev. B: Condens. Matter Mater. Phys.*, 2000, **62**, 12652–12655, DOI: 10.1103/PhysRevB.62.12652.

190 E. Ertekin, M. S. Daw and D. C. Chrzan, *Philos. Mag. Lett.*, 2008, **88**, 159–167, DOI: 10.1080/09500830701822104.

191 E. Ertekin, D. C. Chrzan and M. S. Daw, *Phys. Rev. B: Condens. Matter Mater. Phys.*, 2009, **79**, 155421, DOI: 10.1103/PhysRevB.79.155421.

192 S. Bhowmick and U. V. Waghmare, *Phys. Rev. B: Condens. Matter Mater. Phys.*, 2010, **81**, 155416, DOI: 10.1103/PhysRevB.81.155416.

193 P. Jensen, J. Gale and X. Blase, *Phys. Rev. B: Condens. Matter Mater. Phys.*, 2002, **66**, 193403, DOI: 10.1103/PhysRevB.66.193403.

194 A. J. M. Nascimento and R. W. Nunes, *Nanotechnology*, 2013, **24**, 435707, DOI: 10.1088/0957-4484/24/43/435707.

195 T. Dumitrica and B. I. Yakobson, *Appl. Phys. Lett.*, 2004, **84**, 2775–2777, DOI: 10.1063/1.1695630.

196 C. P. Ewels, M. I. Heggie and P. R. Briddon, *Chem. Phys. Lett.*, 2002, **351**, 178–182, DOI: 10.1016/S0009-2614(01)01371-9.

197 L. G. Zhou and S.-Q. Shi, *Appl. Phys. Lett.*, 2003, **83**, 1222–1224, DOI: 10.1063/1.1599961.

198 C. Wang and Y. H. Ding, *J. Mater. Chem. A*, 2013, **1**, 1885–1891, DOI: 10.1039/c2ta00736c.

199 Z. Li, P. Dharap, P. Sharma, S. Nagarajaiah and B. I. Yakobson, *J. Appl. Phys.*, 2005, **97**, 074303, DOI: 10.1063/1.1870102.

200 Ge. G. Samsonidze, G. G. Samsonidze and B. I. Yakobson, *Phys. Rev. Lett.*, 2002, **88**, 065501, DOI: 10.1103/PhysRevLett.88.065501.

201 B. I. Yakobson, G. Samsonidze and G. G. Samsonidze, *Carbon*, 2000, **38**, 1675–1680, DOI: 10.1016/S0008-6223(00)00093-2.

202 M. Buongiorno Nardelli, B. I. Yakobson and J. Bernholc, *Phys. Rev. B: Condens. Matter Mater. Phys.*, 1998, **57**, R4277–R4280, DOI: 10.1103/PhysRevB.57.R4277.

203 S. Chen, *Buckling and topological defects in graphene and carbon nanotubes*, PhD thesis, University of California, Berkeley, 2012.

204 S. Chen, E. Ertekin and D. C. Chrzan, *Phys. Rev. B: Condens. Matter Mater. Phys.*, 2010, **81**, 155417, DOI: 10.1103/PhysRevB.81.155417.

205 I. Zsoldos, *Nanotechnol., Sci. Appl.*, 2010, **3**, 101–106, DOI: 10.2147/NSA.S13905.

206 B. B. Fan, X. B. Yang and R. Zhang, *Phys. Lett. A*, 2010, **374**, 2781–2784, DOI: 10.1016/j.physleta.2010.04.066.

207 Z. Song, V. I. Artyukhov, B. I. Yakobson and Z. Xu, *Nano Lett.*, 2013, **13**, 1829–1833, DOI: 10.1021/nl400542n.

208 R. Grantab, V. B. Shenoy and R. S. Ruoff, *Science*, 2010, **330**, 946–948, DOI: 10.1126/science.1196893.

209 L. Yi, Z. Yin, Y. Zhang and T. Chang, *Carbon*, 2013, **51**, 373–380, DOI: 10.1016/j.carbon.2012.08.069.

210 Y. J. Wei, J. Wu, H. Yin, X. Shi, R. Yang and M. S. Dresselhaus, *Nat. Mater.*, 2012, **11**, 759–763, DOI: 10.1038/nmat3370.

211 P. Zhang, P. E. Lammert and V. H. Crespi, *Phys. Rev. Lett.*, 1998, **81**, 5346–5349, DOI: 10.1103/PhysRevLett.81.5346.

212 Y. J. Sun, F. Ma, D. Y. Ma, K. W. Xu and P. K. Chu, *J. Phys. D: Appl. Phys.*, 2012, **45**, 305303, DOI: 10.1088/0022-3727/45/30/305303.

213 D. Bozovic, M. Bockrath, J. H. Hafner, C. M. Lieber, H. Park and M. Tinkham, *Phys. Rev. B: Condens. Matter Mater. Phys.*, 2003, **67**, 033407, DOI: 10.1103/PhysRevB.67.033407.

214 B. G. Demczyk, Y. M. Wang, J. Cumings, M. Hetman, W. Han, A. Zettl and R. O. Ritchie, *Mater. Sci. Eng., A*, 2002, **334**, 173–178.

215 B. I. Yakobson, *Appl. Phys. Lett.*, 1998, **72**, 918–920, DOI: 10.1063/1.120873.
216 M. Buongiorno Nardelli, B. I. Yakobson and J. Bernholc, *Phys. Rev. Lett.*, 1998, **81**, 4656–4659, DOI: 10.1103/PhysRevLett.81.4656.
217 F. Ding, K. Jiao, M. Wu and B. I. Yakobson, *Phys. Rev. Lett.*, 2007, **98**, 075503, DOI: 10.1103/PhysRevLett.98.075503.
218 J. H. Warner, E. R. Margine, M. Mukai, A. W. Robertson, F. Giustino and A. I. Kirkland, *Science*, 2012, **337**, 209–212, DOI: 10.1126/science.1217529.
219 K. Suenaga, H. Wakabayashi, M. Koshino, Y. Sato, K. Urita and S. Iijima, *Nat. Nanotechnol.*, 2007, **2**, 358–360, DOI: 10.1038/nnano.2007.141.
220 J. Guo, J. R. Morris, Y. Ihm, C. I. Contescu, N. C. Gallego, G. Duscher, S. J. Pennycook and M. F. Chisholm, *Small*, 2012, **8**, 3283–3288, DOI: 10.1002/smll.201200894.
221 O. V. Yazyev and S. G. Louie, *Phys. Rev. B: Condens. Matter Mater. Phys.*, 2010, **81**, 195420, DOI: 10.1103/PhysRevB.81.195420.
222 T.-H. Liu, G. Gajewski, C.-W. Pao and C.-C. Chang, *Carbon*, 2011, **49**, 2306–2317, DOI: 10.1016/j.carbon.2011.01.063.
223 Y. Liu and B. I. Yakobson, *Nano Lett.*, 2010, **10**, 2178–2183, DOI: 10.1021/nl100988r.
224 F. Ding, K. Jiao, Y. Lin and B. I. Yakobson, *Nano Lett.*, 2007, **7**, 681–684, DOI: 10.1021/nl0627543.
225 O. Lehtinen, S. Kurasch, A. V. Krasheninnikov and U. Kaiser, *Nat. Commun.*, 2013, **4**, 2089, DOI: 10.1038/ncomms3098.
226 J. Y. Huang, S. Chen, S. H. Jo, Z. Wang, D. X. Han, G. Chen, M. S. Dresselhaus and Z. F. Ren, *Phys. Rev. Lett.*, 2005, **94**, 236802, DOI: 10.1103/PhysRevLett.94.236802.
227 C. Gómez-Navarro, J. C. Meyer, R. S. Sundaram, A. Chuvilin, S. Kurasch, M. Burghard, K. Kern and U. Kaiser, *Nano Lett.*, 2010, **10**, 1144–1148, DOI: 10.1021/nl9031617.
228 G.-D. Lee, E. Yoon, K. He, A. W. Robertson and J. H. Warner, *Nanoscale*, 2014, **6**, 14836–14844, DOI: 10.1039/c4nr04718d.
229 G.-D. Lee, E. Yoon, N.-M. Hwang, C.-Z. Wang and K.-M. Ho, *Appl. Phys. Lett.*, 2013, **102**, 021603, DOI: 10.1063/1.4775671.
230 M. H. Gass, U. Bangert, A. L. Bleloch, P. Wang, R. R. Nair and A. K. Geim, *Nat. Nanotechnol.*, 2008, **3**, 676–681, DOI: 10.1038/nnano.2008.280.
231 P. Simonis, C. Goffaux, P. A. Thiry, L. P. Biro, Ph. Lambin and V. Meunier, *Surf. Sci.*, 2002, **511**, 319–322, DOI: 10.1016/S0039-6028(02)01511-X.
232 J. Coraux, A. T. N'Diaye, C. Busse and T. Michely, *Nano Lett.*, 2008, **8**, 565–570, DOI: 10.1021/nl0728874.
233 Y. Tison, J. Lagoute, V. Repain, C. Chacon, Y. Girard, F. Joucken, R. Sporken, F. Gargiulo, O. V. Yazyev and S. Rousset, *Nano Lett.*, 2014, **14**, 6382–6386, DOI: 10.1021/nl502854w.
234 P. Y. Huang, C. S. Ruiz-Vargas, A. M. van der Zande, W. S. Whitney, M. P. Levendorf, J. W. Kevek, S. Garg, J. S. Alden, C. J. Hustedt, Y. Zhu, J. Park, P. L. McEuen and D. A. Muller, *Nature*, 2011, **469**, 389–393, DOI: 10.1038/nature09718.
235 B. Yang, H. Xu, J. Lu and K. P. Loh, *J. Am. Chem. Soc.*, 2014, **136**, 12041–12046, DOI: 10.1021/ja5054847.
236 K. Kim, Z. Lee, W. Regan, C. Kisielowski, M. F. Crommie and A. Zettl, *ACS Nano*, 2011, **5**, 2142–2146, DOI: 10.1021/nn1033423.
237 O. V. Yazyev, *Solid State Commun.*, 2012, **152**, 1431–1436, DOI: 10.1016/j.ssc.2012.04.045.
238 B. I. Yakobson and F. Ding, *ACS Nano*, 2011, **5**, 1569–1574, DOI: 10.1021/nn200832y.
239 J. Zhang, J. Zhao and J. Lu, *ACS Nano*, 2012, **6**, 2704–2711, DOI: 10.1021/nn3001356.
240 S. Malola, H. Häkkinen and P. Koskinen, *Phys. Rev. B: Condens. Matter Mater. Phys.*, 2010, **81**, 165447, DOI: 10.1103/PhysRevB.81.165447.
241 A. Cao and Y. Yuan, *Appl. Phys. Lett.*, 2012, **100**, 211912, DOI: 10.1063/1.4722786.
242 V. V. Ivanovskaya, A. Zobelli, P. Wagner, M. I. Heggie, P. R. Briddon, M. J. Rayson and C. P. Ewels, *Phys. Rev. Lett.*, 2011, **107**, 065502, DOI: 10.1103/PhysRevLett.107.065502.
243 P. Koskinen, S. Malola and H. Häkkinen, *Phys. Rev. Lett.*, 2008, **101**, 115502, DOI: 10.1103/PhysRevLett.101.115502.
244 J. Kunstmann, C. Özdoğan, A. Quandt and H. Fehske, *Phys. Rev. B: Condens. Matter Mater. Phys.*, 2011, **83**, 045414, DOI: 10.1103/PhysRevB.83.045414.
245 J. M. H. Kroes, M. A. Akhukov, J. H. Los, N. Pineau and A. Fasolino, *Phys. Rev. B: Condens. Matter Mater. Phys.*, 2011, **83**, 165411, DOI: 10.1103/PhysRevB.83.165411.
246 T. Wassmann, A. P. Seitsonen, A. M. Saitta, M. Lazzeri and F. Mauri, *Phys. Rev. Lett.*, 2008, **101**, 096402, DOI: 10.1103/PhysRevLett.101.096402.
247 B. Huang, M. Liu, N. Su, J. Wu, W. Duan, B. Gu and F. Liu, *Phys. Rev. Lett.*, 2009, **102**, 166404, DOI: 10.1103/PhysRevLett.102.166404.
248 C. K. Gan and D. J. Srolovitz, *Phys. Rev. B: Condens. Matter Mater. Phys.*, 2010, **81**, 125445, DOI: 10.1103/PhysRevB.81.125445.
249 J. M. Carlsson, L. M. Ghiringhelli and A. Fasolino, *Phys. Rev. B: Condens. Matter Mater. Phys.*, 2011, **84**, 165423, DOI: 10.1103/PhysRevB.84.165423.
250 Y. Wei, J. Wu, H. Yin, X. Shi, R. Yang and M. Dresselhaus, *Nat. Mater.*, 2012, **11**, 759–763, DOI: 10.1038/nmat3370.
251 E. Cockayne, G. M. Rutter, N. P. Guisinger, J. N. Crain, P. N. First and J. A. Stroscio, *Phys. Rev. B: Condens. Matter Mater. Phys.*, 2011, **83**, 195425, DOI: 10.1103/PhysRevB.83.195425.
252 G. D. Lee, E. Yoon, C.-Z. Wang and K.-M. Ho, *J. Phys.: Condens. Matter*, 2013, **25**, 155301, DOI: 10.1088/0953-8984/25/15/155301.
253 L. L. Song, X. H. Zheng, R. L. Wang and Z. Zeng, *J. Phys. Chem. C*, 2010, **114**, 12145–12150, DOI: 10.1021/jp1040025.
254 J. H. Warner, Y.-C. Lin, K. He, M. Koshino and K. Suenaga, *Nano Lett.*, 2014, **14**, 6155–6159, DOI: 10.1021/nl5023095.
255 K. Kim, S. Coh, C. Kisielowski, M. F. Crommie, S. G. Louie, M. L. Cohen and A. Zettl, *Nat. Commun.*, 2013, **4**, 2723, DOI: 10.1038/ncomms3723.
256 C.-I. Chia and V. H. Crespi, *Phys. Rev. Lett.*, 2012, **109**, 076802, DOI: 10.1103/PhysRevLett.109.076802.
257 V. I. Artyukhov, Y. Liu and B. I. Yakobson, *Proc. Natl. Acad. Sci. U. S. A.*, 2012, **109**, 15136–15140, DOI: 10.1073/pnas.1207519109.

258 J. Lee, Z. Yang, W. Zhou, S. J. Pennycook, S. T. Pantelides and M. F. Chisholm, *Proc. Natl. Acad. Sci. U. S. A.*, 2014, **111**, 7522–7526, DOI: 10.1073/pnas.1400767111.

259 J. H. Warner, Z. Liu, K. He, A. W. Robertson and K. Suenaga, *Nano Lett.*, 2013, **13**, 4820–4826, DOI: 10.1021/nl402514c.

260 Ç. Ö. Girit, J. C. Meyer, R. Erni, M. D. Rossell, C. Kisielowski, L. Yang, C.-H. Park, M. F. Crommie, M. L. Cohen, S. G. Louie and A. Zettl, *Science*, 2009, **323**, 1705–1708, DOI: 10.1126/science.1166999.

261 S. S. Terdalkar, S. Huang, H. Yuan, J. J. Rencis, T. Zhu and S. Zhang, *Chem. Phys. Lett.*, 2010, **494**, 218–222, DOI: 10.1016/j.cplett.2010.05.090.

262 J. Zhu and D. Shi, *J. Appl. Phys.*, 2011, **110**, 104311, DOI: 10.1063/1.3662183.

263 E. Erdogan, I. Popov, C. G. Rocha, G. Cuniberti, S. Roche and G. Seifert, *Phys. Rev. B: Condens. Matter Mater. Phys.*, 2011, **83**, 041401, DOI: 10.1103/PhysRevB.83.041401.

264 A. W. Robertson, G. D. Lee, K. He, E. Yoon, A. I. Kirland and J. H. Warner, *Nano Lett.*, 2014, **14**, 1634–1642, DOI: 10.1021/nl500119p.

265 A. Zobelli, A. Gloter, C. P. Ewels, G. Seifert and C. Colliex, *Phys. Rev. B: Condens. Matter Mater. Phys.*, 2007, **75**, 245402, DOI: 10.1103/PhysRevB.75.245402.

266 Z. Wang, Y. G. Zhou, J. Bang, M. P. Prange, S. B. Zhang and F. Gao, *J. Phys. Chem. C*, 2012, **116**, 16070–16079, DOI: 10.1021/jp303905u.

267 J. C. Meyer, F. Eder, S. Kurasch, V. Skakalova, J. Kotakoski, H. J. Park, S. Roth, A. Chuvilin, S. Eyhusen, G. Benner, A. V. Krasheninnikov and U. Kaiser, *Phys. Rev. Lett.*, 2013, **110**, 239902, DOI: 10.1103/PhysRevLett.110.239902.

268 A. Krasheninnikov, F. Banhart, J. Li, A. Foster and R. Nieminen, *Phys. Rev. B: Condens. Matter Mater. Phys.*, 2005, **72**, 125428, DOI: 10.1103/PhysRevB.72.125428.

269 L. Tsetseris, B. Wang and S. T. Pantelides, *Phys. Rev. B: Condens. Matter Mater. Phys.*, 2014, **89**, 035411, DOI: 10.1103/PhysRevB.89.035411.

270 K. He, A. W. Robertson, S. Lee, E. Yoon, G. D. Lee and J. H. Warner, *ACS Nano*, 2014, **8**, 12272–12279, DOI: 10.1021/nn504471m.

271 K. Jin, H. Y. Xiao, Y. Zhang and W. J. Weber, *Appl. Phys. Lett.*, 2014, **104**, 203106, DOI: 10.1063/1.4879258.

